GEOPHYSICAL FLUID FLOW DURING HYDROTHERMAL VENTING AND CARBON SEQUESTRATION

A Dissertation
Presented to
The Academic Faculty

by

Joshua E. Smith

In Partial Fulfillment
of the Requirements for the Degree
of Doctor of Philosophy in the
School of Civil and Environmental Engineering

Georgia Institute of Technology

December 2017

GEOPHYSICAL FLUID FLOW DURING HYDROTHERMAL VENTING

AND CARBON SEQUESTRATION

Approved by:

Dr. Leonid N. Germanovich, Advisor
School of Civil and Environmental Eng.
Georgia Institute of Technology

Dr. J. David Frost
School of Civil and Environmental Eng.
Georgia Institute of Technology

Dr. Haiying Huang
School of Civil and Environmental Eng.
Georgia Institute of Technology

Dr. Sheng Dai
School of Civil and Environmental Eng.
Georgia Institute of Technology

Dr. Robert P. Lowell
Department of Geosciences
Virginia Polytechnic Institute and State University

Dr. Lawrence C. Murdoch
School of Environmental Eng. And Earth Sciences
Clemson University

Date Approved: 06/17/2017

ACKNOWLEDGEMENTS

First and foremost, I wish to expresses my highest appreciation to my family for their unwavering support throughout my life. This endeavor was only possible due to their encouragement and sacrifices.

I am sincerely grateful to Dr. Leonid N. Germanovich for his mentoring and contributions to this work. His unique insight challenged me to approach problems in new and surprising ways. I want to extend my gratitude to my thesis committee: Dr. J. David Frost, Dr. Haiying Huang, Dr. Sheng Dai, Dr. Robert P. Lowell, and Dr. Lawrence C. Murdoch. Their patience and valuable comments were paramount to this work. In particular, I would like to acknowledge the guidance of Dr. Robert P. Lowell, Dr. Lawrence C. Murdoch, and Dr. J. David Frost.

The invaluable efforts of Arlette De Santiago, who provided many hours of editing are greatly appreciated. I would also like to express my thanks to Longde Jin for his assistance on the revisions of this manuscript. I am indebted to the past members of Rock and Fracture Mechanics Laboratory at Georgia Tech for their technical and personal support. I thank Sihyun Kim, Thomas Wang, Gence Genc, John Hu, Devon Gwaba, and Robert Hurt. I am particularly grateful to Sihyun Kim and Thomas Wang for their interest and many stimulating discussions.

My experience in the Atlanta region was shaped by the professional and personal relationships forged here. The interactions with my colleagues was a vital part of my graduate studies. As such, I wish to recognize Alejandro Martinez, Andres Peralta, Mahdi Roozbahani, Fikret Atalay, Sangy Hanumasagar, Albert Liu, Rodrigo Borela Valenta, Nicole Caruso, Cheng Zhu, Xenia Wirth, and Jackson Su. All members in the Georgia Tech Geosociety and faculty should also be acknowledged. I am also grateful of the efforts provided by the Civil and Environmental Engineering staff: Robert Simon, Lisa Tuttle, Crystal Hanson, Belal Elnaggar, and Melisa Hubbs. Furthermore, I wish to acknowledge the friends I have made here in Atlanta, which include Rupam Banerjee, Brandon Duncan, Peter Wang, Artem Usanin, and Jeanette Pyle.

This work was made possible in part by the support of National Science Foundation (grant OCE-1131355) and Department of Energy (grant DE-FE0023313). I am thankful for the efforts of our industrial collaborator, Grand Resources Inc. In particular, I greatly appreciate the guidance and assistance provided by Marvin Robinowitz, Richard Robinowitz, Scott Robinowitz, Dwight Dauben, and June Schmeling. I am also thankful for the collaborative efforts of Dr. Stephen Moysey, Dr. Scott DeWolf, and Alex Hanna on this project.

TABLE OF CONTENTS

LIST OF TABLES

page

LIST OF FIGURES

page

SUMMARY

This dissertation involves two topics *(i)* buoyant, turbulent discharge and *(ii)* fluid flow in porous medium coupled with mechanical deformation. Specifically, we quantify discharge and heat flux from hydrothermal plumes along oceanic spreading centers, and model the poroelastic response of the subsurface during injection into reservoirs. Chapters 2 of this work is published in the *Journal of Geophysical Research* [*Germanovich et al.*, 2015]. and Chapter 3 is written in the format of a manuscript to be submitted in the near future. Consequently, the chapters have their own introductions and list of references.

The first part of this thesis is concerned with measuring hydrothermal discharge along mid-ocean ridges. This work builds upon the study of *Genc* [2012], who first reported on some of the measurements in this work. We have enhanced the database to include approximately double the number of total measurements. This includes 16 measurements performed with devices that predated the flowmeters developed by *Genc* [2012] and *Germanovich et al.*, [2015], 30 more measurements along the Juan de Fuca Ridge, and 12 new measurements at the East Pacific Rise during Jason dives 758, 759, and 760. We improve upon the interpretation of the data using these new measurements.

Near mid-ocean ridges, magma bodies may occur as inclusions at shallow depths. Ambient seawater enters the subsurface and infiltrates towards the magma bodies. The low temperature seawater mines heat from the magma inclusions, undergoing water-rock reactions that result in a chemically altered, low density, hot buoyant fluid that rises towards the surface to discharge through discrete orifices as focused flow or mixes with ambient seawater near the surface to vent as diffusive patches on the seafloor. Seafloor hydrothermal venting plays a significant role in the Earth's energy and geochemical budgets and support unique seafloor ecosystems. Quantifying the fluid flow and heat output are key parameters necessary to constrain models of hydrothermal circulation. Hydrothermal fluids discharge at temperatures approaching 400°C. Pressures exceed 20 MPa, which is many times greater than available in current lab or other field settings. The challenging nature of collecting data in the extreme environment of seafloor hydrothermal venting has severely restricted measurements on these vents. Indirect and most direct measurement techniques of fluid velocity and heat output cannot partition flow derived from focused or diffuse sources.

In this work, we discuss current techniques for measuring hydrothermal discharge and heat flux and describe the performance of devices deployed on 45 dives across the North, South, and Equatorial Pacific. Devices are deployed using occupied or remotely operated submersibles to record unlimited measurements over the course of a dive. The devices can measure flow rates over two orders of magnitude. Instruments do not require maintenance between dives and last for multiple cruises without requiring maintenance. The rotations of rotor blades allows determination of flow velocity, areas are determine using submersible lasers, and vent fluid temperature is measured with the submersible temperature probe. The measured flow rates can be used in conjunction with vent temperature or geochemical measurements to obtain heat outputs or geochemical fluxes from both focused and diffuse flow sites.

The devices were tested on 30 *Alvin* dives on the Juan de Fuca ridge and 3 *Jason* dives on the East Pacific Rise. We report 104 new measurements over a wide range of discharge temperatures (5 to 363°C), velocities (2 to 199 cm/s), and depths (1517 to 2511 m). These include the first advective heat output measurements at the High Rise vent field and the first direct fluid flow measurement at Middle Valley. Our data suggest that black smoker heat output at the Main Endeavour vent field may have declined since 1994 and that after the 2005–2006 eruption, the high-temperature advective flow at the East Pacific Rise 9°50'N field may have become more channelized, predominately discharging through the Bio 9 structure. We also report 16 measurements on 10 *Alvin* dives and 2 *Jason* dives with flow meters that predate devices described in this work and were used in the process of their development. This includes the first advective measurements in the Lau Basin and at the East Pacific Rise 9°39.5'N.

The second part of this thesis is concerned with monitoring the injection process during carbon storage and petroleum operations. Carbon storage in geologic formations is a promising option to mitigate the rise of CO_2 in the atmosphere; however, injecting CO_2 increases and redistributes the pressure in the formation. Monitoring is necessary to provide an early warning system of hazards during the injection process and to insure the long-term security of injected carbon. One possible way to monitor the fluid injection processes is by measuring subsurface deformation.

Injection into geologic formations deforms the reservoir and confining units in a complex pattern that increases in magnitude and expands outward with time. Formation properties and pressure redistribution affect the deformation pattern, and this effect is possible to interpret from measurements of the strain tensor. We utilized a combination of analytical and numerical

methods to develop models of the subsurface deformation induced by pressurized regions. Our models suggest monitoring instruments at significantly shallower depths than the reservoir are capable of measuring deformation signals generated during waterflooding or carbon sequestration operations. From this analysis we determined strainmeters may be installed at relatively shallow depths (first several hundred feet of the subsurface). This eliminates the need of deep monitoring wells (at the depth of the reservoir) that are both challenging and costly depths.

Based on the available 2-D and 3-D analytical solutions of deformation induced by pressurized inclusions in an infinite half-space, we show the principle of monitoring deformation to interpret the pressure increase in a reservoir. The strain tensor is distinctive and forms a characteristic signature from pressurized geometries representative of injection into reservoirs. Strains and tilts are measurable up to the ground surface, suggesting it is feasible to use measurements of deformation in shallow boreholes. Multiple components of strain are more effective than a single component, or pressure signals, at constraining pressurized geometries. A function consisting of multiple components of strain and tilt was introduced to determine the location where the signal strength is greatest. The deformation function has a distinct minimum at a depth of several hundred feet, which suggests there may be a range of depths that are best. These locations correspond to the target depth to deploy monitoring instruments, but the ultimate determination of instrument siting will be dependent on local field conditions.

Modern borehole strainmeters are capable of measuring multiple components of strain and tilt, however, this technique has not been validated in the field. The first field test of this technique will occur during a waterflooding operation at the carbon storage analog site at the North Avant oil field in Osage County, OK. This field is a representative example of geological formations proposed for carbon storage. To design the field test, we perform a geologic analysis to develop a conceptual model of the North Avant field. Currently, two boreholes have been drilled for instrument installation based on this analysis.

The geologic analysis of the North Avant field site was applied to more realistic numerical models of the poroelastic response to water injection. A benchmark axisymmetric model is representative of the idealized conditions at a planned water injection test site. Our results suggest monitoring instruments should be deployed at a depth of $z \leq 200$ ft or $z \geq 450$ ft. Instruments should be installed away from the wellbore to register tilt signals, but within 1000 ft to measure strains. If fluid in injected at a rate of 300 psi into the Bartlesville sandstone, the

resulting deformation is on the order of 1×10^{-7}. From this analysis, two monitoring wells have been drilled at the North Avant field in preparation of a field demonstration, with more scheduled for drilling.

Permeability is likely to vary within reservoirs, but dimensions are challenging to constrain without extensive testing. High permeability channels are common in petroleum formations consisting of fluvial deposits and strongly affect the fluid flow pattern. These high permeability channels would allow faster injection rates and increased carbon storage capacity, but may result in unexpected fluid migration that could lead to CO_2 escape. It is therefore important to identify such channels in order to make informed decisions during CO_2 sequestration and petroleum operations. The major reservoir of the North Avant field, the Bartlesville sandstone, consists of homogenous reservoir underlain by channels of high permeability that are present locally.

We developed a 3-D model of injection into the Bartlesville sandstone to determine the effect of a heterogeneous permeability on the deformation pattern in the subsurface. Permeability boundaries result in an increase of deformation compared to the benchmark model. The increase in deformation is most prominent near lateral permeability boundaries. When injection occurs at a well intersecting the high energy channels, strains in the shallow subsurface increase over the channel. Adjacent to the channel, strains decrease compared to the benchmark model, but tilts increase when the boundary is perpendicular to the direction of the component of tilt. This suggests that a spatial array of measurements of the strain tensor may be used to contain the dimensions of the high energy channels

CHAPTER 1

FLUID FLOW AND HEAT OUTPUT IN SEAFLOOR HYDROTHERMAL ENVIRONMENTS

1.1. Abstract

This chapter consists of published material in the *J. Geophys. Res Solid Earth, 120* [*Germanovich et al.*, 2015] and builds upon the work by *Genc* [2012]. We review techniques for measuring fluid flow and advective heat output from seafloor hydrothermal systems and describe new measurements from anemometer and turbine flowmeter devices we have calibrated and tested. These devices allow measuring fluid velocity at high- and low-temperature focused and diffuse discharge sites at oceanic spreading centers. The devices perform at ocean floor depths and black smoker temperatures and can be used to measure flow rates ranging over 2 orders of magnitude. Flow velocity is determined from the rotation rate of the rotor blades or paddle assembly. These devices have an open bearing design that eliminates clogging by particles or chemical precipitates as the fluid passes by the rotors. The devices are compact and lightweight enough for deployment from either an occupied or a remotely operated submersible. The measured flow rates can be used in conjunction with vent temperature or geochemical measurements to obtain heat outputs or geochemical fluxes from both vent chimneys and diffuse flow regions. The devices were tested on 30 *Alvin* dives on the Juan de Fuca ridge and 3 *Jason* dives on the East Pacific Rise. We report 104 new measurements over a wide range of discharge temperatures (5°–363°C), velocities (2–199 cm/s), and depths (1517–2511 m). These include the first advective heat output measurements at the High Rise vent field and the first direct fluid flow measurement at Middle Valley. Our data suggest that black smoker heat output at the Main Endeavour vent field may have declined since 1994 and that after the 2005–2006 eruption, the high-temperature advective flow at the East Pacific Rise 9°50'N field may have become more channelized, predominately discharging through the Bio 9 structure. We also report 16 measurements on 10 *Alvin* dives and 2 *Jason* dives with flow meters that predate devices described in this work and were used in the process of their development. This includes the first advective measurements in the Lau Basin and at the East Pacific Rise 9°39.5'N. We discuss potential error sources and how they may affect the accuracy of measurements by our devices and other devices.

1.2. Introduction

The unique environment of hydrothermal venting along oceanic spreading centers has pushed the innovation of heat measurement techniques since first being discovered 40 years ago. Discharge along the seafloor is divided into low-temperature "diffuse" discharge, first detected at the Galapagos Spreading Center in 1977 [*Corliss et al.*, 1979], and high-temperature "focused" flow, first observed along the East Pacific Rise [*Spiess et al.*, 1980]. Discrete orifices focus the high-temperature supersaturated fluids. Upon mixing with ambient seawater, minerals precipitate out, building large (up to tens of meters tall) structures. Chemical signatures indicate that diffuse flow is a mixture of hot fluid and ambient seawater [*Corliss et al.*, 1979; *Edmond et al.*, 1979; *Cooper et al.*, 2000; *Von Damm and Lilley*, 2004; *Lang et al.*, 2006]. This relatively low temperature fluid vents through fissures on sulfide structures or higher permeability zones on the adjacent seafloor.

Heat output from both diffuse and focused flow sites provide important constraints on mathematical models that relate magmatic and hydrothermal heat fluxes [e.g. *Lowell and Germanovich*, 2004; *Liu and Lowell*, 2009; *Wankel et al.*, 2011; Genc 2012; *Lowell et al.*, 2013; *Germanovich et al.*, 2015] and are critical for understanding the physical and geochemical evolution of seafloor hydrothermal systems [e.g., *Lowell and Germanovich*, 1994, 2004]. Hydrothermal vents provide chemical and heat energy for unique biological communities with speciation dependent upon fluid characterization [e.g., *Levin et al.*, 2016]. The flow data is necessary to constrain how the vents support communities [*Butterfield et al.*, 2004; *Von Damm and Lilley*, 2004; *Wankel et al.*, 2011].

Biological communities vary along a plume's ecotone. For example, bacteria biomass increases within neutrally buoyant plumes [*Winn et al.*, 1986] and above these plumes, where zooplankton feed off chemosynthetic energy [*Burd and Thomson*, 1994; *Vereshchaka and Vinogradov*, 1999; *Cowen et al.*, 2001]. Recent studies [e.g., *Hinrichs and Boetius*, 2002; *Dekas et al.*, 2009; *Boetius and Wenzhöfer*, 2013] have also shown the importance of hydrothermal vents in biogeochemical cycling on a global scale [*Levin et al.*, 2016].

Measurements at seafloor hydrothermal vent fields pose several challenges. The fields are located along oceanic spreading centers at depths of several kilometers. To the best of our knowledge, these vents provide a setting of pressure many times greater than current lab or other field testing. Additionally, discharge temperatures approach 400°C. Numerous methods have been proposed and tested for measurements of both focused and diffuse flow [*Converse et al.*, 1984; *Baker and Massoth*, 1987; *Schultz et al.*, 1992; *Thomson et al.*, 1992; *Ginster et al.*, 1994;

Ramondenc et al., 2006; *Genc*, 2012; *Germanovich et al.*, 2012]. Heat output is measured on the scale of an entire vent field using integrated water column measurements, or direct measurements of individual vents are conducted on discrete orifices. We discuss current techniques for measuring hydrothermal heat flux and describe the performance of a cup anemometer device and two turbine flow meter devices deployed on a total of 30 dives with submersible *Alvin* and 3 dives with ROV *Jason*. We also report measurements on 10 *Alvin* and 2 *Jason* dives with devices that predate those described in this work and discuss instrument limitations.

1.3. Integrated measurements

Heat flow data are collected at the scale of a vent field by conductivity-temperature-depth and transmissometer tows or vertical casts and water bottle sampling through the plume and the ambient ocean [*Baker and Massoth*, 1987; *Thomson et al.*, 1992; *Gendron et al.*, 1994; *Baker et al.*, 1998]. These data are used to determine the maximum rise height in the plume z_{max} and to construct the background density profile $\rho_a(z)$, where *z* is height above the plume source. One can also use the excess heat content in the neutrally buoyant plume and the advective transport velocity of the plume to estimate the heat output from a vent field [e.g., *Baker and Massoth*, 1987; *Thomson et al.*, 1995]. Measurements within neutrally buoyant plumes have been used to determine the integrated heat output from hydrothermal vent fields at the Flow and Floc vent areas at the CoAxial segment [*Baker et al.*, 1998]; at the Endeavour segment [*Baker and Massoth*, 1987; *Thomson et al.*, 1992], Main Endeavour Field (MEF) [*Veirs et al.*, 2006], and North Cleft segment [*Baker et al.*, 1993] of the Juan de Fuca ridge; and Broken Spur [*Murton et al.*, 1999] and Trans-Atlantic Geotraverse (TAG) [*Rudnicki and Elderfield*, 1992] hydrothermal fields at the Mid-Atlantic ridge.

The fundamental theory for rise and spreading of turbulent buoyant plumes is outlined by *Morton* [1957] and reviewed by *Fischer et al.* [1979], *Turner* [1986], and *Hunt and van den Bremer* [2011] among others. The theory shows that for a buoyant axisymmetric plume rising from a point source with negligible momentum, $z_{max} = 5(B_0/\pi)^{1/4}N^{-3/4}$, where $B_0 = \alpha_T g H_0/\left(c_p \rho_0\right)$ is the buoyancy flux at the source; $N = [(g/\rho_0)(-d\rho_a/dz)]^{1/2}$ is the buoyancy frequency; g is the gravitational acceleration; ρ_0 and H_0 are the fluid density and the total heat flux at the source,

respectively; α_T is the coefficient of thermal expansion of seawater at ambient, low-temperature conditions; c_p is the fluid specific heat at constant pressure; and the density gradient $d\rho_a/dz$ in the ambient stratified environment is assumed to be constant. These expressions result in $H_0 = [\pi\rho_0 c_p/(\alpha_T g)](z_{max}/5)^4 N^3$ [e.g., *Baker*, 1994, 2007; *Thomson et al.*, 1995], indicating that the heat output is very sensitive to estimates of z_{max} and $d\rho_a/dz$. As a result, heat outputs obtained from measurements in the neutrally buoyant plume are uncertain by at least a factor of 2 [e.g., *Baker*, 2007]. For example, *Carazzo et al.* [2008] introduced a variable entrainment law to conclude that the heat flux from a hydrothermal plume on the TAG mound is 3 times greater than that obtained by *Rudnicki and Elderfield* [1992], who used the same data set as *Carazzo et al.* [2008], but with a different entrainment coefficient. Further, integrated water column measurements require a large scale effort and time to complete [e.g., *Genc*, 2012; *Germanovich et al.*, 2015].

Rona and Speer [1989] apply the buyout plume theory to plumes rising in the ocean where the ambient density structure depends upon both temperature and salinity. *Speer and Helfrich* [1995] discuss the effects of cross currents and Coriolis effects and conclude that buoyant plumes can drive ocean circulation at larger scales.

1.4. Direct measurements

Direct measurements refer to a class of measurements made at a discrete venting site near the seafloor, whether from a high-temperature chimney orifice or a low-temperature diffuse flow site. Direct measurements also include those made in the buoyant plume at some height above individual vents. To obtain the heat output from a vent field, measurements are summed over the discrete sources of fluid discharge, often extrapolating from a relatively small number of actual measurements to the vent field scale [e.g., *Little et al.*, 1987; *Rona and Trivett*, 1992; *Bemis et al.*, 1993; *Ramondenc et al.*, 2006]. Methods of direct measurements are described below and the calibration (section 1.5) and performance (section 1.6.1) of a cup anemometer and turbine flowmeter designed by *Genc* [2012] and *Germanovich et al.*, [2015] are later described in detail.

1.4.1. Direct measurements in buoyant plumes

A number of techniques exist to estimate hydrothermal heat output from measurements within buoyant plumes rising above discrete vents. For example, *Little et al.* [1987] and *Bemis et al.* [1993] used a package of instruments deployed from a submersible to obtain profiles of temperature, velocity, conductivity, and pressure. The velocity and temperature in the buoyant plume were measured directly, so *Little et al.* [1987] and *Bemis et al.* [1993] applied classic plume theory [*Morton et al.*, 1956; *Tennekes and Lumley*, 1972; *Fischer et al.*, 1979; *Turner*, 1986; *Papanicolaou and List*, 1987].

A limited number of studies have addressed the heat output from diffusive discharge sites [e.g., *Rona and Trivett*, 1992; *Schultz et al.*, 1992, *Ramondenc et al.* 2006; *Veirs et al.*, 2006; *Genc*, 2012]. Lower density diffuse flow reaches its neutral buoyancy at relatively shorter heights above the seafloor [e.g., *Rona and Trivett*, 1992]. This imposes a greater challenge to measure heat flux via plume methods. Still, diffuse flow may account for a large fraction of the total heat output from a vent field [e.g., *Schultz et al.*, 1992; *Ramondenc et al.*, 2006]. It is noteworthy, however, that integrated heat output measurements in the neutrally buoyant plume typically exceed estimates made from direct measurements in high-temperature buoyant plumes [e.g., *Baker*, 2007]. This suggests that mixing in the deep ocean changes the density structure such that measurements in the neutrally buoyant plume contain some heat output that results from diffuse flow and integrated water column measurements may not have sufficient resolution to characterize individual flow sources that often contribute to the same plume higher in the water column [*Bemis et al.*, 2002; *Di Iorio et al.*, 2012].

1.4.2. Eddy and particle tracking

Flow velocities have been estimated by tracking an eddy or a particle against a vertical scale [*Macdonald et al.*, 1980; *Rona and Trivett*, 1992]. Entrained particle rise time in the plume is measured over short distances. These devices are simplistic, but give rise to uncertainties. We report 3 measurements at MEF using a similar device (Figure 1.1a) created by *Ramondenc et al.*, [2006] that isolates a sample portion of the hydrothermal flow. The device includes a scale that is oriented parallel to the plume and the particles entrained within the plume are video recorded to calculate rise time.

This method assumes particles follow straight paths along the centerline of the plume, however, particles are often entrained in turbulent eddies or obscured within the plumes. This limits the number of viable particle to record, particularly within more vigorously venting grey or black smokers [*Ramondenc et al.*, 2006]. Additionally, particles are video recorded from a ROV or submersible and measurements are a function of the pitch and yaw of the camera.

These uncertainties may lead to variability in recorded data. At East Pacific Rise 21°N, *Macdonald et al.* [1980] originally recorded a heat flux up to 250 MW at one edifice. *Macdonald* [1983] later adjusted this flux value to approximately 60 MW across four chimneys on the edifice, which is still 1 to 2 orders of magnitude greater than subsequent flowmeter measurements (0.5–10 MW at East Pacific Rise 21°N; see section 1.4.6) [*Converse et al.*, 1984].

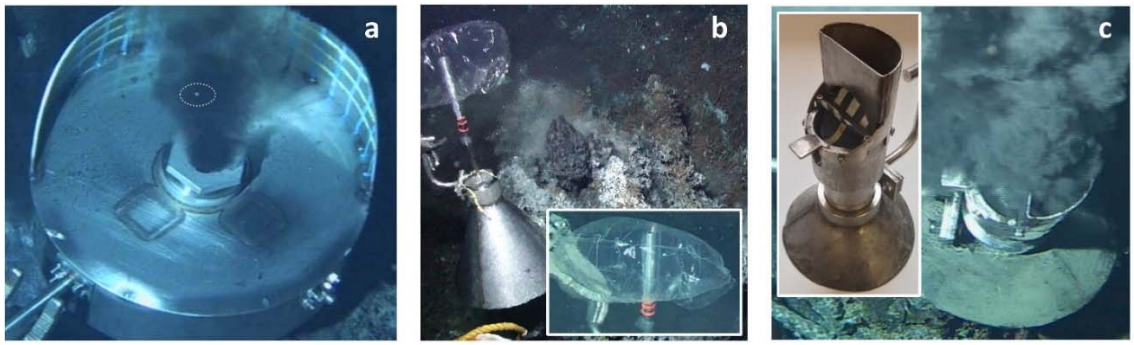

Figure 1.1. (a) Flow velocity measurement at a black smoker orifice on Dante, Main Endevour field, Juan de Fuca (*Alvin* dive 4350). A particle (within the dotted circle) is tracked on the frames of the video during the dive. The flow rate of the 330°C hydrothermal fluid from the orifice of 5 cm diameter was 20 cm/s, while the heat output was 0.5 MW (measurement 3 in Table 1.1). (b) Hydrological seepage meter modified for the hydrothermal flow conditions at the ocean floor and deployed vertically over a small chimney during *Alvin* dive 4411 to Dante, Main Endevour field, Juan de Fuca. The flow rate of the 80°C hydrothermal fluid from the orifice of 1 cm diameter was 2 cm/s, while the heat output was only 0.5 kW (measurement 1 in Table 1.1). Hydrothermal fluid is captured by a collection bag (inset). (c) Anemometer device (inset) that predates the cup anemometer developed in this work (section 1.4.5). The paddle rotates on an axis with a length of 5 cm. The device is deployed on the Bio 9 structure, East Pacific Rise 9°50'N, during *Alvin* dive 4403 (measurement 11 in Table 1.1).

1.4.3. Acoustic and particle tracking

Various acoustic methods have been used to quantify diffuse and focused hydrothermal flow. Velocity measurements have been determined by monitoring the backscatter of an acoustic pulse on small suspended particles [*Palmer*, 2005; *Palmer and Rona*, 2005] or turbulent temperature

fluctuations [*Ross and Lueck*, 2003; *Ostashev and Wilson*, 2015]. The Doppler Effect has been applied to calculations of the vertical velocity field [*Jackson et al.*, 2003]. The acoustic scintillation method of measuring forward scattered signals has been used to quantify the temporal fluctuations of hydrothermal flow at the Main Endeavour field [*Xu and Di Iorio*, 2011; *Di Iorio et al.*, 2012].

Crone et al. [2008] describe a visual image-based technique to estimate the velocity in a turbulent plume (such as a black smoker) that they term optical plume velocimetry. They apply the method to laboratory experiments and conclude that temporal cross correlation of adjacent pixels provides sensitive estimates of mean flow velocity in the plume. *Mittelstaedt et al.* [2016] developed a camera system and quantified diffuse discharge at ASHES vent field using Diffuse Flow Velocimetry.

1.4.4. Seepage meters

Seepage meters are designed to measure the exchange of the water across sediment-water interfaces in streams [*Rosenberry*, 2008]. A seepage bag protects against potential crossflows and the fluid moving along a hydraulic gradient is captured in a storage bag. Low temperature diffuse flow rate measurements were conducted in this work using a seepage meter [e.g., L. C. Murdoch, private communication, 2008] modified to ocean floor hydrothermal flow conditions (Figure 1.1b). This meter resulted in reliable data (measurement 1 in Table 1.1), but limited applicability. The seepage meter can only be used once per dive (at least, without sophisticated changes) and high temperature and velocity flows are likely to damage the bag.

1.4.5. Anemometers

Sarrazin et al. [2009] estimated diffuse flow rates at the Lucky Strike vent field, MAR using a duel sensor system. A Constant Voltage Anemometer [*King*, 1914] measured the difference in plume temperature and the ambient temperature, which is proportional to the effluent flow rate. Additionally, a flow visualizer attached to the anemometer independently measured the particle rise time through video imagery, similar to [*Macdonald et al.*, 1980; *Rona et al.*, 2002; *Ramondenc et al.*, 2006].

We report 4 measurements using a single paddle anemometer flow meter (Figure 1.1c) developed and used on several occasions [e.g., *Germanovich et al.*, 2015]. The rotor axis is

perpendicular to the flow and supported by jewel bearings also used in subsequent designs. The meter is particularly easy to use in transparent or semi-transparent flows (such as white or grey smokers and diffuse flow). In black smoker flows, however, the rotations are difficult to register visually (although not impossible; Table 1.1, measurements 11 through 14). A further 51 measurements were performed using a lightweight (approximately 2 kg) cup anemometer device (Figure 1.2 and 1.3). The open bearing support allows fluid to pass freely through the bearing and minimizes mineral precipitation experienced in more traditional hydrothermal settings [e.g., *Futrell*, 1989; *Vaughn et al.*, 2006]. Device walls protect the paddle wheels from potential cross flow (Figure 1.3c). Detailed explanation of instrument construction is explained by *Genc*, [2012].

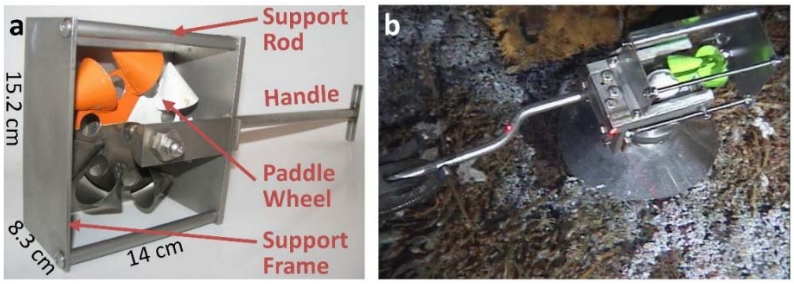

Figure 1.2. (a) Cup anemometer device developed by *Genc* [2012]. The paddle wheel and anemometer cups are fabricated from a titanium alloy; all other parts are made from stainless steel grade 316. Cups of the paddle wheel were painted to enhance the visualization process. A handle is attached to the frame for deployment from an occupied submersible or ROV. After *Genc* [2012] and *Germanovich et al.*, [2015]. (b) Cup anemometer device deployed at a diffuse flow site (Dante, Main Endeavor field, *Alvin* dive 4411).

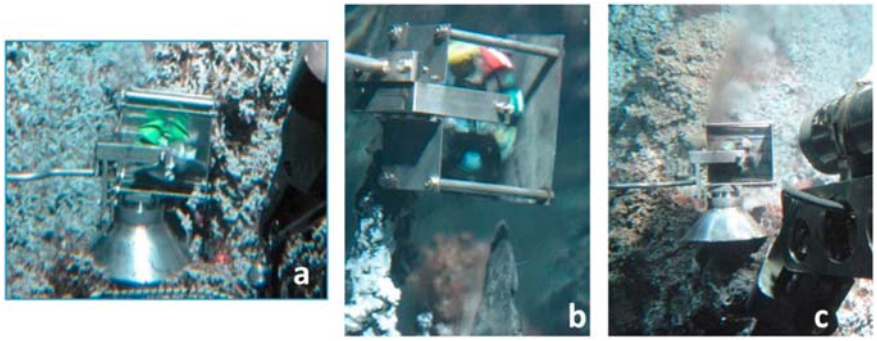

Figure 1.3. Deployment of the cup anemometer (a) over a low-temperature diffuse flow site (covered with tubeworms) on *Alvin* dive 4412 at the Clam Bed vent field, Endeavour segment, Juan de Fuca (measurement 61 in Table 1.2), (b) over a white smoker chimney on *Alvin* dive 4452 to Hulk, Main Endevour field (measurement 47 in Table 1.2), and (c) over a black smoker orifice on *Alvin* dive 4414 to Hulk, Main Endevour field (measurement 33 in Table 1.2). The black smoker flow is affected by cross flow upon exiting the device. Near the orifice, however, the device walls protect the flow (once the device is properly oriented) making the measurements closer to the calibration conditions (section 1.5). Images modified from Figure 2.4 and 2.13 of *Genc* [2012].

In the case of diffuse flow, flow is calculated by backtracking to the full area at the cone base (Figure 1.2b, similar to *Sarrazin et al.* [2009]). For focused flow, the concentrator covered the vent orifice, so that the flow was exiting the orifice near the main part of the device (Figure 1.3c). The device is deployed over the fluid discharge site (Figure 1.3) from either a manned submersible or ROV. Fluid flows into the anemometer and paddle rotations are recorded by the submarine's video cameras. The rotation rate is determined postdive from video records by counting paddle wheel rotations within a known amount of time. Linear flow velocity is obtained from the calibration curve constructed from lab test results (section 1.5). The device is held at a given site for a few minutes to insure that a sufficient number of revolutions are recorded.

1.4.6. Flowmeters

Converse et al. [1984] and *Ginster et al.* [1994] measured focused discharge using a commercial, electromagnetic turbine flowmeter at the East Pacific Rise and Juan de Fuca, respectively. *Schultz et al.* [1992, 1996] developed both nonmechanical (using electromagnetic induction) and mechanical (a spinning rotor) meters for measuring diffuse effluent velocities and temperatures. These devices were installed for several days to create a time series of velocity and temperature. *Schultz et al.* [1992] conducted the first direct measurements of diffuse flow on the Peanut structure in the southern part of the MEF. Sea trials of these turbine flow meters encountered issues with the failure of electronic components [e.g., *Converse et al.*, 1984; *Converse*, 1985; *Ginster et al.*, 1994] and particle precipitation within the bearings [e.g., *Ginster et al.*, 1994].

We report 40 measurements and discuss the performance of two turbine flowmeters (TFMs) with identical principle components, except for rotor assemblies. *Genc*, [2012] oversaw the original construction of these devices. TFM1 is designed for use in high temperature focused flow and TFM2 is optimized for use in low temperature diffuse flow. An observation wheel attached to rotor extrudes above and outside the flow tube. Fluid flow angled to the turbine blades exerts a torque that initiates and maintains rotation. The rotations are recorded using standard *Alvin* or

ROV video equipment and counted postidive by advancing video images at the matching frame rate. Multiple counts are performed over the full time interval of each measurements and the average rotation rate is calculated (see section 1.6.4 on temporal variability). In instances of velocities exceeding 150 cm/s the video images are advanced frame by frame with

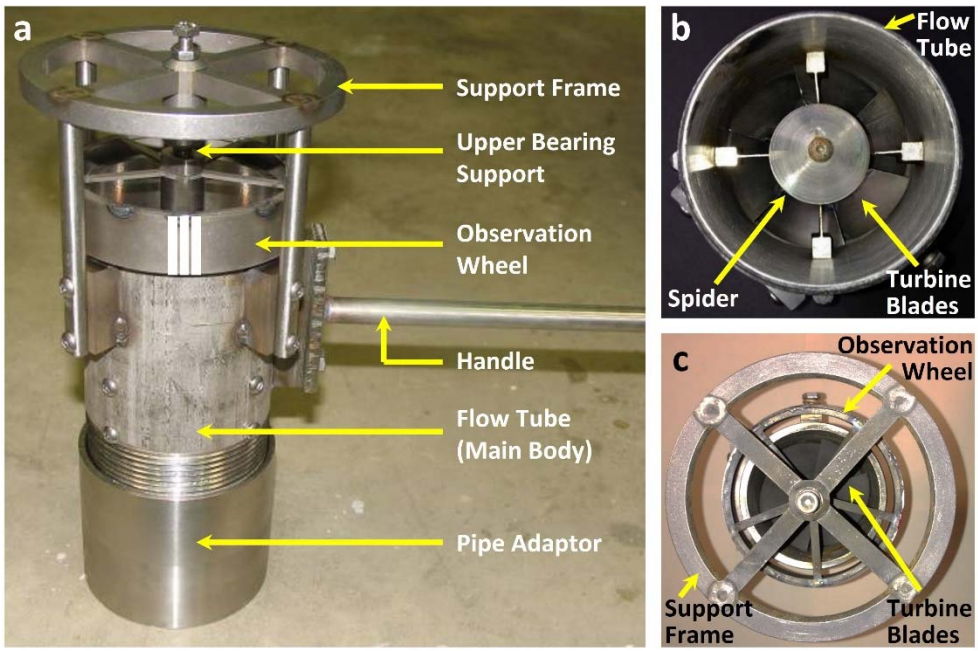

Figure 1.4. (a) Turbine flowmeter TFM1 and its components. After *Genc* [2012] and *Germanovich et al.*, [2015]. (b) Bottom (with pipe adaptor removed) and (c) top views.

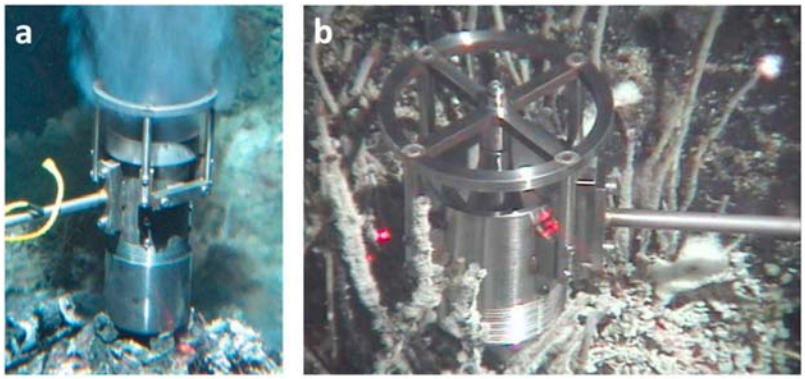

Figure 1.5. (a) Deployment of TFM1 at a black smoker on the Fairy Castle vent structure at the High Rise vent field (*Alvin* dive 4526). After *Genc* [2012] and *Germanovich et al.*, [2015]. The fluid flow rate was 114.1 cm/s (measurement 18 in Table 1.3). (b) TFM2 deployed at a diffuse flow site at the Ventor vent structure in the High Rise vent field (*Alvin* dive 4620) [*Genc*, 2012; *Germanovich et al.*, 2015]. Distance between two red laser beams, indicated by the red dots, is 10 cm (although in this case, the distance between the red dots is greater than that since the dots are not located on a plane perpendicular to the beams). The velocity of the diffuse fluid was 2.1 cm/s (measurement 25 in Table 1.3).

a precision of 0.07 s. Rotation rates are converted to linear velocity using calibration curves (section 1.5).

A pipe adapter was used on TFM1 during the measurements on black smokers to protect the rotor from occasional chimney debris and allows the high-velocity flow to better approach the stable pattern before it enters the rotor zone. The adapter was not used for diffuse measurements with TFM2 to reduce the distance between the rotor assembly and source. The calibration tests for TFM1 and TFM2 (section 1.5) were conducted with and without the pipe adapter, respectively.

1.5. Calibration

The cup anemometer and flow meters underwent calibrations periodically throughout the deployment history of these devices. We employ standard methods for flowmeters in conventional pipe systems [e.g., *Webster*, 1999] to calibrate our devices in the hydraulics lab of Georgia Tech. The initial calibration was performed by *Genc*, [2012] and subsequent calibrations were performed both pre- and post-dive [e.g. *Germanovich et al.*, 2015] using the same methodology. A representative black smoker orifice was constructed from horizontal piping (inner diameter of 52.5 mm) located inside a transparent flume (Figure 1.6a). The devices were placed near the pipe opening, at a distance comparable to the measurement distance using submersibles. The cup anemometer and TFM1 were calibrated at flow velocities ranging from 27 to 141 cm/s and 25 to 249 cm/s, respectfully to mimic the rates expected of hydrothermal venting [e.g., *Ramondenc et al.*, 2006]. Rotation rates were determined during the test using a stroboscope [e.g., *van Veen*, 1977].

To calibrate TFM2 at flow velocities characteristic for diffuse hydrothermal flow [e.g., *Ramondenc et al.*, 2006; *Sarrazin et al.*, 2009], we used an experimental setup for flow velocities between 2 and 10 cm/s first developed by *Genc* [2012] and *Germanovich et al.*, [2015]. A 5 gal bucket is modified to act as a water reservoir. Water enters the base of the bucket through a 5 cm inlet pipe at a constant rate (Figure 1.6b). TFM2 is attached to this pipe in a vertical position. Water freely flows out through a hole in the top of the bucket to keep the container completely filled. The number of rotations were counted visual to the nearest half rotation over a known time interval. This process was repeated for several time intervals.

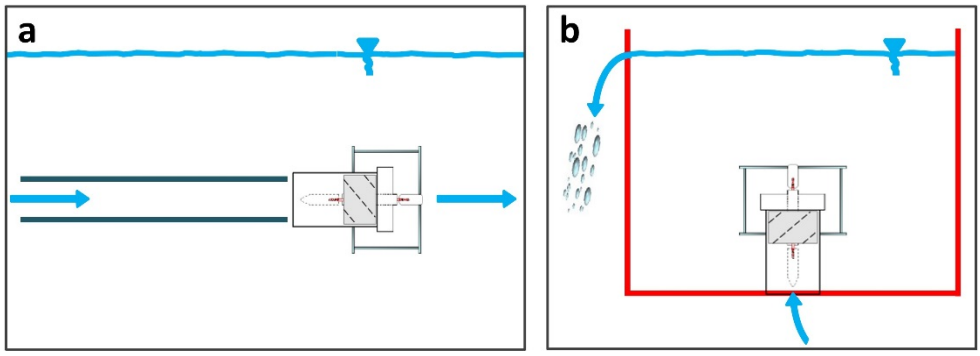

Figure 1.6. (a) Schematic of TFM1 calibration setup in the hydraulic flume. The rotations were simultaneously monitored by a stroboscope and a video camera. The number of revolutions corresponding to a certain flow rate was then determined postexperiment by using the recorded video imagery. The calibration curve shown in Figure 1.7a was constructed based on these measurements. (b) Schematic of the laboratory setup for calibrating TFM2 at low flow rates. Calibrations were performed in a container by changing the flow rates from the water faucet. The relatively slow rotations were videotaped, visually counted, and plotted on the calibration curve (Figure 1.7b) for velocities ranging from 2 to 10 cm/s.

Restricted instrument storage space on *Alvin* or *Jason* typically limits each dive to only one flow meter. On occasion, TFM2 is used to measure the discharge of focused transparent and semitransparent flows. Therefore, TFM2 was also calibrated in the same laboratory setup as the cup anemometer and TFM1 for higher velocities, up to 53 cm/s. Interpolation between the low and high velocity calibrations results in the same calibration line.

A linear dependence of calibration data results in

$$w = w_0\left({}^{v}/_{v_0} - 1\right) \tag{1.1}$$

where w is the number of rotations per unit time and v is the linear flow velocity [*Genc*, 2012; *Germanovich et al.*, 2015]. The fitting parameters are $w_0 = 1.710$ rpm and $v_0 = 1.389$ cm/s for the cup anemometer, $w_0 = 18.326$ rpm and $v_0 = 8.238$ cm/s for TFM1, and $w_0 = 8.192$ rpm and $v_0 = 1.953$ cm/s for TFM2. The coefficient of correlation, r^2, always exceeds 0.98. Rotations are initiated at velocities exceeding v_0. For all calibrations, $v_0 > 0$ and $w_0 > 0$.

In some instances, measurement results (in Tables 1.2 and 1.4) are extrapolated beyond the calibration range of the flowmeters, which is acceptable due to the linear calibration curves (Figure 1.7). In instances of very low discharge during field tests, only unsteady, quasiperiodic rotations occurred, indicating that flow through the meters was not sufficiently strong to rotate the meter blades continuously. In this case, using equation (1.1) (or its inverse) yields the lower limit of flow velocity that corresponds to the measured time-averaged rotation rate. In such cases,

the results should be viewed as lower estimates of flow rates. These estimates, however, are probably quite close to the actual discharge rates (section 1.6.1).

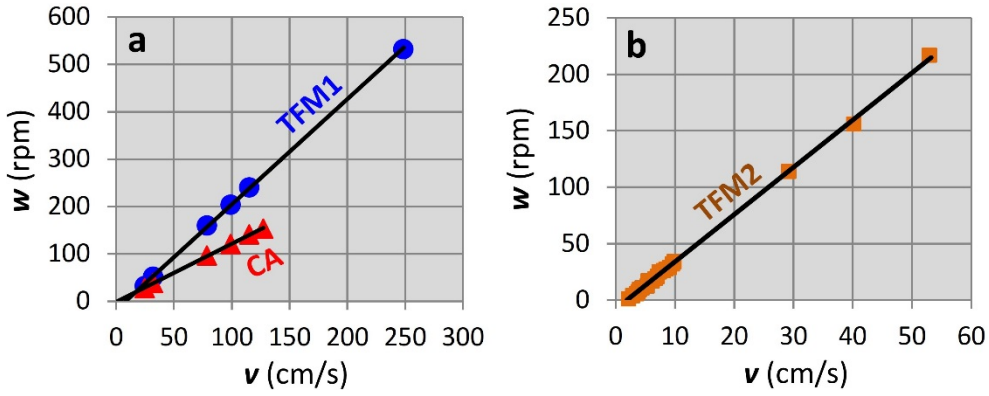

Figure 1.7. Calibration results for (a) the TFM1 device (circles) and cup anemometer (triangles) and (b) the TFM2 device (squares). The calibration lines shown are from postcruise calibrations. Precruise calibrations differ by less than 5% from the postcruise calibrations.

1.6. Sea trial performance

Regardless of fluid temperature, *focused flow* regime refers to sites with a discrete source area and *diffuse flow* regime applies to measurements made on obscured source areas. The orifice sizes are estimated from video footage using *Alvin*'s red laser beams (spaced at the fixed distance of 10 cm; see also caption to Figure 1.5) and other appropriately oriented scales such as marked metal rods or the jaws of *Alvin*'s manipulators. In the case of black smokers, it is rare when the inner side of the orifice can actually be seen, but in several occasions, we were able to bring the upper part of the chimney on board and compare the actual orifice geometry, determined by slicing the samples, to that measured based on the video. We concluded that the resulting error in measuring the orifice area was approximately 20%, which also applies to the measurements with turbine flowmeters described below. A temperature sensor on the ROV or submarine directly measures ambient seawater and the centerline discharge temperature immediately before or after velocity measurements. The heat output is calculated over the total area of discharge from

$$H = C_f v(T_f - T_a)A \tag{1.2}$$

where $C_f \approx 4 \times 10^6\ \mathrm{J/(m^3 \times °C)}$ is the volumetric heat capacity of the fluid ($C_f = C_p \rho_f$) [e.g., *Sun et al.*, 2008; *Sharqawy et al.*, 2010]. v is the fluid velocity, $T_f - T_a$ is the difference in temperature between that of hydrothermal vent fluid, T_f, and ambient seawater, T_a, and A is the

area of the discharge site, such as a black smoker orifice or patch of diffuse flow [*Genc*, 2012; *Germanovich et al.*, 2015].

Sources of error are derived from: (1) mechanical characteristics of the flowmeters or (2) uncertainties associated with field conditions [*Genc*, 2012; *Germanovich et al.*, 2015]. Sea trials showed that both devices performed successfully and required little (if any) post-dive shipboard maintenance such as cleaning the components, repainting the observation mark or adjusting spring tension. The unique open sapphire jewel bearing system [e.g., *Genc*, 2012; *Germanovich et al.*, 2015] allows fluid to travel pass the bearing limiting particle precipitation and clogging on the critical parts of the device (i.e., sapphire bearings) to negligible amounts. The bearings of the cup anemometer are occasionally replaced on a cruise, while the TFMs do not require replacement of bearings over this same time period.

Genc [2012] and *Germanovich et al.*, [2015] determined that the TFMs are more robust instruments than the cup anemometer and sturdier during transport or deployment by a submersible. The axis of the TFMs are oriented parallel to fluid flow, resulting in axial thrust as the primary load. In comparison, the axis of the cup anemometer is perpendicular to fluid flow, requiring a radial load to initiate rotation. This results in a higher preload to initiate rotations and induces greater wear on the bearings of the cup anemometer [*Genc*, 2012; *Germanovich et al.*, 2015]. The closed-structure frame of the TFM prohibits any potential crossflow during measuring (e.g., Figure 1.5a), but may increase the rate of particle precipitation along the stainless steel tubing.

When the venting fluid becomes saturated, minerals will precipitate to some degree on whatever surface is present. Titanium is frequently used in the seawater environment because it is generally less reactive than steel and shows little or no corrosion. It may not be possible to completely prevent mineral deposition as some nucleation spots may be available even on a very smooth titanium surface. Hence, in addition to replacing the stainless steel with titanium, mineral deposition can be minimized during long-term deployments by minimizing entrainment of ambient seawater.

1.6.1. Flowmeter performance

The devices constructed by *Genc* [2012] can be characterized similar to flow measurements in pipe systems [e.g., *Hochreiter*, 1958; *Baker et al.*, 1993; *Webster*, 1999; *Baker*, 2000]. Typically,

turbine flowmeters are calibrated over a range of viscosities. This may be represented as a universal viscosity curve, where the sensitivity, or K factor, is a function of the log of the ratio of output frequency to kinematic viscosity [*Gannon*, 1994]. This method requires sets of flow rates of fluids with differing viscosities. The factor $K = w/Q$, where w is the flow rate and Q is the flow rate, show be linear within its acceptable range for one set of fluid properties. This range is $0.1Q_{max}$ to Q_{max} for typical flowmeter design criteria, where Q_{max} is the maximum designed flow rate. To calibrate our devices, we use tap water at room temperatures. The strong linear relationship of the calibration curves for our devices (Figure 1.7) suggests these devices are operating within standard design specifications for such flowmeters.

Potential causes of inaccurate velocity measurements are likely the result of differences of density and viscosity (due to the effect of fluid temperature and pressure) between lab calibration and field conditions. The density of hydrothermal discharge is approximately 40% lower than that of the room temperature water used during flowmeter calibration, resulting in up to a 15% error [*Baker*, 1993]. The viscosity of high temperature hydrothermal fluids may approach values one order of magnitude less than the room temperature tap water used in the calibration. In experiments conducted by *Cuthbert and Beck*, [1999], an order-of-magnitude change of the liquid viscosity resulted in the change of K of approximately 10%. Therefore, even when the field conditions are significantly different than the calibration conditions, the overall error in measured velocity is not expected to exceed 30% at black smokers [*Genc*, 2012; *Germanovich et al.*, 2015]. The error in the measurement of diffuse flow velocity is likely to be considerably smaller. Compared to flow metering in industrial pipes, where the attainable measurement error could be as low as 0.1% [e.g., *Webster*, 1999; *Baker*, 2000], the level of accuracy in our devices may appear to be relatively low. This level of accuracy is acceptable in the seafloor hydrothermal environment, however, because assumptions regarding conditions in the field may be more problematic than inaccuracies resulting from the flowmeters themselves. Fluid flow rates likely vary with time over tidal cycles and as a result of changes in bottom currents. Our flowmeters could capture these variations or obtain long-term mean flow rates if they are deployed for longer periods of time.

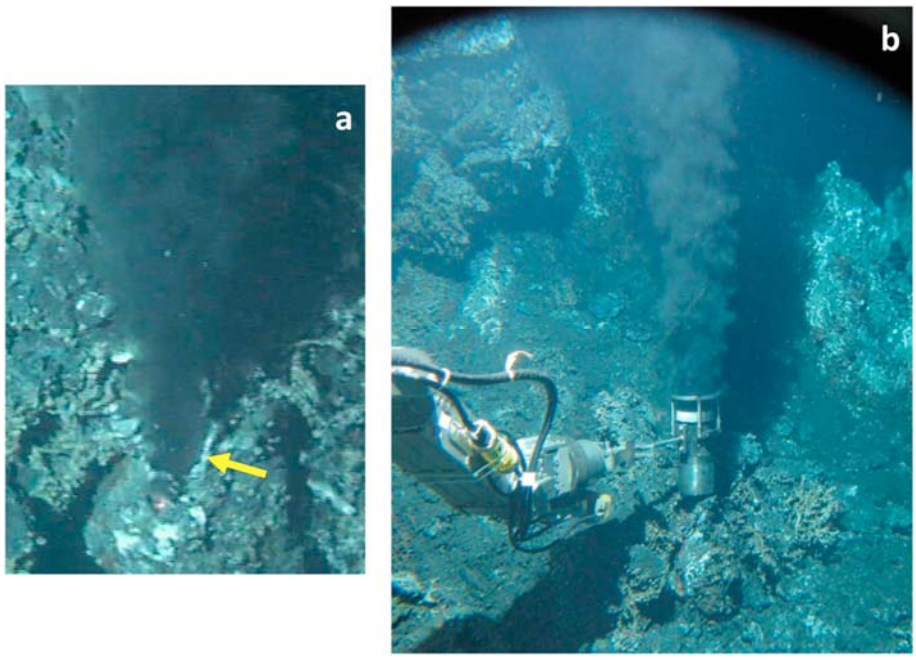

Figure 1.8. (a) Focused flow (orifice denoted by the arrow) at the Dante structure (Main Endevour field, *Alvin* dive 4518) located at X = 4999 m, Y = 6135 m (47°56.9446'N, 129°5.8591'W), at the depth of Z = 2179 m. No reliable in-hull, long-baseline (LBL) navigation was achieved during dive 4518, so these local *Alvin* coordinates are the Doppler fixes with several surface LBL and USBL corrections applied during the dive. (b) TFM1 device deployed at this black smoker [*Genc*, 2012; *Germanovich et al.*, 2015]. The measured flow velocity was 84.0 cm/s (measurement 1 in Table 1.3).

1.6.2. Field conditions

Difficulties of working on the seafloor may affect measurement accuracy. Currently, the sampling of black smoker vents on large vent structures and throughout the vent field is incomplete, and to obtain estimates of heat flow on the vent structure or vent field scale requires extrapolation of the limited data set. Discharge velocities are translated to volumetric flow rates by visually estimating orifice diameter (or area in cases of elongated fissures), which is dependent on available reference objects and submersible camera pitch. Radially symmetric plumes are assumed for calculations. Our estimate of the corresponding uncertainty is approximately 20% (section 1.6), whereas *Ginster et al.* [1994] assumed an uncertainty of ±5%. *Tivey and Singh* [1997] used X-ray computer tomography to study the morphology of the flow channels in black smoker chimneys. Their results suggest that orifice areas calculated assuming a circular geometry could be underestimated by 32% (on average by 16%; see Figure 1.2a in *Tivey and Singh* [1997]).We conclude that the accumulation of these issues results in heat outputs estimates that are likely accurate to within ±50%.

Source areas for diffuse flow are typically larger than the cross sectional area of the flowmeters. Measured velocities are extrapolated to the total area of diffuse patches. Figure 1.9a shows how the area of a diffuse flow patch is assessed and suggests that the estimates could differ by up to 50%. As a result, heat output estimates using these devices are uncertain by roughly a factor of 2 [*Genc*, 2012; *Germanovich et al.*, 2015]. This accuracy is similar to that of integrated and plume measurements [*Baker*, 2007].

During cup anemometer measurements, another source of error can come from cross flow that distorts the flow of the plume passing the anemometer wheel [*Genc*, 2012; *Germanovich et al.*, 2015]. Hence, the anemometer needs to be properly oriented to minimize this effect (Figure 1.3c). Nevertheless, the closed-structure frame of the TFMs mostly contains the hydrothermal flow within the device (Figure 1.5a and 1.8b).

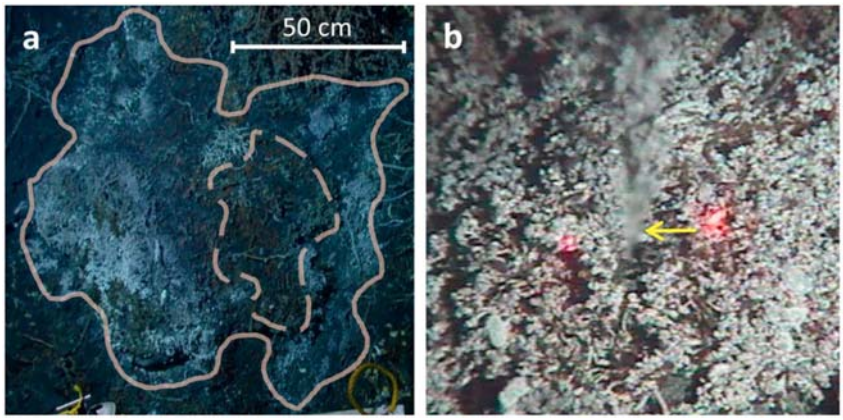

Figure 1.9. (a) Diffuse flow site near Dante structure (MEF, *Alvin* dive 4518) at *X* = 5005 m, *Y* = 6168 m (47°56.9527'N, 129°5.8793'W), and *Z* = 2194 m. TFM1 measured a flow velocity of 13.1 cm/s (measurement 2 in Table 1.3). White microbial mats visualize the area of diffuse venting, which is between the solid and dashed lines indicating its outer and inner borders, respectively [*Genc*, 2012; *Germanovich et al.*, 2015]. The shimmering water was distinctly observed above this area and was not visible outside, where no live biological activity could be detected. The area, 7100 cm^2, of this diffuse venting site was used in equation (1.2). We carefully analyzed this site, and it is unlikely that any measurable diffuse flow is venting from the area inside the dashed perimeter, but it cannot be entirely excluded. If this area were included in the calculation, the final result would differ by approximately 50%. (b) Vertical, low-temperature focused flow (indicated by arrow) within a diffuse flow site at *X* = 4954 m, *Y* = 6153 m (47°56.9543'N, 129°5.8952'W), and *Z* = 2188 m (Grotto, MEF, *Alvin* dive 4627). The source area of focused flow is defined by the orifice circumference while the source area of diffuse flow is estimated by bio prominence. TFM2 measured a flow velocity of 2.0 cm/s (measurement 9 in Table 1.3).

1.6.3. Temporal variability

Natural temporal variability of hydrothermal flow represents another source of inaccuracy if the measurement goal is the time-averaged fluxes. The cup anemometer and turbine flowmeters provide near instantaneous measurements of fluid velocity. Table 1.3, dives 4518 and 4525, shows that repeat TFM1 measurements at the same location at Dante a week apart resulted in variance of heat flux of approximately 10%, indicating that the device has a reasonably good degree of precision. Another example is given in Figure 1.10, where the measured flow velocities are plotted during the time interval of several minutes. This example shows that the transient flow rate fluctuations within a few minutes can be as large as 15%, which is consistent with data in Table 1.1 in *Ramondenc et al.* [2006]. Over longer time periods, temporal variations in velocity may be significantly greater due to tidal cycles and changes in the subsurface [*Genc*, 2012; *Germanovich et al.*, 2015]. *Schultz et al.* [1996] measured diffuse flow at the TAG hydrothermal field to range from approximately 0.48 cm/s to 0.57 cm/s and temperatures ranging from approximately 13.5°C to 150°C over the course of two and three-fourths days. For diffuse venting at the ASHES hydrothermal field, *Mittelstaedt et al.* [2016] measured a range of velocity and temperatures from 0.5 to 6 cm/s and 0°C to 6.5°C above ambient over 12 days of continuous measurements.

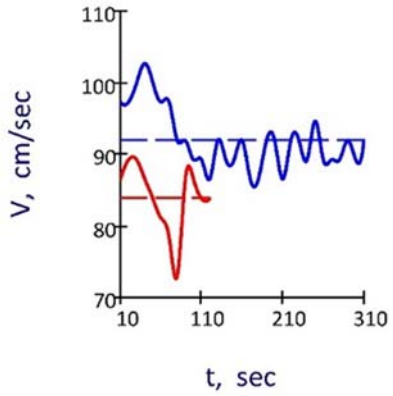

Figure 1.10. Velocity-time dependence measured with TFM1 at the orifice of a black smoker vent (Figure 1.8b) during *Alvin* dives 4518 and 4525 (red and blue lines, respectively). The shown velocity is averaged over the time window of 10 s. Red and blue dashed lines show the time-averaged velocities V_0 = 84.0 cm/s and V_0 = 92.0 cm/s, respectively (measurements 1 and 3 in Table 1.3).

1.6.4. Sea trials

The cup anemometer and turbine flowmeters were tested during five oceanographic expeditions from 2008 to 2014. The cup anemometer was deployed on eight *Alvin* dives on cruise AT15-34 to the Endeavour segment of Juan de Fuca in 2008. On this cruise, a total of 35 measurements of fluid flow were obtained at vent structures in the MEF, Mothra field, and Clam Bed vent field (Figure 1.11). An additional 29 flow rate measurements were obtained during nine *Alvin* dives on cruise AT15-36 at the MEF, Mothra vent field, and Axial Seamount (Figure 1.11). Results of measurements with the cup anemometer device are given in Table 1.2. The cup anemometer was designed with the intent to be used at black smokers, thus, measurements were dominantly conducted at high-temperature vents.

TFM1 was tested during four *Alvin* dives on cruise AT15-47 to Juan de Fuca in 2009, where a total of nine focused and diffuse flow measurements were made at the MEF and the High Rise field, and five *Alvin* dives on cruise AT15-67 to Juan de Fuca in 2010, where a total of ten focused and diffuse flow measurements were made at Endeavour (MEF, Mothra, and High Rise field) and Middle Valley (Dead Dog field). One diffuse flow measurement was taken at the Axial Seamount on an *Alvin* dive during cruise AT15-47 using TFM2. TFM2 was also deployed on three *Alvin* dives during cruise AT15-67 when eight flow measurements were conducted at MEF and Axial Seamount. The devices were further tested in 2014 during three *Jason* dives on cruise AT26-10 to the East Pacific Rise (9°50'N) where four and eight measurements were taken using TFM1 and TFM2, respectively. Results obtained with TFM1 and TFM2 are given in Table 1.3 and 1.4.

Locations of measurements reported in Table 1.1 through 1.4 were originally recorded in the local *Alvin* coordinate set X (south-north) and Y (west-east). All measurements were conducted in the Universal Transverse Mercator (UTM) zone 9 [e.g., *Snyder*, 1987]. The local X and Y are the geodetic easting and northing adjusted by applying a false easting and false northing, respectively, to the standard UTM zone 9 projection based on the WGS84 datum [e.g., *Grafarend and Krumm*, 2006]. False easting and false northing for 2008, 2009, and 2010 cruises were the same, which resulted in the same local origins for these years. For dives at the Endeavour segment, the local origin is at 47.89390°N, 129.16450°W, at the Axial Seamount at 45.90000°N, 130.06670°W, and at Middle Valley at 48.41667°N, 128.73333°W. The local origin of measurements is at 9.13330°N, 104.33330°W (UTM zone 13) for the East Pacific Rise 9°50' and 9°39.5'. At Lau Basin [e.g., *Tivey et al.*, 2012], the local origin is at 20.36670°S, 176.20000°W for the Tow Cam vent field and is at

20.83330°S, 176.26670°W for the Autonomous Benthic Explorer (ABE) vent field (both at UTM zone 1).

In general, locations of flow sources on the deep ocean hydrothermal structures often tend to be transient with venting being sealed (shut down) in some locations and reappearing in neighboring locations. Hence, it is likely that at least some flow sources registered in Table 1.1 through 1.4 do not exist anymore. In addition, due to the navigational issues on some dives (e.g., Figure 1.5 in caption), it was not possible to convert all recorded local coordinates to the geodetic coordinates. Therefore, in Table 1.1 through 1.4 we present the geodetic coordinates of hydrothermal structures rather than those of individual vents. That the vents were indeed located on the structures as presented in Table 1.1 through 1.4 were verified by markers that were available for all reported structures.

Devices are carefully inspected between dives. On occasion, the bearing of the cup anemometer required replacement. Any potential particle precipitation was removed from stainless steel components and fresh paint was applied to cups darkened by particle accumulation [*Genc,* 2012; *Germanovich et al.*, 2015]. The TFM devices were carefully inspected but did not require any maintenance during cruises. Temperature measurements were not always recorded due to malfunctions to *Alvin's* temperature probe. In these instances, heat output is estimated using temperature values obtained on the same structure during different dives. Some of the data from both the cup anemometer and turbine flowmeters have been presented by *Germanovich et al.* [2009] and *Genc* [2012] and all the data were published .

The turbine designs performed successfully in both high-temperature focused flow and low-temperature diffuse flow areas [*Genc*, 2012; *Germanovich et al.*, 2015]. A minimum velocity of 2 cm/s was measured at Grotto (measurements 6 and 9 in Table 1.3). To the best of our knowledge, this is the lowest flow rate ever measured at the Juan de Fuca ridge. We obtained a velocity of 198.6 cm/s with TFM1 at a black smoker on the Godzilla structure in the High Rise vent field (measurement 19 in Table 1.3). Therefore, the flow rate at Juan de Fuca can be at least as low as 2 cm/s and at least as high as 199 cm/s. We also apply our calibration to the previous measurements with our devices of the first direct heat output measurements at the High Rise hydrothermal field [*Germanovich et al.*, 2009; *Holden et al.*, 2009] and Main Endeavour [*Genc*, 2012], Endeavour segment (Table 1.3; *Germanovich et al.*, 2015]).

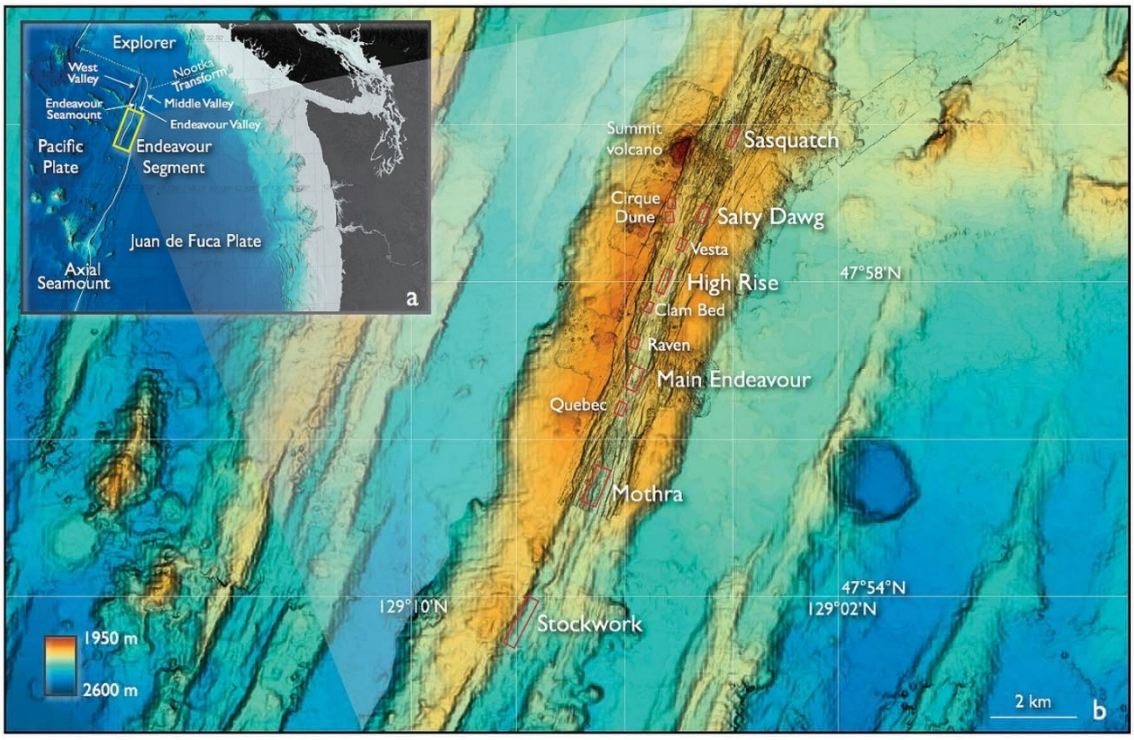

Figure 1.11. (a) Locations of the Endeavour segment, Axial Seamount, and Middle Valley [*Kelley et al.*, 2012] on the Juan de Fuca ridge. (b) Bathymetry map of the Endeavour segment showing hydrothermal vent fields [*Kelley et al.*, 2012].

1.7. Discussion

It is useful to compare the flow measurements and heat outputs we obtained with estimates made using other means. At high-temperature vents, velocity measurements using the cup anemometer and turbine flowmeters ranged between 5.9 and 199 cm/s. These values are generally in line with other direct measurements. For example, for black smokers, particle tracking measurements at ASHES ranged between 20 and 90 cm/s [*Rona and Trivett*, 1992], between 10 and 30 cm/s at East Pacific Rise 9°50'N [*Ramondenc et al.*, 2006], and between 1 and 5 m/s at East Pacific Rise 21°N [*Macdonald et al.*, 1980]. Early turbine flowmeter measurements have ranged between 70 and 236 cm/s at East Pacific Rise 21°N sites [*Converse et al.*, 1984] and between 68 and 337 cm/s on the Juan de Fuca ridge [*Ginster et al.*, 1994]. Estimates of diffuse flow discharge have ranged from values as low as 1.1 and 4.9 mm/s at the substrate level at Lucky Strike [*Sarrazin et al.*, 2009], 5 mm/s at TAG [*Schultz et al.*, 1996], to 4 cm/s at East Pacific Rise 9°50'N [*Ramondenc et al.*, 2006] and between 7 to 15 cm/s at the Peanut structure in the MEF [*Schultz et al.*, 1992].

Diffuse effluent along a single crack at ASHES was measured to vary between 0.1 and 5.8 cm/s [*Mittelstaedt et al.*, 2016]. These estimates of diffuse flow are generally similar to our measurements of low-temperature venting (focused or diffused), which ranged between 2 and 17.5 cm/s (Table 1.1 through 1.4).

Comparison of heat output estimates is somewhat more difficult, however. For example, *Bemis et al.* [1993] found that the median heat flux per black smoker vent was 9 MW and 3 MW for the Endeavour (18 vents) and Southern (18 vents) segments, respectively, and the total heat flux from high-temperature venting at these Juan de Fuca segments was estimated as 239 MW and 66 MW, respectively. *Ginster et al.* [1994] obtained heat outputs for individual black smoker vents ranging between 0.9 and 42 MW for the MEF with an average value of 6.2 MW/vent. In contrast, our measurements (Table 1.2 and 1.3) obtained an average of 1.8 MW/vent at Hulk from 16 high-temperature ($T > 140°\mathrm{C}$) focused vents and 1.3 MW/vent at Dante from 25 high-temperature focused vents. Four measurements on Dante with devices preceding our TFMs and cup anemometer (Table 1.1) resulted in the average heat output of 0.52 MW/vent. In general, it appears that our flow measurements show lower heat output than those obtained nearly two decades earlier by *Bemis et al.* [1993] and *Ginster et al.* [1994]. This may reflect the general decline in heat output in MEF. Measurements using Autonomous Benthic Explorer in 2000 yielded approximately 600 MW [*Veirs et al.*, 2006], whereas repeat measurements in 2004 yielded approximately 300 MW for MEF [*Thompson et al.*, 2005].

Our flowmeter measurements made at a high-temperature vent in the Dead Dog and Puppy Dog mounds in Middle Valley, Juan de Fuca, resulted in advective heat outputs of 20 MW (measurement 27 in Table 1.3), 19 MW (measurement 28 in Table 1.3), and 0.41 MW (measurement 5 in Table 1.1), respectively. Using plume theory, *Stein and Fisher* [2001] measured the advective heat flux from 10 individual vents in Middle Valley (eight at Dead Dog and two at Bent Hill sites) to be in the range of 1.4–39.6 MW with the mean value of 9 MW. Our result is in agreement with *Stein and Fisher* [2001] range. Thermal anomalies registered by [*Baker et al.*, 1987] at the Dead Dog site were consistent with a 6.5 MW heat source, which may be representative of the advective heat flux in the Middle Valley approximately 25 years ago. The somewhat higher value measured by *Stein and Fisher* [2001] for the mean vent heat discharge may be indicative of the increased advective heat budget a decade later. In turn, the mean value of our measurements, 13 MW, may be an indication that advective heat output at Middle Valley

has continued to increase. It is difficult to determine definitely, however, based on our three measurements in two locations.

Ramondenc et al. [2006] presented the measurement results obtained in 2004, shortly before the 2005–2006 East Pacific Rise eruption at 9°50'N [e.g., *Rubin et al.*, 2012]. Focused, high-temperature discharges were measured at structures Bio 9, M-vent, P-vent, and Tica both in 2004 [*Ramondenc et al.*, 2006] and 2014 (Table 1.4). In 2004, each of these structures had several orifices with a typical heat output of 1 MW per orifice. In 2014, M-vent and Tica did not have any high-temperature venting at all. P-vent had two white smokers and one grey with the mean heat output of 0.29 MW per orifice (Table 1.4). Venting at Bio 9 appears to have increased compared to the 2004 level, however, as the black smoker measurement obtained in 2014 also indicates a heat output of the order of 1 MW per high-temperature vent and, visually, the Bio 9 structure had several vigorous black smoker clusters. Overall, the high-temperature, advective heat output from Bio 9 is estimated to be tens of megawatts, which is several times greater than the 9 MW estimated in 2004 [*Ramondenc et al.*, 2006]. Furthermore, it appears that Bio 9 alone now vents at the same order of heat output as the entire 9°50'N hydrothermal field did in 2004 (42 MW). It is possible that the high-temperature, advective flow has become more channelized, predominately discharging through the Bio 9 structure.

Although our data are somewhat limited, they do provide some ground truth for flow estimates made using acoustic or optical methods described in section 1.4.3. For example, using acoustic scintillation methods, *Xu and Di Iorio* [2011] estimate the heat output at Dante to be approximately 62 MW. The data shown in Table 1.2 and 1.3 represent only about half (and, possibly, less) of the vents on Dante. If the data are extrapolated to encompass all the high-temperature vents, the heat output obtained using the flowmeter data would be a minimum of 50 MW.

Finally, by making direct measurements of flow at both focused and diffuse flow vents, one can, in principle, obtain estimates of the partitioning between focused and diffuse flows [e.g., *Ramondenc et al.*, 2006] as well as estimates of geochemical transports in focused and diffuse flow settings [*Lowell et al.*, 2013]. For example, using an in situ mass spectrometer (ISMS), concentrations of CO_2 (aq), CH_4, and H_2 were measured at a number of high-temperature and diffuse flow vents at MEF and Mothra [*Wankel et al.*, 2011] where we also made fluid flow and temperature measurements. The combination of the fluid flow and ISMS measurements showed that geochemical fluxes from diffuse flow sites could equal or exceed those from focused high-

temperature sites and that the flux of H_2 from diffuse flow vents was much less than expected, suggesting utilization by biota [*Wankel et al.*, 2011].

1.8. Conclusion

We calibrated and field tested a cup anemometer and two turbine flowmeter devices for making direct measurements of both focused and diffuse fluid flows in seafloor hydrothermal systems. The manned submersible *Alvin* (30 dives) and ROV *Jason* (3 dives) were used to obtain 104 separate measurements conducted at depths up to 2511 m and at temperatures up to 363°C. In sea trials, the turbine flowmeters successfully measured velocities ranging between 2 and 198.6 cm/s. The cup anemometer device operated between 7.6 and 88.1 cm/s. The rate of 2 cm/s is the lowest ever measured at the Juan de Fuca ridge, and the results obtained with our devices (Table 1.3) represent the first direct heat output measurements at the High Rise hydrothermal field, Endeavour segment, and the Dead Dog vent area, Middle Valley, on the Juan de Fuca ridge. The first direct measurements of the diffuse flow rates at most of the structures on the northern part of the Main Endeavour Field (Dante, Hulk, Grotto, and S&M) were also obtained with our devices.

The data reported by *Ramondenc et al.* [2006] for the East Pacific Rise at 9°50'N is considerably expanded by the measurements reported in Table 1.4. This work also reports (Table 1.1) the first direct flow and heat measurements at the 9°39.5'N hydrothermal area on the East Pacific Rise, at the Tow Cam and ABE vent fields in the Lau Basin, and at the Puppy Dog mound in the Middle Valley. These measurements were obtained with devices that predated the flowmeters described in this work and were used in the process of their development.

The cup anemometer and flowmeters were able to take quick measurements (on the scale of minutes) and require minimal maintenance pre- or post-dive. Their open bearing design [*Genc*, 2012; *Germanovich et al.*, 2015] allows limits mineral precipitation, allowing for use during long-term deployment. Although the cup anemometer is simpler and easier to manufacture, our experience favors the turbine meters. For example, entrainment of the fresh seawater into the hydrothermal flow within the TFM devices is minimal compared to measurements with the cup anemometer. As a result of their robust modular design, the TFM devices could incorporate a variety of electronic sensors.

We report direct measurements of flow velocity over two orders of magnitude in multiple hydrothermal vent settings using a multitude of instruments. Specifically, we discuss the performance of a new cup anemometer and TFM devices designed to explore a broad range of heat and chemical fluxes at oceanic spreading centers. The ability of these devices to accurately preform multiple measurements on an individual dive fills an important niche as the literature is currently severely limited on hydrothermal flow velocity.

1.9. Tables

Table 1.1. Results of flow rate and heat output measurements at the Main Endeavour field and Middle Valley, Juan de Fuca ridge, and at Lau Basin performed with devices that preceded the flowmeters described in [*Genc*, 2012; *Germanovich et al.*, 2015].

Measure-ment	*Alvin* dive	Depth (m)	Flow regime	Flow velocity (cm/sec)	Temper-ature (°C)	Orifice diameter (cm)	Source area (cm^2)	Flow rate (cm^3/sec)	Heat output (kW)
Main Endeavour Vent Field (Endeavour)									
Dante (47° 56.9527'N, 129° 5.8793'W)									
1	4411	2,192	Focused	2.0[a]	80	1	0.8	1.6	0.5
2	4348	2,176	Focused	24.6[b]	333	6.2	30.2	743	984
3	4350	2,181	Focused	19.9[b]	330	5	19.6	390	512
4	4350	2,181	Focused	36.8[b]	312	4	12.6	464	575
Middle Valley									
Puppy Dog Mound (48° 26.8778'N, 128° 42.2538'W)									
5	4351	2,414	Focused	19.6[b]	269	5	19.6	384	410
Lau Basin									
Marker 7, Tow Cam vent field (20° 19.0017'S, 176° 8.1768'W)									
6	233[d]	2,704	Focused	116[b]	318.6	4	12.6	1,460	1,850
7	233[d]	2,706	Focused	37[b]	316.9	3	7.1	263	331
Site 8, ABE (20° 45.9835'S, 176° 11.5867'W)									
8	234[d]	2,132	Focused	58[b]	289.1	3	7.1	412	473
9	234[d]	2,130	Focused	100[b]	350	6	28.3	2,830	3,940
East Pacific Rise									
9°39.5'N (9°39.5344'N, 104°15.7147'W)									
10	4280	2,543	Focused	110[b]	378	4	12.6	1,390	2,090
Bio 9 (9°50.3056'N, 104°17.4764'W)									
11	4403	2,504	Focused	74[c]	341	6	28.3	2,090	2,840
12	4405	2,504	Focused	33[c]	358	3	7.1	234	334
13	4407	2,504	Focused	40[c]	350	3	7.1	284	395
P-vent (9°50.2720'N, 104°17.4640'W)									
14	4403	2,506	Focused	71[c]	374	5	19.6	1,390	2,070
15	4575	2,509	Diffuse	2.0[b]	20[e]		1,850	3,700	268
Tica (9°50.3981'N, 104°17.4927'W)									
16	4580	2,512	Diffuse	5.8[b]	20[e]		1,220	7,080	512

[a] Velocity measured with a seepage meter (Figure 1.1b) modified to hydrothermal flow conditions at mid-oceanic ridges

[b] Velocity measured using the particle tracer (Figure 1.1a)

[c] Velocity measured using an anemometer device (Figure 1.1c) that predated the cup anemometer (section 1.4.5)

[d] *Jason* dives

[e] Temperature is inferred from additional measurements at the same vent

Table 1.2. Flow rate and heat output measurements performed with the cup anemometer device at the Endeavour segment and Axial Seamount on the Juan de Fuca ridge.

Measure-ment	*Alvin* dive	Depth (m)	Flow regime	Flow velocity (cm/s)	Temper-ature (°C)	Orifice diameter (cm)	Source area[a] (cm^2)	Flow rate (cm^3/s)	Heat output (kW)
Main Endeavour vent field (Endeavour)									
Crypto (47°56.9797'N, 129°5.8191'W)									
1	4452	2,201	Focused	71.1	328.3	7	38.5	2,740	3,570
Dante (47°56.9527'N, 129°5.8793'W)									
2	4415	2,191	Focused	53.5	318.6	2.5	4.9	262	332
3	4421	2,197	Focused	12.5	201	3.6	10	130	100
4	4421	2,176	Focused	57.1	330[b]	8	50.3	2,870	3,770
5	4422	2,174	Focused	21.2	335.7	3	7.1	150	200
6	4422	2,175	Focused	6.2	333.3	4	12.6	78.1	104
7	4422	2,175	Focused	7.9	330[b]	2	3.1	24.5	32.1
8	4422	2,175	Focused	10.3	330[b]	1.5	1.8	18.5	24.3
9	4422	2,175	Focused	4.2	142	1	0.8	3.4	1.9
10	4422	2,175	Diffuse	10.2	312		12.6	129	159
11	4422	2,184	Focused	4.2	225	5.6	24.6	103	92
12	4422	2,185	Focused	24.5	328	8	50.3	1,230	1,610
13	4422	2,185	Focused	19.9	300.7	7	38.5	766	916
14	4422	2,182	Focused	65.8	333.1	4	12.6	829	1,100
15	4422	2,181	Focused	46.1	334.7	4	12.6	581	773
16	4422	2,186	Focused	8.5	251	1.2	1.1	9.4	9.3
17	4422	2,180	Focused	21.2	310	5	19.6	416	512
18	4439	2,176	Focused	26.7	327.5	8.3	54.1	1,440	1,880
19	4439	2,176	Focused	63.0	325	5	19.6	1,230	1,600
20	4441	2,185	Focused	45.1	328.9	7	38.5	1,740	2,270
21	4447	2,175	Focused	63.4	325.7	8.5	56.7	3,590	4,660
22	4447	2,175	Focused	59.0	322.9	6	28.3	1,670	2,140
23	4452	2,176	Focused	7.6	163	4	12.6	95.8	61.7
24	4452	2,176	Focused	24.1	249	3	7.1	171	169
Grotto (47°56.9473'N, 129°5.9114'W)									
25	4439	2,187	Focused	40.4	330[b]	7	38.5	1,560	2,040
26	4439	2,185	Focused	44.3	324	6	28.3	1,250	1,620
27	4439	2,189	Focused	35.0	330	6	28	980	1,290
28	4439	2,187	Focused	45.5	334	7.9	49	2,230	2,960
29	4441	2,200	Diffuse	4.2	20[b]		2,400	10,100	730
Hulk (47°57.0067'N, 129°5.8272'W)									
30	4414	2,186	Focused	18.4	322	7	38.5	708	907
31	4414	2,186	Focused	45.1	322	7	38.5	1,740	2,220
32	4414	2,187	Focused	46.0	313	3.9	11.9	550	680
33	4414	2,186	Focused	17.4	312	8	50.3	875	1,090
34	4414	2,192	Focused	72.1	320.3	5.6	25	1,800	2,300
35	4416	2,193	Focused	20.0	146	8	50.3	1,010	580
36	4416	2,192	Focused	12.1	321.1	8.5	56.7	686	876
37	4416	2,192	Diffuse	11.5	257		19.6	225	230
38	4416	2,184	Focused	16.7	278.4	2.7	5.7	95.2	105
39	4416	2,188	Diffuse	17.5	272.4		95	1,660	1,800
40	4416	2,188	Focused	28.3	279	6	28.3	801	888
41	4416	2,189	Diffuse	12.4	304.3		50.3	624	754

Table 1.2. (continued)

Measure-ment	*Alvin* dive	Depth (m)	Flow regime	Flow velocity (cm/s)	Temper-ature (°C)	Orifice diameter (cm)	Source area[a] (cm^2)	Flow rate (cm^3/s)	Heat output (kW)
42	4420	2,186	Focused	20.6	160	4	12.6	260	160
43	4421	2,191	Focused	88.1	320	9	63.6	5,600	7,130
44	4447	2,189	Focused	11.1	309.3	5	19.6	218	268
45	4449	2,197	Focused	13.1	15.5	4.5	16	210	11
46	4452	2,192	Focused	53.8	327.7	3.5	9.6	516	673
47	4452	2,191	Focused	14.6	85.1	4	12.6	184	61.2
48	4452	2,188	Focused	28.8	320.1	4	12.6	363	462
S&M 2008 (47°56.8718'N, 129°5.9194'W)									
49	4446	2,189	Diffuse	12.1	20[b]		78.5	950	68.8
TP (47°56.9716'N, 129°5.8593'W)									
50	4420	2,194	Focused	13.7	118.9	2	3.1	42.5	19.9
51	4447	2,174	Focused	4.2	337.3	5	19.6	82.3	110
52	4447	2,173	Focused	61.6	330[b]	6	28.3	1,740	2,290
53	4447	2,174	Focused	16.7	330[b]	4	12.6	210	276
54	4452	2,191	Focused	82.6	333.7	3.7	10.8	892	1,180
Mothra vent field (Endeavour)									
Faulty Towers (47°55.4202'N, 129°6.5372'W)									
55	4418	2,277	Focused	78.5	312.9	10	78.5	6,160	7,670
56	4418	2,277	Focused	58.9	314.9	14	154	9,070	11,400
57	4450	2,271	Focused	82.5	321.3	13	133	11,000	14,000
58	4450	2,276	Focused	54.8	324	11	95.0	5,210	6,710
59	4450	2,171	Diffuse	9.6	107		177	1,700	714
Stonehenge (47°55.2666'N, 129°6.5814'W)									
60	4450	2,290	Focused	50.0	309.5	5	19.6	980	1,210
Clam Bed vent field (Endeavour)									
(47°57.7837'N, 129°5.4822'W)									
61	4412	2,186	Diffuse	11.2	228		479	5,360	4,850
62	4412	2,187	Diffuse	11.5	277		133	1,530	1,680
Axial Seamount									
Vixen (45°55.0338'N, 129°59.5881'W)									
63	4444	1,521	Focused	44.1	333	5.3	22.1	975	1,290
Diva (45°55.5784'N, 129°58.7485'W)									
64	4445	1,522	Focused	13.1	280[b]	5.5	24	310	350

[a]Source area for diffuse flow estimated by bio prominence

[b]Temperature is inferred from additional measurements at the same vent

Table 1.3. Flow rate and heat output measurements performed with the TFM1 and TFM2 devices at the Endeavour segment, Axial Seamount, and Middle Valley on the Juan de Fuca ridge.

Measure-ment	*Alvin* dive	Depth (m)	Device	Flow regime	Flow velocity (cm/s)	Temper-ature (°C)	Orifice diameter (cm)	Source area[a] (cm^2)	Flow rate (cm^3/s)	Heat output (kW)
Main Endeavour vent field (Endeavour)										
Dante (47°56.9527'N, 129°5.8793'W)										
1[b]	4518	2,179	TFM1	Focused	84.0	336	4.5	15.9	1,340	1,780
2	4518	2,194	TFM1	Diffuse	13.1	12		7,100	93,000	3,760
3[b]	4525	2,179	TFM1	Focused	92.0	338	4.5	15.9	1,460	1,970
4	4526	2,181	TFM1	Focused	98.8	327	7.9	49.0	4,840	6,300
Grotto (47°56.9473'N, 129°5.9114'W)										
5	4621	2,188	TFM1	Focused	40.1	290	3.4	9.1	365	421
6	4622	2,188	TFM2	Diffuse	2.0	13.9		1,090	2,180	105
7	4626	2,186	TFM1	Focused	134.0	320	7.9	49.0	6,570	8,400
8	4627	2,190	TFM2	Diffuse	5.9	20		1,580	9,320	675
9	4627	2,188	TFM2	Focused	2.0	20.3	2	3.1	6.2	0.5
10	4627	2,188	TFM2	Diffuse	12.7	42.6		50	635	103
Hulk (47°57.0067'N, 129°5.8272'W)										
11	4627	2,193	TFM2	Diffuse	2.1	15.9		1,770	3,720	208
12	4627	2,193	TFM2	Diffuse	9.8	14.8		4,530	44,400	2,290
13	4626	2,199	TFM1	Focused	51.1	306	4.1	13.2	675	820
14	4626	2,192	TFM1	Focused	151.3	310	7.8	47.8	7,200	8,900
Mothra vent field (Endeavour)										
Faulty Towers (47°55.4202'N, 129°6.5372'W)										
15	4628	2,278	TFM1	Focused	76.1	318	9	63.6	4,840	6,120
High Rise vent field (Endeavour)										
Bambi (47°58.1173'N, 129°5.2181'W)										
16	4623	2140	TFM1	Focused	155.1	337	8	50.3	7,800	10,460
Boardwalk (47°58.1075'N, 129°5.2294'W)										
17	4623	2,134	TFM1	Focused	59.5	324	5.2	21.2	1,260	1,630
Fairy Castle (47°58.0266'N, 129°5.2896'W)										
18	4526	2,158	TFM1	Focused	114.1	329	5	19.6	2,240	2,930
Godzilla (47°58.1183'N, 129°5.2415'W)										
19	4516	2,136	TFM1	Focused	198.6	349	10	78.5	15,600	21,600
Park Place (47°58.0913'N, 129°5.2695'W)										
20	4516	2,149	TFM1	Focused	57.4	315	4.2	13.9	798	999
21	4623	2,148	TFM1	Focused	31.2	250	4	12.6	393	390
Ventor (47°58.0589'N, 129°5.3779'W)										
22	4516	2,164	TFM1	Focused	138.4	332	3	7.1	983	1,300
23	4526	2,163	TFM1	Focused	135.2	333	4.5	15.9	2,150	2,850
Axial Seamount										
Marker 134 (45°56.1538'N, 129°58.8917'W)										
24	4620	1,517	TFM2	Diffuse	2.1	5		1,210	2,540	31.5
25	4620	1,517	TFM2	Diffuse	2.1	4.8		1,510	3,170	36.8
Marker 33/55 (45°55.9871'N, 129°58.9472'W)										
26	4521	1,520	TFM2	Diffuse	4.1	19.6		49	201	14.2

Table 1.3. (continued)

Measure-ment	*Alvin* dive	Depth (m)	Device	Flow regime	Flow velocity (cm/s)	Temper-ature (°C)	Orifice diameter (cm)	Source area[a] (cm^2)	Flow rate (cm^3/s)	Heat output (kW)
					Middle Valley					
Dead Dog Mound (48°27.3635'N, 128°42.5814'W)										
27	4625	2,406	TFM1	Focused	171.6	260	12	113	19,400	20,000
28	4625	2,399	TFM1	Focused	186.3	265	11	95	17,700	18,600

[a]Source area for diffuse flow estimated by bio prominence

[b]Measurements during *Alvin* dives 4518 and 4525 conducted on the same orifice

Table 1.4. Flow rate and heat output measurements performed with the TFM1 and TFM2 devices at 9°50'N on the East Pacific rise.

Measure-ment	*Jason* dive	Depth (m)	Device	Flow regime	Flow velocity (cm/s)	Temper-ature (°C)	Orifice diameter (cm)	Source area[a] (cm^2)	Flow rate (cm^3/s)	Heat output (kW)
East Pacific Rise										
P-vent (9°50.2720'N, 104°17.4640'W)										
1	758	2,509	TFM2	Diffuse	3.7	8.6		9,630	35,600	950
2	758	2,511	TFM1	Focused	45.0	284	1.5	1.8	81.0	91.4
3	758	2,499	TFM1	Focused	24.6	272.4	5	19.6	482	522
4	758	2,499	TFM1	Focused	21.0	165	5	19.6	412	269
Crab Spa (9°50.3975'N, 104°17.4883'W)										
5[b]	758	2,502	TFM2	Diffuse	9.8	16		314	3,080	174
6	758	2,502	TFM2	Diffuse	3.9	8.8		314	1,220	33.8
7[b]	758	2,502	TFM2	Focused	12.0	22.4	3.1	7.5	90.0	7.4
8[b]	758	2,502	TFM2	Diffuse	6.1	20.6		306	1,870	140
M-vent (9°50.7997'N, 104°17.5913'W)										
9	759	2,498	TFM2	Focused	2.8	24.2	1.5	1.8	5.0	0.4
Bio 9 (9°50.3056'N, 104°17.4764'W)										
10	760	2,505	TFM1	Focused	101.1	363	2.4	4.5	450	700
Tica (9°50.3981'N, 104°17.4927'W)										
11	758	2,511	TFM2	Diffuse	17.2	167		1,400	24,100	15,900
Colonizer CV61 (9°50.2766'N, 104°17.4718'W)										
12	758	2,506	TFM2	Focused	12.3	77.9	2.5	4.9	60.3	18.3

[a]Source area for diffuse flow estimated by bio prominence

[b]Measurements done at the same site. The flow appeared diffuse (measurement 5) before the organisms occupying the site were removed. After removal, a flow source (small fracture) was exposed (measurement 7), although a significant component of the diffuse flow (measurement 8) remained.

1.10. References

Baker, E. T. (1994), A 6-year time series of hydrothermal plumes over the Cleft segment of the Juan de Fuca Ridge, *J. Geophys. Res. Solid Earth*, *99* (B3), 4889–4904, doi:10.1029/93JB01030.

Baker, E. T. (2007), Hydrothermal cooling of midocean ridge axes: Do measured and modeled heat fluxes agree?, *Earth Planet. Sci. Lett.*, *263*, 140–150, doi:10.1016/j.epsl.2007.09.010.

Baker, E. T., and G. J. Massoth (1987), Characteristics of hydrothermal plumes from two vent fields on the Juan de Fuca Ridge, northeast Pacific Ocean, *Earth Planet. Sci. Lett.*, *85* (1–3), 59–73, doi:10.1016/0012-821X(87)90021-5.

Baker, E. T., G. A. Freely, and G. J. Massoth (1987), Hydrographic and chemical survey of hydrothermal plumes from the Middle Valley vent, *Eos Trans. AGU*, *68*(1325).

Baker, E. T., G. J. Massoth, S. L. Walker, and R. W. Embley (1993), A method for quantitatively estimating diffuse and discrete hydrothermal discharge, *Earth Planet. Sci. Lett.*, *118* (1–4), 235–249, doi:10.1016/0012-821X(93)90170-E.

Baker, E. T., G. J. Massoth, R. A. Feely, G. A. Cannon, and E. Thomson (1998), The rise and fall of the CoAxial hydrothermal site, 1993-1996, *103* (July 1993), 9791–9806.

Baker, R. C. (2016), *Flow Measurement Handbook*, 2nd ed., Cambridge University Press, Cambridge.

Beaulieu, S. E., E. T. Baker, C. R. German, and A. Maffei, An authoritative global database for active submarine hydrothermal vent fields, *Geochemistry, Geophys. Geosystems*, 14 (11), 4892-4905, doi: 10.1002/2013GC004998

Bemis, K. G., R. P. Von Herzen, and M. J. Mottl (1993), Geothermal heat flux from hydrothermal plumes on the Juan de Fuca Ridge, *J. Geophys. Res.*, *98* (B4), 6351–6365, doi:10.1029/92JB02273.

Bemis, K. G., P. A. Rona, D. R. Jackson, C. D. Jones, D. Silver, and K. Mitsuzawa (2002), A comparison of black smoker hydrothermal plume behavior at Monolith Vent and at Clam Acres Vent Field: Dependence on source configuration, *Mar. Geophys. Res.*, *23*, 81–96, doi:10.1023/A:1022484931681.

Boetius, A., and F. Wenzhöfer (2013), Seafloor oxygen consumption fuelled by methane from cold seeps, *Nat. Geosci.*, *6* (9), 725–734, doi:10.1038/ngeo1926.

Burd, B. J., and R. E. Thomson (1994), Hydrothermal venting at endeavour ridge: effect on zooplankton biomass throughout the water column, *Deep. Res. Part I*, *41* (9), 1407–1423, doi:10.1016/0967-0637(94)90105-8.

Butterfield, D. A., K. K. Roe, M. D. Lilley, J. A. Huber, J. A. Baross, R. W. Embley, and G. J. Massoth (2004), Mixing, reaction and microbial activity in the sub-seafloor revealed by temporal and spatial variation in diffuse flow vents at axial volcano, in *The Subseafloor Biosphere at Mid-Ocean Ridges*, edited by W. S. D. Wilcock, E. F. Delong, D. S. Kelley, J. A. Baross, and S. C. Cary, pp. 269–289, American Geophysical Union, Washington, D.C.

Carazzo, G., E. Kaminski, and S. Tait (2008), On the rise of turbulent plumes: Quantitative effects of variable entrainment for submarine hydrothermal vents, terrestrial and extra terrestrial explosive volcanism, *J. Geophys. Res.*, *113* (B9), B09201, doi:10.1029/2007JB005458.

Converse, D. R. (1985), Flow rates in the East Pacific Rise (21°N) hot springs, and numerical investigations of two regimes of hydrothermal circulation, Harvard Univ.

Converse, D. R., H. D. Holland, and J. M. Edmond (1984), Flow rates in the axial hot springs of the East Pacific Rise (21°N): Implications for the heat budget and the formation of massive sulfide deposits, *Earth Planet. Sci. Lett.*, *69* (1), 159–175, doi:10.1016/0012-821X(84)90080-3.

Cooper, M. J., H. Elderfield, and A. Schultz (2000), Diffuse hydrothermal fluids from Lucky Strike hydrothermal vent field: Evidence for a shallow conductively heated system, *J. Geophys. Res.*, *105* (B8), 19369–19375, doi:10.1029/2000JB900138.

Corliss, J. B. et al. (1979), Submarine thermal sprirngs on the Galapagos Rift, *Science (80-.).*, *203* (4385), 1073–1083, doi:10.1126/science.203.4385.1073.

Cowen, J. P., M. A. Bertram, S. G. Wakeham, R. E. Thomson, J. William Lavelle, E. T. Baker, and R. A. Feely (2001), Ascending and descending particle flux from hydrothermal plumes at Endeavour Segment, Juan de Fuca Ridge, *Deep Sea Res. Part I Oceanogr. Res. Pap.*, *48* (4), 1093–1120, doi:10.1016/S0967-0637(00)00070-4.

Crone, T. J., R. E. McDuff, and W. S. D. Wilcock (2008), Optical plume velocimetry: A new flow measurement technique for use in seafloor hydrothermal systems, *Exp. Fluids*, *45*(5), 899–915, doi:10.1007/s00348-008-0508-2.

Cuthbert, M. R., and S. B. M. Beck (1999), A non-dimensional method to increase the accuracy of turbine flowmeters, *Proc. Inst. Mech. Eng. Part E*, *213*, 121–126, doi:10.1243/0954408991529816.

Von Damm, K. L., and M. D. Lilley (2004), Diffuse flow hydrothermal fluids from 9° 50′ N East Pacific Rise: Origin, evolution and biogeochemical controls, in *The Subseafloor Biosphere at Mid-Ocean Ridges*, edited by W. Wilcock, E. F. Delong, D. S. Kelley, J. A. Baross, and S. Craig Cary, pp. 245–268, American Geophysical Union, Washington, D.C.

Dekas, A. E., R. S. Poretsky, and V. J. Orphan (2009), Deep-sea archaea fix and share nitrogen in methane-consuming microbial consortia, *Science*, *326* (5951), 422–426, doi:10.1126/science.1178223.

Edmond, J. M., J. B. Corliss, and L. I. Gordon (1979), Ridge crest-hydrothermal metamorphism at the Galapagos Spreading Center and reverse weathering, 383–390.

Fischer, H. B., E. J. List, R. C. Y. Koh, J. Imberger, and N. H. Brooks (1979), Turbulent jets and plumes, in *Mixing in Inland and Coastal Waters*, pp. 315–389, Academic Press, Inc., San Diego, California.

Gannon, J. (1994), Getting the most from turbine flowmeters, *Machine Design, 66* (11), 55-58.

Genc, G. (2012), Serpentinization-assisted deformation processes and characterization of hydrothermal fluxes at mid-ocean ridges, Georgia Institute of Technology.

Gendron, J. F., J. F. Todd, R. A. Feely, E. T. Baker, and D. C. Kadko (1994), Excess 222 Rn above the Cleft segment of the Juan de Fuca Ridge, *J. Geophys. Res. Solid Earth*, *99* (B3), 5007–5015, doi:10.1029/93JB03209.

Germanovich, L. N., D. Di Iorio, G. Genc, R. S. Hurt, R. P. Lowell, J. F. Holden, D. A. Butterfield, and E. Olsen, J. (2009), *Direct measurements of hydrothermal heat output at Juan de Fuca Ridge*, American Geophysical Union.

Germanovich, L. N., G. Genc, R. P. Lowell, and P. A. Rona (2012), Deformation and surface uplift associated with serpentinization at mid-ocean ridges and subduction zones, *J. Geophys. Res. Solid Earth*, *117* (7), 1–23, doi:10.1029/2012JB009372.

Germanovich, L. N., R. S. Hurt, J. E. Smith, G. Genc, and R. P. Lowell (2015), Measuring fluid flow and heat output in seafloor hydrothermal environments, *J. Geophys. Res. Solid Earth*, *120* (12), doi:10.1002/2015JB012245.

Ginster, U., M. J. Mottl, and R. P. Von Herzen (1994), Heat flux from black smokers on the Endeavour and Cleft segments, Juan de Fuca Ridge, *J. Geophys. Res.*, *99* (B3), 4937–4950, doi:10.1029/93JB02800.

Grafarend, E. W., and F. W. Krumm (2006), *Map projections, cartographic information systems*, Springer, Berlin.

Hinrichs, K.-U., and A. Boetius (2002), The anaerobic oxidation of methane: New insights in microbial ecology and biogeochemistry, in *Ocean Margin Systems*, pp. 457–477, Springer Berlin Heidelberg, Berlin, Heidelberg.

Hochreiter, H. M. (1958), Dimensionless correlation of coefficients of turbine type flow meters, *Trans. ASME*, *80*, 1363–1368.

Holden, J. F., D. A. Butterfield, and M. D. Lilley (2009), *Endeavour-Axial geochemistry and ecology research (EAGER), 2009 cruise, R/V Atlantis–DSV Alvin AT15-47, Endeavour Segment and Axial Volcano, Juan de Fuca ridge, Northeast Pacific Ocean, AT15-47 NeMO 2009 cruise report*.

Hunt, G. R., and T. S. van den Bremer (2011), Classical plume theory: 1937-2010 and beyond, *IMA J. Appl. Math.*, *76* (3), 424–448, doi:10.1093/imamat/hxq056.

Di Iorio, D., J. W. Lavelle, P. Rona, K. Bemis, G. Xu, L. Germanovich, R. Lowell, and G. Genc (2012), Measurements and models of heat flux and plumes from hydrothermal discharges near the deep seafloor, *Oceanography*, *25* (1), 168–179, doi:10.5670/oceanog.2012.14.

Jackson, D. R., C. D. Jones, P. A. Rona, and K. G. Bemis (2003), A method for Doppler acoustic measurement of black smoker flow fields, *Geochemistry, Geophys. Geosystems*, *4* (11), 1–12, doi:10.1029/2003GC000509.

James, C. F. (1989), Bucket wheel assembly for a flow measuring device, U.S. Patent 4,866,985.

Kelley, D. S. D. et al. (2012), Endeavour Segment of the Juan de Fuca Ridge: One of the most remarkable places on Earth, *Oceanography*, *25* (1), 44–61, doi:10.5670/oceanog.2012.03.

King, L. V. (1914), On the convection of heat from small cylinders in a stream of fluid: Determination of the convection constants of small platinum wires with applications to hot-wire anemometry, *Philos. Trans. R. Soc. A Math. Phys. Eng. Sci.*, *214* (509–522), 373–432, doi:10.1098/rsta.1914.0023.

Lang, S. Q., D. A. Butterfield, M. D. Lilley, H. Paul Johnson, and J. I. Hedges (2006), Dissolved organic carbon in ridge-axis and ridge-flank hydrothermal systems, *Geochim. Cosmochim. Acta*, *70* (15), 3830–3842, doi:10.1016/j.gca.2006.04.031.

Levin, L. A. et al. (2016), Hydrothermal vents and methane seeps: Rethinking the sphere of influence, *Front. Mar. Sci.*, *3* (72), 1–23, doi:10.3389/fmars.2016.00072.

Little, S. A., K. D. Stolzenbach, and R. P. Von Herzen (1987), Measurements of plume flow from a hydrothermal vent field, *J. Geophys. Res.*, *92* (B3), 2587–2596.

Liu, L., and R. P. Lowell (2009), Models of hydrothermal heat output from a convecting, crystallizing, replenished magma chamber beneath an oceanic spreading center, *J. Geophys. Res. Solid Earth*, *114* (B02102), doi:10.1029/2008JB005846.

Lowell, R. P., and L. N. Germanovich (1994), On the temporal evolution of high-temperature hydrothermal systems at ocean ridge crests, *J. Geophys. Res. Solid Earth*, *99* (B1), 565–575, doi:10.1029/93JB02568.

Lowell, R. P., and L. N. Germanovich (2004), Hydrothermal processes at mid-ocean ridges: Results from scale analysis and single-pass models, in *Mid-Ocean Ridges*, edited by C. R. German, J. Lin, and L. M. Parson, pp. 219–244, Washington, D.C.

Lowell, R. P., A. Farough, J. Hoover, and K. Cummings (2013), Characteristics of magma-driven hydrothermal systems at oceanic spreading centers, *Geochemistry, Geophys. Geosystems*, *14* (6), 1756–1770, doi:10.1002/ggge.20109.

Macdonald, K. C. (1983), A Geophysical comparison between fast and slow spreading centers: Constraints on magma chamber formation and hydrothermal activity, in *Hydrothermal Processes at Seafloor Spreading Centers*, pp. 27–51, Springer US, Boston, MA.

Macdonald, K. C., K. Becker, F. N. Spiess, and R. D. Ballard (1980), Hydrothermal heat flux of the "black smoker" vents on the East Pacific Rise, *Earth Planet. Sci. Lett.*, *48* (1), 1–7, doi:10.1016/0012-821X(80)90163-6.

Mittelstaedt, E., D. J. Fornari, T. J. Crone, J. Kinsey, D. Kelley, and M. Elend (2016), Diffuse venting at the ASHES hydrothermal field: Heat flux and tidally modulated flow variability derived from in situ time-series measurements, *Geochemistry, Geophys. Geosystems*, *17* (4), 1435–1453, doi:10.1002/2015GC006144.

Morton, B. R. (1957), Buoyant plumes in a moist atmosphere, *J. Fluid Mech.*, *2* (2), 127–144, doi:10.1017/S0022112057000038.

Morton, B. R., G. Taylor, and J. S. Turner (1956), Turbulent gravitational convection from maintained and instantaneous sources, *Proc. R. Soc. A Math. Phys. Eng. Sci.*, *234* (1196), 1–23, doi:10.1098/rspa.1956.0011.

Murdoch, L. C. (2008), Private communication

Murton, B. J., L. J. Redbourn, C. R. German, and E. T. Baker (1999), Sources and fluxes of hydrothermal heat, chemicals and biology within a segment of the Mid-Atlantic Ridge, *Earth Planet. Sci. Lett.*, *171* (2), 301–317, doi:10.1016/S0012-821X(99)00157-0.

Ostashev, V. E., and D. K. Wilson (2015), *Acoustics in Moving Inhomogeneous Media*, CRC Press, Boca Raton, Fla.

Palmer, D. R. (2005), Acoustical scattering from constituents of an ocean plume located near a boundary surface, *IEEE Trans. Geosci. Remote Sens.*, *43* (4), 770–777, doi:10.1109/TGRS.2005.844309.

Palmer, D. R., and P. A. Rona (2005), Acoustical imaging of deep ocean hydrothermal flows, in *Sounds in the sea: from ocean acoustics to acoustical oceanography*, pp. 551–563.

Papanicolaou, P. N., and E. J. List (1987), Statistical and spectral properties of tracer concentration in round buoyant jets, *Int. J. Heat Mass Transf.*, *30* (10), 2059–2071, doi:10.1016/0017-9310(87)90086-X.

Ramondenc, P., L. N. Germanovich, K. L. Von Damm, and R. P. Lowell (2006), The first measurements of hydrothermal heat output at 9°50'N, East Pacific Rise, *Earth Planet. Sci. Lett.*, *245*(3–4), 487–497, doi:10.1016/j.epsl.2006.03.023.

Rona, P. a., and D. A. Trivett (1992), Discrete and diffuse heat transfer atashes vent field, Axial Volcano, Juan de Fuca ridge, *Earth Planet. Sci. Lett.*, *109*, 57–71, doi:10.1016/0012-821X(92)90074-6.

Rona, P. A., and K. G. Speer (1989), An Atlantic hydrothermal plume: Trans-Atlantic Geotraverse (TAG) area, Mid-Atlantic ridge crest near 26°N, *J. Geophys. Res.*, *94*(B10), 13879–13893.

Rona, P. A., K. G. Bemis, D. Silver, and C. D. Jones (2002), Acoustic imaging, visualization, and quantification of buoyant hydrothermal plumes in the Ocean, *Mar. Geophys. Res.*, *23*, 147–168, doi:10.1023/A:1022481315125.

Rosenberry, D. O. (2008), A seepage meter designed for use in flowing water, *J. Hydrol.*, *359* (1–2), 118–130, doi:10.1016/j.jhydrol.2008.06.029.

Ross, T., and R. Lueck (2003), Sound scattering from oceanic turbulence, *Geophys. Res. Lett.*, *30* (6), 6–9, doi:10.1029/2002GL016733.

Rubin, K. H., S. A. Soule, W. W. Chadwick Jr., D. J. Fornari, D. A. Clague, and R. W. Embley (2012), Volcanic eruptions in the deep sea, *Oceanography*, *25* (1), 142–157, doi:10.5670/oceanog.2011.65.

Rudnicki, M. D., and H. Elderfield (1992), Theory applied to the Mid-Atlantic ridge hydrothermal plumes: the finite-difference approach, *J. Volcanol. Geotherm. Res.*, *50*, 161–172, doi:10.1016/0377-0273(92)90043-D.

Sarrazin, J., P. Rodier, M. K. Tivey, H. Singh, A. Schultz, and P. M. Sarradin (2009), A dual sensor device to estimate fluid flow velocity at diffuse hydrothermal vents, *Deep. Res. Part I Oceanogr. Res. Pap.*, *56* (11), 2065–2074, doi:10.1016/j.dsr.2009.06.008.

Schultz, A., J. R. Delaney, and R. E. McDuff (1992), On the partitioning of heat flux between diffuse and point source seafloor venting, *J. Geophys. Res.*, *97* (B9), 12299–12314, doi:10.1029/92JB00889.

Schultz, A., P. Dickson, and H. Elderfield (1996), Temporal variations in diffuse hydrothermal flow at TAG, *Geophys. Res. Lett.*, *23* (23), 3471–3474, doi:10.1029/96GL02081.

Sharqawy, M. H., J. H. Lienhard, and S. M. Zubair (2010), Thermophysical properties of seawater: a review of existing correlations and data, *Desalin. Water Treat.*, *16* (1–3), 354–380, doi:10.5004/dwt.2010.1079.

Snyder, J. P. (1987), *Map projections--a working manual*: *U.S. Geological Survey Professional Paper 1395*, Wasington, D.C.

Speer, K. G., and K. R. Helfrich (1995), Hydrothermal plumes: a review of flow and fluxes, *Geol. Soc. London, Spec. Publ.*, *87* (1), 373–385, doi:10.1144/GSL.SP.1995.087.01.29.

Spiess, F. N. et al. (1980), East Pacific Rise: Hot springs and geophysical experiments, *Science*, *207* (4438), 1421–1433, doi:10.1126/science.207.4438.1421.

Stein, J. S., and A. T. Fisher (2001), Multiple scales of hydrothermal circulation in Middle Valley, northern Juan de Fuca Ridge: Physical constraints and geologic models, *J. Geophys. Res. Solid Earth*, *106* (B5), 8563–8580, doi:10.1029/2000JB900395.

Sun, H., R. Feistel, M. Koch, and A. Markoe (2008), New equations for density, entropy, heat capacity, and potential temperature of a saline thermal fluid, *Deep Sea Res. Part I Oceanogr. Res. Pap.*, *55*, 1304–1310, doi:10.1016/j.dsr.2008.05.011.

Tennekes, H., and J. L. Lumley (1972), *A First Course in Turbulence*, The MIT Press, Cambridge, Massachusetts.

Thompson, W. J., R. E. McDuff, F. R. Stahr, D. R. Yoerger, and M. Jakuba (2005), Heat flux from the Endeavour segment of the Juan de Fuca ridge, in *Eos Trans. AGU, 86*.

Thomson, R. E., J. R. Delaney, R. E. McDuff, D. R. Janecky, and J. S. McClain (1992), Physical characteristics of the Endeavour ridge hydrothermal plume during July 1988, *Earth Planet. Sci. Lett.*, *111*, 141–154, doi:10.1016/0012-821X(92)90175-U.

Thomson, R. E., E. E. Davis, and B. J. Burd (1995), Hydrothermal venting and geothermal heating in Cascadia Basin, *J. Geophys. Res. Solid Earth*, *100* (B4), 6121–6141, doi:10.1029/95JB00030.

Tivey, M. K., and S. Singh (1997), Nondestructive imaging of fragile sea-floor vent deposit samples, *Geology*, *25* (10), 931–934, doi:10.1130/0091-7613(1997)025<0931:NIOFSF>2.3.CO.

Tivey, M. K., E. Becker, R. Beinart, C. R. Fisher, P. R. Girguis, C. H. Langmuir, P. J. Michael, and A.-L. Reysenbach (2012), Links from Mantle to Microbe at the Lau Integrated Study Site, *Oceanography*, *25* (1), 62–77, doi:10.5670/oceanog.2011.65.

Turner, J. S. (1986), Turbulent entrainment: The devlopment of the entrainment assumption, and its application to geophysical flows, *J. Fluid Mech.*, *173* (1986), 431–471, doi:10.1017/S0022112086001222.

Vaughn, E. C., J. M. Fulford, and H. R. Myers (2006), Bucket wheel assembly for fluid flow meters, U.S. Patent 7,017,425 B1.

van Veen, F. (1977), *Handbook of Stroboscopy*, Gen Rad Inc., Concord, Mass.

Veirs, S. R., R. E. McDuff, and F. R. Stahr (2006), Magnitude and variance of near-bottom horizontal heat flux at the Main Endeavour hydrothermal vent field, *Geochemistry, Geophys. Geosystems*, *7*(2), doi:10.1029/2005GC000952.

Vereshchaka, A. L., and G. M. Vinogradov (1999), Visual observations of the vertical distribution of plankton throughout the water column above Broken Spur vent field, Mid-Atlantic Ridge, *Deep. Res. Part I Oceanogr. Res. Pap.*, *46*(9), 1615–1632, doi:10.1016/S0967-0637(99)00018-7.

Wankel, S. D., L. N. Germanovich, M. D. Lilley, G. Genc, C. J. DiPerna, A. S. Bradley, E. J. Olson, and P. R. Girguis (2011), Influence of subsurface biosphere on geochemical fluxes from diffuse hydrothermal fluids, *Nat. Geosci.*, *4*(7), 461–468, doi:10.1038/ngeo1183.

Webster, J. G. (1999), *The Measurement, Instrumentation, and Sensors Handbook*, Springer, New York.

Winn, C. D., D. M. Karl, and G. J. Massoth (1986), Microorganisms in deep-sea hydrothermal plumes, *Nature*, *320*(6064), 744–746, doi:10.1038/320744a0.

Xu, G., and D. Di Iorio (2011), The relative effects of particles and turbulence on acoustic scattering from deep-sea hydrothermal vent plumes., *J. Acoust. Soc. Am.*, *130*(4), 1856–1867, doi:10.1121/1.3624816.

CHAPTER 2

CHARACTERIZING THE IN SITU STRAIN CAUSED BY SUBSURFACE INJECITON

2.1. Abstract

This work is concerned with monitoring fluid flow in geologic formations. In particular, there is significant concern on how to monitor the injection process during carbon storage and petroleum operations. Injection deforms the reservoir and confining units in a complex pattern that increases in magnitude and expands outward with time. Formation properties and pressure redistribution affect the deformation pattern, and this effect is possible to interpret from measurements of the strain tensor. In this work, we utilized a combination of analytical and numerical methods to develop models of the subsurface deformation induced by pressurized regions. Our models suggest monitoring instruments at significantly shallower depths than the reservoir are capable of measuring deformation signals generated during waterflooding or carbon sequestration operations. A function of multiple strain and tilt components is used to locate the zone of greatest signal strength. Modern borehole strainmeters are capable of measuring multiple components of strain and tilt, however, this technique has not been validated in the field. The first field test of this technique will occur during a waterflooding operation at the carbon storage analog site at the North Avant oil field in Osage County, OK. Numerical models of the poroelastic response to water injection are based on our geologic analysis of the North Avant field site. The results show it is possible to interpret the pressure distribution from measurements of the strain field in the shallow subsurface. Permeability is likely to vary within reservoirs, but the distribution is challenging to constrain without extensive testing. We investigate the deformation in the vicinity of regions of permeability change and our results suggest it is feasible to identify channels of high permeability using a spatial array of multiple measurements of strain and tilt. This is significant as such channels are common in petroleum formations of fluvial deposits and strongly affect the fluid flow pattern. Similar high permeability channels would allow faster injection rates and increased carbon storage capacity, but may result in unexpected fluid migration that could lead to CO_2 escape. It is therefore important to identify such channels in order to make informed decisions during CO_2 sequestration and petroleum operations.

2.2. Introduction

Carbon storage in geologic formations is a promising option to mitigate the rise of CO_2 in the atmosphere [*IPCC*, 2005], however, injecting CO_2 increases and redistributes the pressure in the formation. This may cause potentially damaging strains that should be avoided to prevent degrading the wellbore integrity (i.e. casing seal [*Crow et al.*, 2010]), reactivating faults [*Moeck et al.*, 2009; *Garagash and Germanovich*, 2012], or damaging the formation (i.e. generating faults [*Dusseault et al.*, 1998]). Further, the injected carbon must be retained within formations over long timescales for this storage method to be viable [*Verdon et al.*, 2013]. Monitoring is necessary to provide an early warning system of hazards during the injection process and to insure the long-term security of injected carbon. Currently, there is significant concern on how best to monitor carbon storage operations [e.g., *IPCC*, 2005; *Liu*, 2012]. One possible way to monitor fluid injection processes is by measuring subsurface deformation induced by pressure redistribution in reservoirs.

Fluid injection deforms the enveloping rocks in a complex pattern that increases in magnitude and expands outward with time [*Cappa and Rutqvist*, 2011; *Davis*, 2011; *Verdon et al.*, 2013; *Murdoch*, 2014]. Pressure redistribution and formation properties affect the deformation pattern, and this pattern may be possible to interpret from measurements of the strain field in the vicinity of the injection site [*Vasco et al.*, 2001, 2010; *Fabian and Kümpel*, 2003; *Iglesias and McLaughlin*, 2012; *Hesse and Stadler*, 2014; *DeWolf et al.*, 2015; *Murdoch et al.*, 2016]. Deformation reaches the ground surface, where surface displacements have been measured during injection processes [e.g., *Vasco et al.*, 2010], and interpreted for information on the subsurface permeability structure [e.g., *Vasco et al.*, 2001]. Measurements made in the subsurface [e.g., *Verdon et al.*, 2013] allow for strain recordings at shorter intervals and larger strain rates than typically possible for surface techniques. The construction of deep wells (at the depth of the reservoir) for instrument installation is challenging and costly, however, simulations indicate that injection into a reservoir may create strains that are measurable at relatively shallow depths (first several hundred feet of the subsurface) [*Murdoch et al.*, 2016]. Hence, reservoir properties and pressures may be inferred without drilling to reservoir depths for direct pressure or deformation measurements. Using multiple components of deformation are likely to better constrain interpretations of deformation, and modeling of typical conditions of carbon storage sites suggests it may be feasible to measure in-situ strains in cap rocks (Appendix A.2. and [*Murdoch et al.*, 2016]).

Borehole extensometers or strainmeters can measure in-situ strains during injection processes. Early developments in extensometers that record small deformations within a borehole [*Davis et al.*, 1969; *Gale*, 1975; *Gladwin*, 1984; *Martin et al.*, 1991; *Thompson and Kozak*, 1991] have led to more recent technical innovations. Portable extensometers designed to characterize displacements during well tests [*Vaughn et al.*, 2006; *Svenson et al.*, 2007; *Cappa and Rutqvist*, 2011; *Schweisinger et al.*, 2011] allowed for instruments to be removed after tests were completed. For example, *Hisz et al.* [2013] describes an instrument that combines an extensometer and a tiltmeter that can be temporarily anchored to borehole for measurements of both the vertical displacement and horizontal shear, or tilt. *DeWolf et al.* [2015] describes a removable strainmeter that can measure up to four components of strain and two components of tilt. In a vertical borehole, their sensors measure the vertical strain, horizontal strain tensor, and two components of tilt.

The removable strainmeter described by *DeWolf et al.* [2015] is intended to measure the induced deformation during carbon storage processes, however, current operations of carbon storage are limited, with most planned or actual projects associated with gas production facilities [*IPCC*, 2005]. An analog to CO_2 storage is the water injection process in the petroleum industry. Water injection, or waterflooding, has been a common secondary recovery technique for many decades [e.g., *Buckley and Leverett*, 1942; *Temizel et al.*, 2017] in oil reservoirs that are representative examples of geological formations proposed for carbon storage [e.g., *IPCC*, 2005; *Murdoch*, 2014].

The motivation of this work is to monitor an injection process by measuring multiple components of strain and tilt. The ability to characterize the subsurface deformation with this technique is currently lacking and the deformation is expected to be site-dependent. Therefore, site characteristics must be analyzed prior to field testing for an understanding of the expected deformation pattern in the vicinity of an injection well. From this analysis, locations of greatest deformation signal must be identified as these are the target areas to install monitoring wells. To test the ability of the strainmeter designed by *DeWolf et al.* [2015], a field demonstration will occur at the CO_2 analog site at the North Avant field in Osage County, OK, approximately 50 miles from Cushing, OK [*Murdoch*, 2014]. The strainmeter will be installed along with a Gladwin strainmeter [*Gladwin*, 1985] and several other instruments to provide a spatial array of the subsurface deformation. This work relies on production data and uses units that are widely accepted in the petroleum industry.

Fluid flow in reservoirs is dependent on the reservoir permeability structure [e.g., *Amy et al.*, 2013]. The reservoir at the North Avant field, the Bartlesville sandstone, is continuous across the field, yet production is known to vary locally due to lenses of coarse-grained sands of high permeability [e.g., *Dauben*, 2013]. Analysis of well logs [*Robinowitz et al.*, 2006] and facies architecture [*D. R. Kerr*, 1990; *Ye and Kerr*, 2000] suggest these sands occur as channels locally at the base of the reservoir. Fluid flow focuses within these channels and likely alters the subsurface deformation pattern; however, the dimensions of these channels are poorly constrained due to a limited number of well logs across the North Avant field. We suggest it may be possible to interpret the channel geometry using measurements of strain and tilt components during the injection process.

The objective of this work is to perform a preliminary investigation of the field characteristics of a CO_2 analog site and evaluate the strain field during an injection process. We use the analytical solution of deformation induced by pressurized inclusions as a first approximation of deformation due to pressure redistribution in reservoirs. More realistic simulations (e.g., for situations lacking an analytical solution) of the evolution of deformation during the injection process are performed numerically. A zone of greatest deformation signal that is optimal for measurements of strain and tilt components are identified as target locations of instrument installation. Potential effects of heterogeneities on the deformation pattern are also discussed. In particular, we show it is feasible to identify borders of permeability change in a heterogeneous reservoir using multiple components of the strain tensor. The interpretation can be improved by combining measurements from multiple devices in a spatial pattern or supplementary field measurements (e.g., barometric and injection pressures).

Specifically, we develop a geologic analysis of the North Avant field that is a basis for mathematical models of a planned water injection process. We idealize the reservoir based on permeability structure and show how this structure affects the deformation pattern. Two boreholes have been drilled for instrument installation at the North Avant field based on this modeling, and data collection has begun. Although models are focused on the field characteristics of the North Avant field, these models can be applied to any site of fluid injection.

2.3. Geologic analysis of the North Avant field

2.3.1. Setting

The North Avant field is located in eastern Osage County, Oklahoma (Figure 2.1a). This is on the northeast platform of the Cherokee Basin, which lies between the Ozark uplift to the east and the Nemaha ridge to the west. The field covers parts of Tiers 23N and 24N, Ranges 11E and 12E between Tulsa, OK to the south and Bartlesville, OK to the north. The region is mixed prairie rangeland with gently rolling hills covered by grasses and few trees (Figure 2.31). Sandstone crops out locally at topographic highs and within stream drainages. Injection will occur at well 9A (36°31'58N, 96°5'00W) and the deformation will be monitored in the vicinity of the well. Well 9A is at an elevation of 837 ft above mean sea level (amsl) on the northern reaches of a nearly flat field trending north to south for several thousand feet. A hill 1500 ft east is the highest point in the vicinity at an elevation of 950 ft amsl. Three retention ponds lie within 1000 ft of well 9A. The largest, approximately 14000 ft^2, is 800 ft to the northeast and another pond covering 1600 ft^2 lies approximately 150 ft to the southwest from well 9A. Tucker Creek discharges from an 8700 ft^2 retention pond 700 ft to the northwest and follows a shallow drainage basin north to south. The drainage is at least 500 ft west of well 9A, where the stream drainage is at an elevation of 790 amsl (Figure 2.31).

2.3.2. Stratigraphy

Pre-Cambrian igneous and metamorphic rocks form the basement of the North Avant field [*Bass*, 1942; *Northcutt*, 1997]. The pre-Cambrian surface in Osage County slopes westward at a depth of 2000 to 5000 ft in the southeast and northwestern part of the county, respectively [*Bass*, 1942]. The floor of the pre-Cambrian rocks have considerable relief and crystalline rock is reached at depths of 2000 to 2600 ft locally at the North Avant field [e.g., *Bass*, 1942]. Approximately 1300 ft north of the well 9A test site, a well drilled by Homa Okla Oil Co. reached the crystalline rock at a depth of 2359 ft [*Bass*, 1942].

A suite of Middle Pennsylvanian sedimentary rocks overlie the pre-Cambrian basement rocks at the North Avant field (Figure 2.1b and Appendix A.3) [*Bass*, 1942]. Density and gamma logs [*Schmeling*, 2016] suggest a series of coal, sandstone, limestone, and mudstone beds 10 ft to over 100 ft thick make up the stratigraphic column. Quaternary alluvial deposits are preserved in major stream drainages [*Hudson et al.*, 2016].

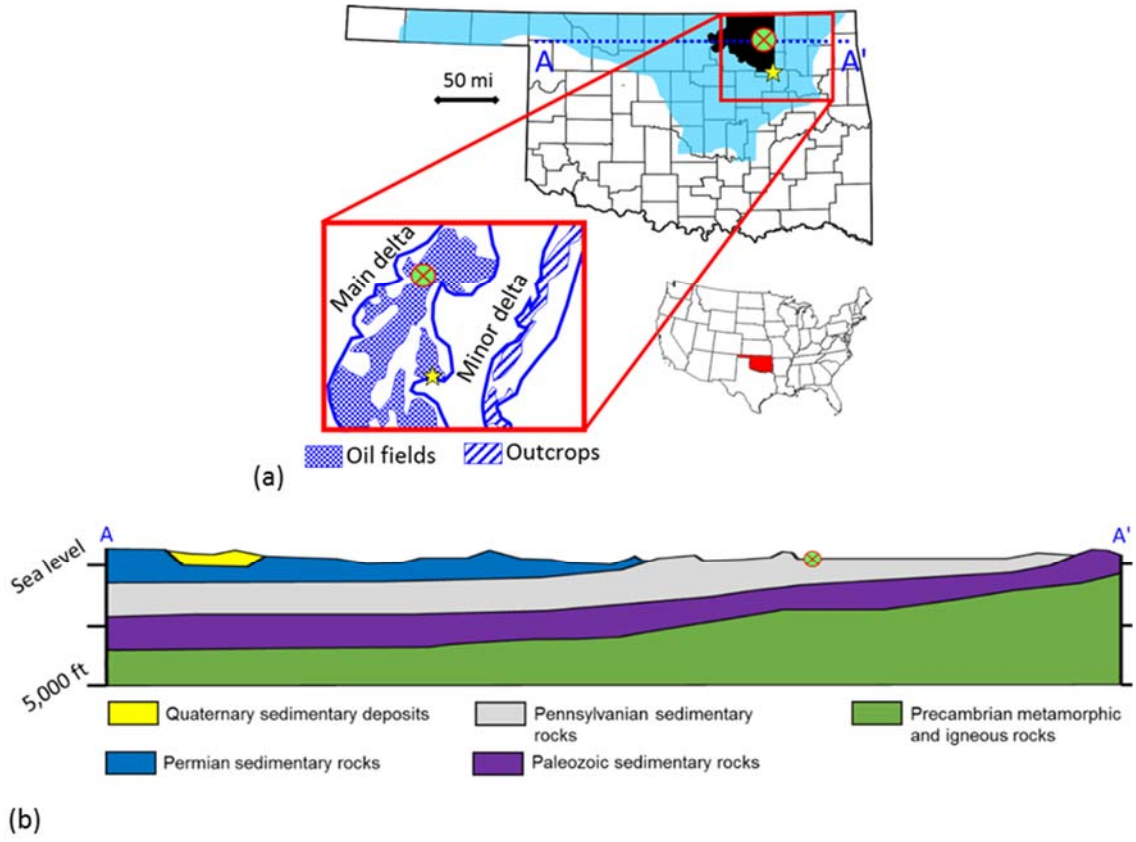

Figure 2.1. (a) Field site (green and red crosshairs) on the North Avant field. It is located within Osage County, OK (black fill) on the Cherokee Platform (light blue fill). The yellow star denotes Tulsa, OK. The inset shows the lateral range of the Bartlesville sandstone. (b) Stratigraphic cross section of $A - A'$, blue dotted line in (a).

The Bartlesville sandstone is the largest and most productive reservoir in the North Avant field. It is a member of the Boggy Formation (Table 2.1) and consists of fluvial incised valley fill deposited during a transgressional period of the lower Desmoinesian series in the Pennsylvanian period [*Ye and Yang*, 1997; *Ye and Kerr*, 2000]. Regionally, it extends north to south more than 140 mi, and the width broadens from 6 mi in the north to 60 mi in the south [*Ye and Kerr*, 2000]. It is up to 280 ft thick within regions interpreted as paleovalleys, and thins to less than 20 ft thick outside these paleovalleys [*Obianyor*, 2008]. The bedding of the formation is nearly flat, with dip angles less than 1 degree [*Hudson et al.*, 2016]. The sandstone dips to the west-southwest at a vertical to horizontal ratio of 1:125 in the southwest, which steepens to 1:200 in the north [*Northcutt*, 1997]. At the North Avant field, the ratio is 1:167, dipping to the west [*Kennedy et al.*, 1942], but the dip at the top of the Bartlesville sandstone may vary by tens to hundreds of feet

[e.g., *Robinowitz et al.*, 2006], probably because of paleotopography. The Bluejacket sandstone 40 mi to the east is the equivalent surface unit of the Bartlesville sandstone (Figure 2.2).

Within the North Avant field, the Bartlesville sandstone lies at a depth of 1200 to 1800 ft (Figure 3.1b). Gamma logs [*Schmeling*, 2016], suggests well 9A intersects the top of the Bartlesville

Table 2.1. Generalized stratigraphic column of lithologies underlying the North Avant field. Local names of formations units are abundant [e.g., *Jordan*, 1957] and we report the subsurface units as they are described by *Northcutt* [1997] and *Obianyor* [2008].

Period	Series	Group		Formation	Member	
					Subsurface name	Surface name
Pennsylvanian	Desmoinesian	Marmaton		Wewoka	Holdenville	Holdenville
					Lenapah lime	Lepanah limestone
					Wayside sand	Nowata
					Big lime	Oolagah
					Labette shale	Labette shale
					Oswego lime	Fort Scott
		Cabaniss	Cherokee	Senora	Prue sandstone	Lagorda sandstone
					Verdigris limestone	Verdigris limestone
					Skinner sand	Chelsea sandstone
					Pink lime	Tiawah
		Kerbs		Boggy	Red Fork sand	Taft sandstone
					Inola lime	Inola limestone
					Bartlesville sandstone	Bluejacket sandstone
				Savanna	Brown lime	Savanna limestone

Figure 2.2. Outcrop of the Bartlesville sandstone exposed along a roadcut 40 mi east of the field site. Natural fractures (blue arrow) result in oil seeps (black surface on rock face) [*Germanovich and Robinowitz*, 2016].

sandstone at a depth of 1620 ft, where the formation is 110 ft thick. The Bartlesville sandstone is capped by a thin mudstone layer [*Obianyor*, 2008], which is overlain by the Inola limestone and Red Fork sandstone (Table 2.1) [*Andrews and Northcutt*, 1997; *Obianyor*, 2008]. *Obianyor* [2008] studied the facies architecture to identify a layer of mudstone 5 to 13 ft thick that underlies the Bartlesville sandstone. The lower contact forms an unconformity with the Savanna formation, where there is a sharp, irregular contact in some locations, and a gradational contact in other locations [*Andrews*, 1997].The deposits between the Savanna formation and the basement rock are mostly carbonates [*Bass*, 1942].

2.3.3. Bartlesville sandstone

The Bartlesville sandstone typically consists of fine- to very fine-grained quartz sandstone, with lesser amounts of siltstone and shale [*Bass*, 1942; *Kennedy et al.*, 1942]. At the North Avant field, the formation consist of medium sand grains (1/4 mm to 1/2 mm) with 5 to 10% clay and silt [*Bass*, 1942]. Minor amounts of mudstone and carbonaceous intraclasts are locally present, particularly near the top of the formation [*Kerr*, 2007]. In general, the grains fine upwards.

Sediments of the Bartlesville sandstone were deposited in two separate depositional environments. Channel-fill, splay, and floodplain deposits typical of sediments deposited in meandering rivers overlie a series of cross-bedded sands typical of sediments deposited by anabranching channels in a braided fluvial environment [*Ye and Yang*, 1997; *Kerr*, 2007; *Obianyor*, 2008]. Hence, the upper sub-unit is called the meandering fluvial facies and the lower sub-unit is referred to as the braided fluvial facies (Figure 2.3). *Obianyor* [2008] analyzed core plugs to develop textural profiles of the bedforms. Within the meandering fluvial facies, channel-fill deposits are composed of moderately sorted, fine grained sands, splay deposits are thinly layered fine grained sands, and muds were deposited on the floodplain. The braided fluvial deposits are subangular to subrounded, moderate to well sorted, coarse to medium grained, channel-fill sandstones. Minor splay, levee, and floodplain mudstone lenses of estuarine tidal and shallow marine sediments were deposited as lateral accretion surfaces and are more prominent within the meandering fluvial deposits [*Ye and Yang*, 1997; *Kerr*, 2007; *Obianyor*, 2008].

The uppermost portion of the Bartlesville member consists of marine deposits with permeability too low for oil production. Injection and production are focused at the base of the Bartlesville sandstone [*Dauben*, 2013] in a region termed the C zone by the industry. The C zone

encompasses all of the braided subfacies and typically includes at least the lower portion of the meandering subfacies (Figure 2.3). An isopach map of the C zone at the North Avant field was developed by *Schmeling* [2016] from core data and well logs (Appendix A.4). The thickness of the C zone varies locally by tens of feet across the North Avant field. It is a minimum of 30 ft approximately 5000 ft to the northwest of well 9A, yet the thickness exceeds 100 ft in well logs elsewhere in the North Avant field.

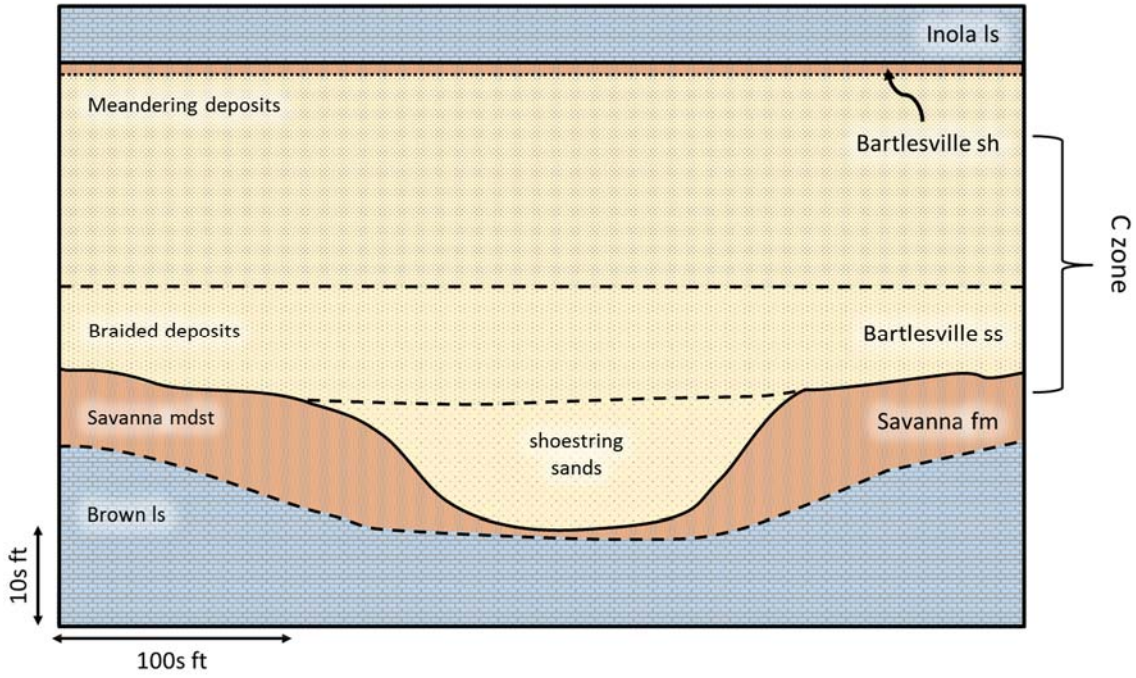

Figure 2.3. Stratigraphic cross section of the Bartlesville sandstone and confining units.

2.3.4. Deposits in high energy channels

The Bartlesville sandstone thickens locally at the expense of the Savanna formation [*Ye and Yang*, 1997], where the braided fluvial unit is underlain by channel-fill deposits of medium to coarse-grained sandstone. The channel deposits range from 3 to 18 ft thick and fine upwards [*Obianyor*, 2008]. Individual channels are separated by thin layers of shale, but may be locally bridged by fractures or sand layers. The channel-fill deposits coalesce into larger (up to 40 feet thick) elongated sand lenses that are termed high energy channels by geoscientists in the petroleum industry because they are composed of coarse-grained sands representative of a high-energy depositional environment [e.g., *Robinowitz et al.*, 2006]. The high energy channels are

typically included in the C zone, although we distinguish between these regions to more accurately characterize the reservoir.

Regionally, the high energy channel deposits are referred to as “shoestring” sands [*Bass*, 1934] because of their elongate and sinuous form. There are conflicting interpretations on the origin of these fluvial deposits. *Bass* [1936] performed a regional study on these sands and determined they were likely deposited as offshore bars of a broad embayment on the western margin of an ancient inland seaway during the Pennsylvanian period. Irregular patches of deposits are the result of sands reworked by shoreline processes. It is possible that the sands locally underwent erosional processes, further truncating the sand deposits; however, *Bass* [1936] did not observe any erosional features at a site approximately 100 mi north of the North Avant field. *Rees* [1972] later suggested the sands were deposited by distributaries in a fluvial environment. In this case, the irregular patches of shoestring sands are the result of deposits on point bars. The shoestring sands were later buried by the brained and meandering fluvial deposits.

At the North Avant field, nine channels trending southwest to northeast have been identified within six square miles of well 9A (Appendix A.4, *Schmeling*, 2016]). The semi-elliptical channels pinch out laterally where the Savanna shale directly underlies the C zone (Figure 2.7b). The channels are up to 50 ft thick, 5000 ft wide and 15000 ft long. Ratios of length to width vary significantly, but are approximately 4:1. The thickness of the channels decreases gradually, with the decrease in thickness not exceeding 1.5 ft per 100 ft of horizontal distance. The largest channel lies 11000 ft to the southeast of well 9A, with a length that extends for over 8000 ft along a northeast axis with a maximum width exceeding 3000 ft. Well logs suggest a high energy channel 35 ft thick is intersected at well 9A. This channel is approximately 2000 ft wide and 7920 ft long and nearly centered below well 9A(Figure 2.7b).

Borehole data has been used to constrain the dimensions of most of the channels at the North Avant field, however this data is limited. The dimensions of the high energy channels are often poorly constrained, as only a few well logs exist in the vicinity of the channels. For example, the dimensions of the high energy channel intersected by well 9A are interpolated from fewer than 15 well logs. This logs are concentrated at or to the south of well 9A, and there are limited data to the north. Specifically, there is no data near the predicted channel border to the northeast. Therefore, it is possible the channel may truncate or expand considerably past this boundary.

2.3.5. Historical oil production

The North Avant field was discovered in 1904 [*Franks*, 1989] and has undergone over 100 years of oil recovery [*Andrews*, 1997]. Cumulative production from 1906 to 2001 exceeded 14,000,000 barrels of oil [*Obianyor*, 2008]. Primary recovery methods, including gas re-injection, were used exclusively from 1905 until 1984, when secondary techniques were introduced. Traditional water injection operations proved to be inefficient due to the heterogeneous nature of the field. This is why horizontal well technology was implemented in 2004 [*Dauben*, 2013] by Grand Resources Inc., who currently control the mineral rights. Twelve wells, including four horizontal wells, are completed within 1000 ft of well 9A. Four of these wells have produced oil since 2010. Production data is limited for these wells, however, the horizontal wells (wells 22 and 32 in Figure 2.31) had an initial production of approximately 450 barrels on the first day of production. Many more wells are in the vicinity of well 9A (Figure 2.31), but have been inactive for many decades. All wells in the vicinity of well 9A have been inactive since at least January 2016.

Well 9A was drilled in the early 1990s with the intention of using it for oil production; however, it produced a meager rate of oil during initial testing. Hence, it was configured to be used as a water injection well to improve oil production from the horizontal wells in the vicinity and has operated as such since at least 2004. Water was injected at a rate between 900 and 1000 barrels per day in 2011. The initial surface pressure was less than 10 psi, which increased to 100 psi over the first few months (Figure 2.4). During the majority of 2012, fluids were injected between 800 and 1000 barrels per day. This corresponded to pressures between 100 and 200 psi. The well was shut-in for the majority of 2013. Sustained injection began again in 2014, until it was last shut-in in October 2015. The last year of injection at a rate of 400 to 700 barrels per day resulted in a surface pressure of 60 to 100 psi.

Bottomhole pressure (wellhead pressure plus hydrostatic pressure) in the vicinity of well 9A has varied significantly due to injection and pumping. At well W2, 650 ft to the SW of well 9A Injection at a rate of approximately 900 barrels per day occurred between January 2011 and February 2013, corresponding with a wellhead pressure of 100 psi (Figure 2.4). After periodic shut-ins, the sustained injection from August 2014 to October 2015 at 500 to 600 barrels per day resulted in a wellhead pressure of approximately 90 psi. The max wellhead pressure recorded (200 psi) at well 9A was achieved when injection rates approached 1000 barrels per day. Prior to October 2010, the water level in well 9A was 420 to 620 ft above the top of the reservoir,

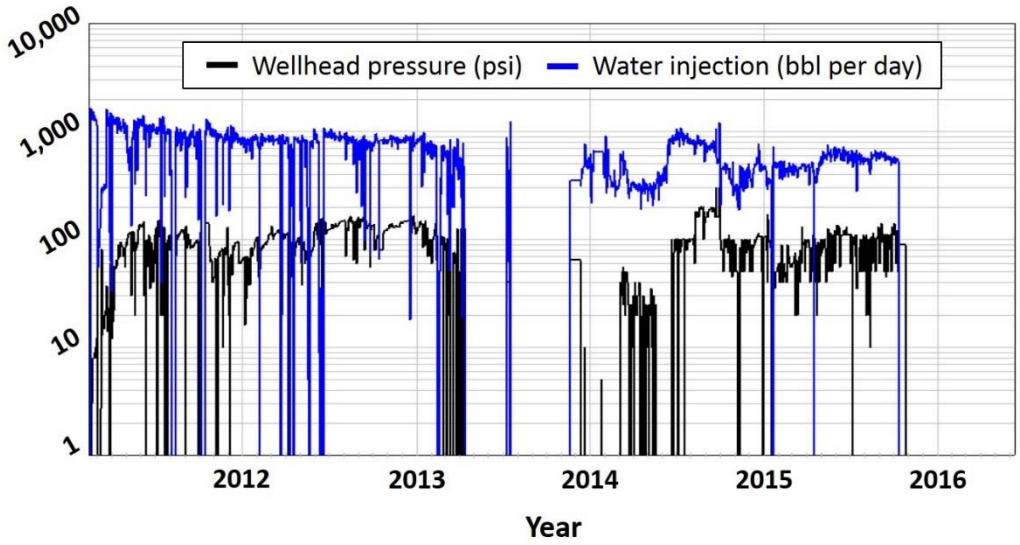

Figure 2.4. Historical record of controlled injection rate and the corresponding wellhead pressure [*Schmeling*, 2016]. Injection in well 9A has occurred nearly continuously from January 2011 to October 2015. Waterflooding occurred at a rate of several 100s of barrels per day and the corresponding wellhead pressure was monitored during this time.

corresponding to a bottomhole pressure of 140 to 270 psi. In August 2016, the water level rose to 1170 ft with a corresponding reservoir pressure of 500 psi.

Two step rate tests were performed by *Robinowitz et al.* [2006] at the Wolco field, approximately 1 mi east of the North Avant field. Records of the injection rate and pressure were measured using a downhole sensor. Prior to the test, reservoir pressure was 125 psi and injection at 2000 barrels of water per day did not register a positive surface pressure at well Wolco 4A during production. The step rate test suggested the bottomhole fracture opening pressure of 573 psi corresponded to an injection rate of 1745 barrels of water per day for a fracture-parting pressure gradient of approximately 0.34 psi/ft. Well logs suggest the Wolco 4A well does not intersect a high energy channel, and another step rate test was performed at Blake 1A, a nearby well intersecting a high energy channel roughly 20 ft thick. At this well, fluids were injected at a rate up to 3000 barrels of water per day. The maximum rate corresponded to a bottom hole pressure of approximately 650 psi, but the surface pressure did not exceed zero and it was determined the fracture parting pressure was not reached [*Robinowitz et al.*, 2006]. This suggests injection at well 9A, which also intersects the high energy channel, can occur at bottomhole pressures exceeding 600 psi without initiating fracturing opening.

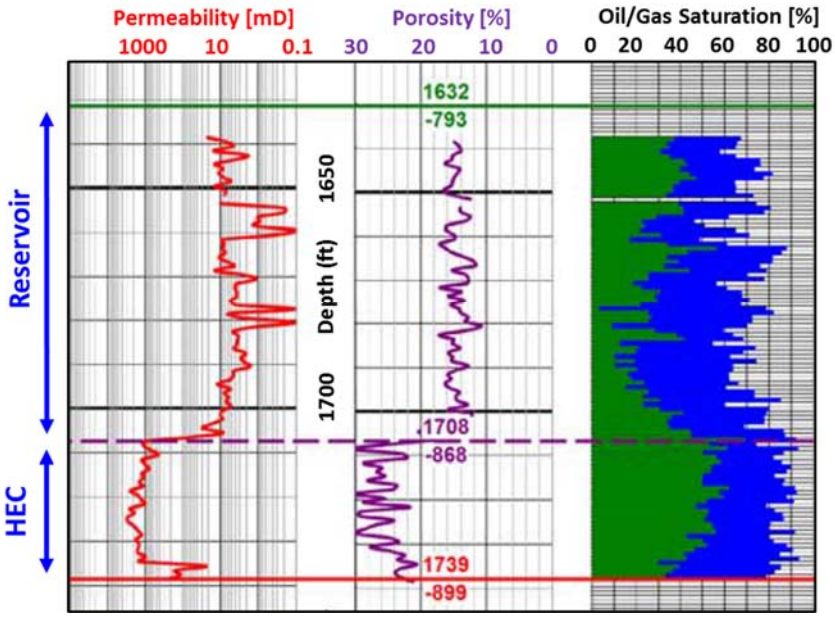

Figure 2.5. Permeability, porosity, and saturation logs of the Bartlesville sandstone at well W2, 650 ft to the southwest of well 9A [*Schmeling*, 2016]. The reservoir grades into shales at a depth of 1632 ft (solid green horizontal line, -793 ft subsea value). The base of the reservoir is at a depth 1739 ft (solid red line, -899 ft subsea value). The reservoir is 50 to 90% saturated with oil (green bars) and water (blue bars). The high energy channel (HEC) has significantly greater permeability, porosity, and oil saturation. The log of oil saturation is consistent with the 45% measured with a resistivity log at well Blake 3A on the Wolco field by *Robinowitz et al.* [2006].

2.3.6. Reservoir properties

The properties of the Bartlesville sandstone are known from laboratory measurements on cores [*Kerr*, 2007; *Obianyor*, 2008], well logs [*Robinowitz et al.*, 2006; Schmeling, 2016], and from analyses of well performance [*Robinowitz et al.*, 2006; *Dauben*, 2013]. In the gamma log of well Solar LaBodie 12-AI, located in the southwest quadrant of sec 19 T24N R12E and approximately 1 mi east of well 9A, meandering fluvial deposits have an average GR API unit of 42.9 and the braided fluvial deposits have an average GR API unit of 38.78 [*Obianyor*, 2008]. The higher value in meandering fluvial deposits suggests it has a higher shale content. This corresponds to the architectural description of *Obianyor* [2008] and suggests it is also likely to have a lower permeability.

Pressure decay profile permeameter measurements were performed on small cores by *Obianyor* [2008]. Eight cores were cut from the meandering fluvial deposits at well Solar LaBobdie 12-AI and seven other wells in the vicinity. An additional six cores from the braided fluvial deposits exposed at an outcrop 35 mi to the southeast of the North Avant field were also utilized in the

analysis. The cores were studied foot by foot for the length of the Bartlesville sandstone. Measurements were oriented parallel to strike, parallel to dip, and perpendicular to sedimentary surfaces. These data show porosity and permeability increase with depth in the Bartlesville member (Table 2.2). In general, porosity and permeability are more variable in the upper meandering fluvial facies [*Obianyor*, 2008]. Core permeability ranges from 0.01 to 129.8 mD, with a geometric mean of 7.6 mD in the meandering fluvial facies, and it ranges from 0.1 to 432 mD with a geometric mean of 35 mD in the underlying braided fluvial unit [*Obianyor*, 2008]. The porosity follows a similar trend; the measurements by *Obianyor* [2008] ranged between 0.10 and 0.20 with an average of 0.16 in meandering fluvial deposits and increases to between 0.15 and 0.23 with an average of 0.18 in the braided fluvial facies.

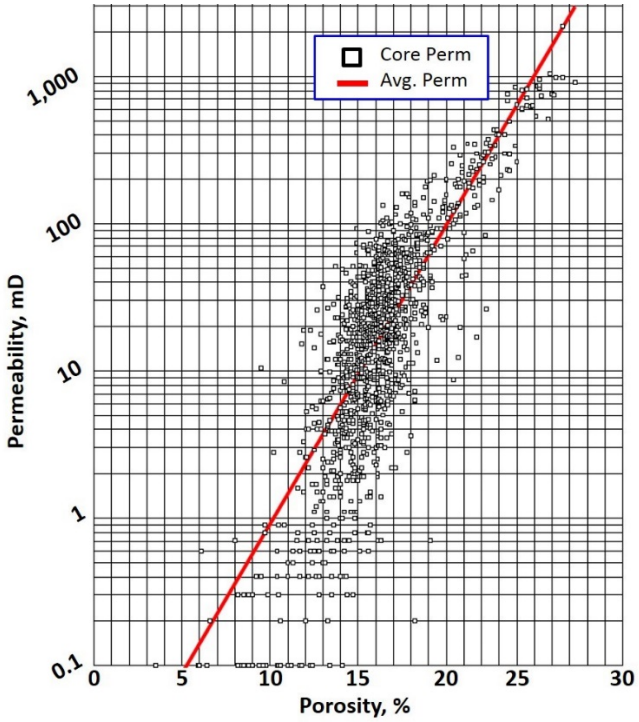

Figure 2.6. The permeability and corresponding porosity of cores from the Wolco area, 2500 ft from well 9A performed with gas probe permeameter [Figure 5 of *Dauben*, 2013]. *Dauben* [2013] used the correlation $\log k = 0.1402\phi - 0.7658$ (red line) for simulations of well performance. This relationship matches well for porosities greater than 15% (permeabilities exceeding several millidarcies), but tends to overestimate the permeability by tenths of millidarcies for porosities below 15%. Nevertheless, this error is exaggerated by the log normal distribution.

The measurements on the cores by *Obianyor* [2008] are generally consistent with other core and field measurements At well Blake 3A, 1 mi east of well 9A, measurements by *Robinowitz et al.* [2006] of the density log and permeability to air cores suggests an average porosity ϕ = 0.18 and permeability k = 30 mD (Figure 2.6). The well logs of gas probe permeameter and neuron porosity provided by *Schmeling* [2016] of well W2, 650 ft southwest of well 9A that suggest the C zone has a permeability of 1 to 10 mD and porosity of 0.11 to 0.19 (Figure 2.5). Values increase in the high energy channel intersected at well W2 such that permeability is approximately 1000 mD and porosity ranges between 0.22 and 0.30. The increase in porosity is considerably less than the increase in permeability. This suggests a significant influence of grain size on the relationship between porosity and permeability [e.g. *Tiab and Donaldson*, 1996]. The permeability in the high energy channel is roughly double the maximum permeability measured on the cores taken from the outcrop of braided fluvial deposits. This likely suggests the core samples of the outcrop either lack high energy channel deposits, or there is significant spatial variation in the permeability of the high energy channels. Excluding measurements within the high energy channel at well W2, permeability measurements are generally consistent independent of the measurement methodology. This suggests joints that are evident on the surface equivalent of the Bartlesville (Figure 2.2, see also *Carroll and Guo*, [1999]) likely do not contribute much to the permeability structure of the reservoir.

Inferences on the permeability at the reservoir scale may be drawn from the data of injection rate and corresponding wellhead pressure at well 9A (Figure 2.4). We identify two periods of approximately constant injection rates that result in near linear increases in the wellhead pressure. In January and February 2012, injection was maintained at approximately 880 barrels per day over the course of 30 days. During this time, the wellhead pressure increased from 80 to 115 psi. Using the built-in SNOPT optimization method within Comsol, we neglect the change in pressure along the borehole and match wellhead pressure with the injection rate to determine an average reservoir permeability k = 180 psi. At another time of relatively constant injection during October and November 2012, the average injection rate was approximately 850 barrels per day. During this time, the wellhead pressure increased from 110 psi to 150 psi. This results in an average reservoir permeability k = 155 psi. These calculated permeabilities are within the range of values measured on core samples. Further, our calculated values are one order of magnitude greater than the values typical of the C zone and one order of magnitude less than the log of

values of the high energy channel intersected by well 9A, suggesting well 9A intersects a high energy channel at the base of the reservoir.

Mud drapes act as vertical permeability baffles throughout the formation. The vertical to horizontal permeability ratio (k_v/k_h) is less than 1, and is generally higher in the braided fluvial deposits (0.07 to 0.77) than the meandering fluvial deposits (0.03 to 0.38) [*Obianyor*, 2008]. In production simulations by *Dauben* [2013], the average $k_v/k_h = 0.25$ was used to match production data.

Table 2.2. Statistical analysis of permeability measurements taken with a probe permeameter on cores of the Bartlesville member in the southwest quadrant of section 19, T24N R12E and adjacent areas [*Kerr*, 2007; *Obianyor*, 2008].

	Porosity, ϕ		Horizontal permeability, k_h (mD)			
Unit	range	avg.	range	avg.	geometric mean	k_v/k_h
Braided deposits	0.15 – 0.23	0.18	0.1 - 430	75	35	0.07 – 0.77
Meandering deposits	0.10 – 0.15		0.01 - 130	25	8	0.03 – 0.38
Shale lenses	0.05 – 0.15		0.01 - 15			

Density varies with lithology within the Bartlesville member. Density logs were analyzed by *Obianyor* [2008] from measurements taken at three foot intervals on three cores at the North Avant field. He measured the thin coal beds to have a density of approximately 1.15 g/cm^3, while claystones and mudstones have densities of 3.1 and 2.8 g/cm^3, respectively. The average densities measured by [*Obianyor*, 2008] on cores at well Solar LaBodie 12-AI are 2.39 g/cm^3 and 2.36 g/cm^3 for the meandering fluvial and braided fluvial deposits, respectively. Hence, the braided fluvial deposits have only a slightly lower density than the meandering fluvial deposits.

Several one-inch cores of the Bartlesville sandstone were drilled by Shell at wells approximately 1 mi east of well 9A in the early 2000s. Two of those samples were then tested under uniaxial compression at Georgia Tech, where *Germanovich* [2017] measured a Young's Modulus of approximately 20 GPa. To the best of our knowledge, other mechanical tests have not been conducted on samples from the North Avant field, and properties were inferred from the database compiled by *Murdoch et al.* [2016]. The data were compiled from testing on rocks collected around the world and we focused on formations with similar environments of deposition and burial history for this study. For example, *Tamimi and Davis* [2012] recorded well

logs of gamma ray, compressional wave velocity, and shear wave velocity on the Morrow A formation at the Postle Field, Texas County, Oklahoma (300 miles west of the North Avant field). Sediments were deposited as multi-stacked lenticular bodies within paleovallies during the Upper Morrow series of the Pennsylvanian age. The sandstone and mudstone were logged at depths of approximately 6200 and 6100 ft, respectively, and the results are presented in Table 3, along with calculated elastic properties. The Young's Modulus of the sandstone is greater than the measurements made by *Germanovich* [2017] on the Bartlesville sandstone. One possible explanation of this is the sediments currently lie at depths exceeding 6000 ft, which is more than three times the depth of the Bartlesville member at North Avant field. Measurements taken on similar formations reported in the literature yield a range of values similar to these measurements [e.g., *Rice and Cleary*, 1976; *Palciauskas and Domenico*, 1989; *Peng and Zhang*, 2007].

Table 2.3. Wave velocities and calculated elastic properties of the Morrow A sandstone from measurements by *Tamimi and Davis* [2012] at the Postle field, Texas County, OK.

	ρ [g/cm^3]	V_p [m/s]	V_s [m/s]	E [GPa]	ν
Morrow sandstone	2.44	3875	3335	31.3	0.23
Morrow shale	2.57	2279	1518	16.2	0.37

2.3.7. Conceptual model

Production data suggests it is useful to categorize the reservoir based on the permeability structure. The coarse sands of the high energy channels result in high permeabilities, and the petroleum industry generally considers permeabilities greater than 100 mD as an indicator of these channels [*Schmeling*, 2016]. In the vicinity of well 9A, the permeability of the high energy channels exceeds this value. The C zone typically has a permeability of 10 mD and porosity of 0.2 (section 2.3.5). There is a jump in permeability and porosity at the boundary of the C zone and high energy channel. Within the high energy channel, the permeability increases to values that exceed 1000 mD and porosity is between 0.20 and 0.25 (Figure 2.5). The reservoir is confined within two shale units with lower porosity (approximately 0.15) and significantly lower permeability ($\lesssim$ 0.1 mD).

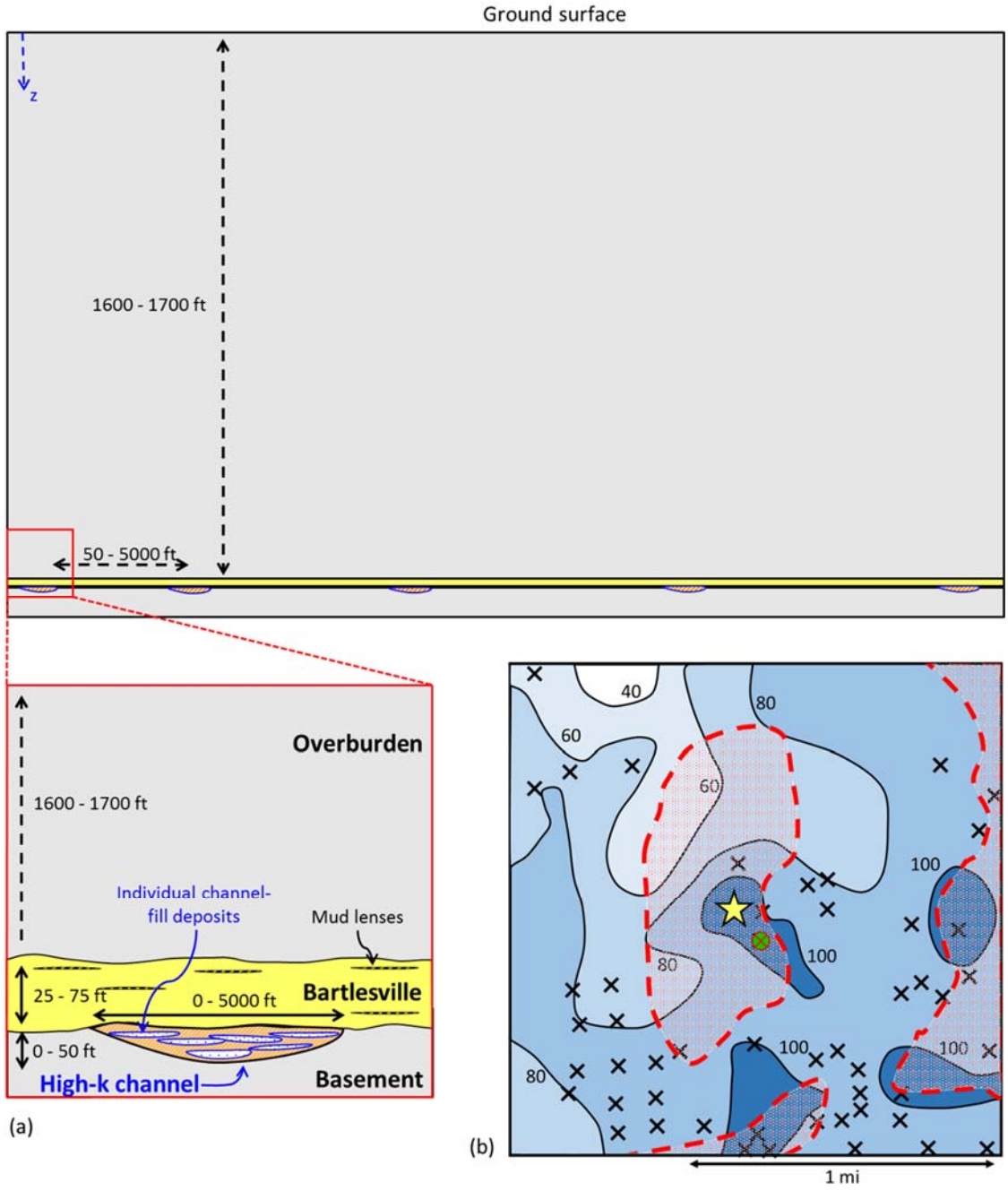

Figure 2.7. (a) Conceptual model of the Bartlesville reservoir. Production is focused in lower section (C zone) of the member. High energy channels with high permeability are dispersed locally below the C zone and consist of a connected series of individual channel deposits. (b) Isopach map of the reservoir (C zone plus high energy channel) in the vicinity of well 9A (yellow star). Approximate boundaries of the high energy channels are marked by red dashed areas. The red cross on the green circle is the location of well W2 used for the logs in Figure 2.5. Black crosses are locations of wells used in contouring. Contours are in feet.

A conceptual model of the reservoir at the North Avant field is composed of a homogeneous, anisotropic reservoir that overlies regions of high permeability at its base. The high energy channels are only present locally, and the spacing between channels varies between 50 to 5000 ft (Figure 2.7). The overlying strata consists of sandstone, mudstone, and limestone, however, data on the properties of the stratigraphic column are currently lacking. Hence, we view these units as an extension of the confining units in models described in later sections.

Sedimentary units are interbedded throughout the stratigraphic column with the thickness of beds at least one order of magnitude, and typically two orders of magnitude, less than the total thickness of the overburden. As an approximation for modeling in the following sections, we assume uniform geomechanical properties and focus on the effect of permeability structure on reservoir pressure distribution and the resulting deformation pattern. We assign a uniform density of 2.5 g/cm^3 in the models. This value is representative of the lithologies present in the stratigraphic column (section 2.3.5 and Appendix A.5); mudstones have densities that may exceed 3 g/cm^3, the density of the sandstone is approximately 2.4 g/cm^3 [*Obianyor*, 2008], and limestones are expected to have densities within this range. Currently, elastic properties of the strata at the North Avant field are limited to the single uniaxial compression test by *Germanovich* [2017]. The measured Young's Modulus was 15 GPa, which we assign for all domains and discuss the implications of varying stiffness in section 2.7.1. The poison ratio of 0.23 and 0.37 (Table 2.3) for the Morrow sandstone and shale, respectively, calculated from the data of *Tamimi and Davis* [2012] is typical for similar formations [e.g. *Detournay and Cheng,* 1993; *Murdoch et. al*, 2016], and we assign v = 0.23.

Using a negative compression sign convention, the principle of effective stress is written as

$$\sigma'_{ij} = \sigma_{ij} + \alpha p \delta_{ij} \tag{2.1}$$

where, σ'_{ij} and σ_{ij} are the effective and total stress, respectively, p is the pore pressure, and δ_{ij} is the Kronecker delta. The Biot Willis coefficient α [*Biot,* 1941, 1955; *Biot and Willis*, 1957] includes the effect of grain compressibility. Specifically, α is the ratio of the fluid volume lost within an element to the volume change of the element during compression at constant stress (when pore pressure is allowed to return to the initial state). Hence, $0 \leq \alpha \leq 1$. For highly compressible skeletons, i.e. soils, the compressibility of the grains is negligible, and α = 1. For rock, α may be considerably less. P*alciauskas and Domenico* [1989] state typical Biot-Willis coefficients of 0.95, 0.76, and 0.69 for mudstones, sandstones, and limestones, respectively. The database of *Detournay and Cheng* [1993] reports a range of α for sandstones between 0.65 to

0.85, for an average α = 0.75. We assign a Biot-Willis coefficient α = 0.75 as an intermediate value. This is a typical value for sandstone formations and is approximately the average expected for the layered strata.

The conceptual model of the North Avant field is the physical basis for our models of the injection process (Figure 2.7a). We investigate this model in the following sections progressing from the simplest analytical models to more accurate numerical models.

2.4. Reservoirs as pressurized inclusions

Reservoirs undergoing fluid injection have been modeled as poroelastic inclusions in undrained elastic host rock [e.g., *Segall and Fitzgerald*, 1998; *Suckale*, 2009] for various shapes (such as elliptical), and homogeneous pressure distributions [e.g., *Mura*, 1982; *Berryman*, 1995; *Germanovich and Chanpura*, 2002; *Guido et al.*, 2015]. Numerical methods are often used if the reservoir shape is not elliptical, the pore pressure distribution is not uniform, or the space is not infinite [e.g., *Rutqvist et al.*, 2008; *Chen*, 2011]. Nevertheless, a number of analytical techniques are available to obtain closed form solutions of simplified problems with subsequent fast computation times. The first-order simplification is to treat the embedded inclusion as a region undergoing transformation strain (also called eigen strain [e.g., *Mura*, 1982; *Chen*, 2011]) such as poroelastic [e.g., *Geertsma*, 1966; *Segall et al.*, 1994] or thermoelastic [e.g., *Davies*, 2003] strains. For example, *Germanovich et al.* [2012] treated the volumetric expansion of a peridotite body undergoing serpentinization as a transformation strain. They developed a model of the crustal stress and deformation induced by the serpentinization, and applied it to topographic features and seismicity at the TAG hydrothermal field (Mid-Atlantic ridge, 26°N) and Miyazaki Plain (Kyushu-Palau subduction zone, SW Japan). In this work, we use the analytical relationships of *Germanovich et al.* [2012] to derive the strains induced by volumetric expansion of pressurized inclusions and to evaluate the resulting deformation. Solutions are numerically plotted using Mathcad [*PTC*, 2007].

2.4.1. Pressurized 2-D inclusion

To highlight the effects of injection on the deformation processes, *Germanovich et al.* [2012] consider the simplest case of a 2-D elliptical inclusion undergoing homogeneous transformation strain, ε_0, in an elastic half-space $y < 0$ (Figure 2.8a). Pressurized inclusions can be viewed as subsurface regions with poroelastic deformations resulting from transformation strain. This is equivalent to the strain generated in a corresponding unconstrained inclusion when removed from the host material.

In general, the displacement field can be represented as [*Muskhelishvili*, 1977]

$$2\mu\left(u_x + iu_y\right) = \kappa\varphi(z) - z\overline{\varphi'(z)} - \overline{\psi(z)} \tag{2.2}$$

where u_x and u_y are the displacements in x (vertical) and y (horizontal) directions, $z = x + iy$, $i^2 = -1$, bars represents complex conjugates, $\kappa = 3 - 4\nu$ for plain strain conditions, $\mu = E/[2(1+\nu)]$ is the shear modulus, and $\varphi(z)$ and $\psi(z)$ are the *Muskhelishvili* [1977] stress functions. Parameters

$$\begin{gathered}\varepsilon_{xx} = \partial u_x/\partial x,\ \varepsilon_{yy} = \partial u_y/\partial y,\ \varepsilon_{xy} = (\partial u_x/\partial y + \partial u_y/\partial x)/2,\\ \omega_{xy} = \partial u_x/\partial y,\ \omega_{yx} = \partial u_y/\partial x\end{gathered} \tag{2.3}$$

are the strains and tilts. , and $\varepsilon_0 = 0$ outside the inclusion. To perform deformation analysis, we first note that, as we are interested in monitoring deformations in shallow boreholes, we only need to consider the region outside the inclusion. In the case of ε_0 homogeneous inside the inclusion, in this region [*Ru*, 1999; *Ru et al.*, 2001; *Germanovich et al*., 2012],

$$\varphi(z) = A\left[\overline{D(\bar{z})} - \overline{P(\bar{z})}\right],\quad \psi(z) = -A\left[z\overline{D'(\bar{z})} - z\overline{P'(\bar{z})} + D(z) - P(z)\right] \tag{2.4}$$

where

$$D(z) = \overline{\omega\left[1/\overline{\omega^{-1}(z)}\right]},\quad A = (4/3)\mu(1+\nu)\varepsilon_0/(\kappa+1) \tag{2.5}$$

and $z = \omega(\zeta)$ is conformal mapping of the region outside the inclusion in the infinite complex plane $z = x + iy$ onto the exterior of the unit circle, $|\zeta| = 1$, on the infinite complex plane $\zeta = \xi + i\eta$, $\omega^{-1}(z)$ is the inverse function of $\omega(\zeta)$. The polynomial of finite degree, $P(z)$, in (2.4) is defined by the asymptotic behavior of $D(z)$ at infinity, that is, by representing $D(z)$ as $D(z) = P(z) + o(1)$ $(z \to \infty)$. Note that while (2.4) is valid outside the inclusion, ε_0 in (2.5) is the transformation strain inside the inclusion. In other words, that $\varepsilon_0 = 0$ outside the inclusion in (2.2) and (2.3) does not mean that the deformation field in this region is independent of the transformation strain.

Choosing

$$\omega(\zeta) = \lambda\zeta + z_0 + \sum_{k=1}^{N} \frac{c_k}{\zeta^k} \tag{2.6}$$

allows for the analysis of many practically-important inclusion shapes [e.g., *Muskhelishvili*, 1977]. In the case of an inclined elliptical inclusion [*Germanovich et al.* 2012], $N = 1, \lambda = e^{i\beta}\,(a+b)/2$, $c_1 = e^{i\beta}\,(a-b)/2$,

$$\omega^{-1}(z) = \frac{e^{-i\beta}(z - z_0)}{a+b}\left[1 + \sqrt{1 - \frac{e^{2i\beta}(a^2 - b^2)}{(z - z_0)^2}}\right] \tag{2.7}$$

and

$$D(z) = \frac{\bar{\lambda}}{\omega^{-1}(z)} + \bar{z_0} + \bar{c_1}\omega^{-1}(z), \quad P(z) = \bar{z_0} + \frac{\bar{c_1}}{\lambda}(z - z_0) \tag{2.8}$$

For the inclusion shown in Figure 2.8a, it is convenient to choose $z_0 = -ih$ with *h* being the depth of the inclusion center.

In a reservoir, regions of greater permeability, such as the high energy channels, are expected to undergo more rapid pressurization. As a first estimate of the pressure distribution during long-term injection into a long channel, we calculate the deformation of a flat-lying ellipse ($\beta = 0$) under plane strain conditions. Using equations (2.2) through (2.8), we compute the strains and tilts induced by inclusions of major axis a_i = 500, 1500, and 3000 ft. The ellipse is centered at a depth of *h* = 1500 ft and the minor axis of the ellipse, *b* = 25 ft, is maintained for all a_i(Figure 2.8b). Elastic properties (Young's Modulus *E* = 15 GPa, Poisson's ratio *v* = 0.23, and Biot-Willis coefficient α = 0.75) are uniform throughout the model. Hereafter, με = 10^{-6} (microstrain), μrad = 10^{-6} (microradians), and nε = 10^{-9} (nanostrain).

2.4.2. Deformation induced by pressurized elliptical region

The high energy channels underlying the C zone at the North Avant field are typically elongated in one direction (section 2.3.3). Injection into these channels may result in pressurized regions resembling this plane strain solution. This analysis shows the principle of monitoring pressure redistribution in inclusions (i.e., reservoirs) with measurements of deformation in shallow boreholes. In particular, it is possible to judge the size of a pressurized region from these measurements.

Figure 2.9 shows how the deformation changes at the shallow depth of 150 ft as inclusion width changes. The maximum of the normal strains is always centered over the origin and increases as a approaches h. After a exceeds h, the magnitude of the normal strains decrease slightly. This trend corresponds to an increasing lateral region of normal strains as a increases. The horizontal strain ε_x is approximately triple the value of the vertical strain ε_y. Horizontal strain is generally tensile over the pressurized region and becomes negative for $|x| > a$. In contrast, ε_y is compressive over the inclusion and tensile for $|x| > a$. There is a local maximum of signal overlying the inclusion boundary. The x location of this local minimum (and strain sign change) moves laterally outward at a faster rate than the increase in a.

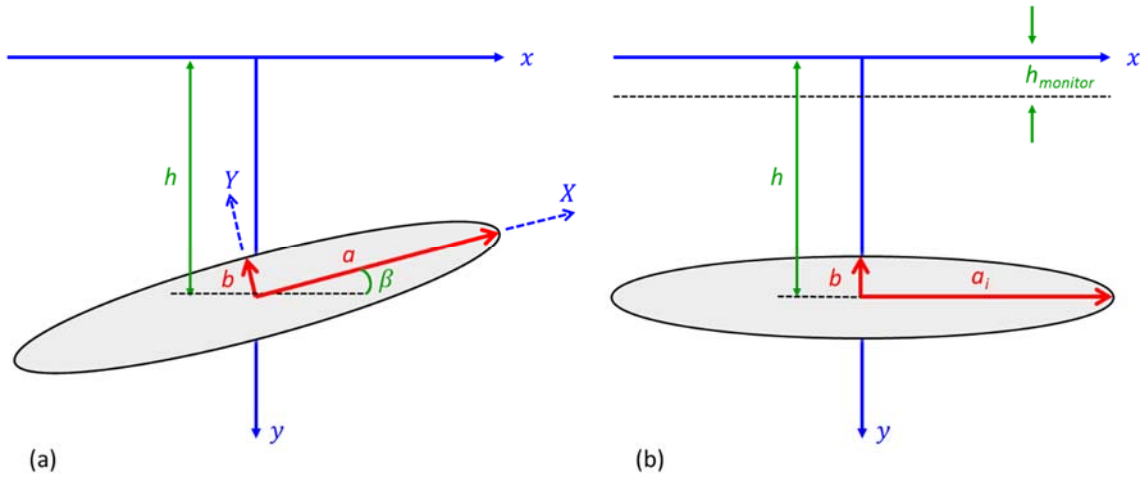

Figure 2.8. (a) Model of elliptical subsurface inclusion located in the half-space $y \leq 0$, $-\infty < x < \infty$ and the major ellipse axis is aligned with coordinate axis, *X*, in rotated coordinate set (*X*, *Y*). (b) Geometry of the inclusion used to calculate the deformation in Figure 2.9. The major axis is a_i, where *i* denotes the variations of the channel width.

The shear strain increases as a approached h. Similar to the normal strains, shear strain decreases as a exceeds h. The x coordinate of maximum ε_{xy} (on the order of 0.01 $\mu\varepsilon$) closely corresponds to $|x| = a$. For small a, the maximum ε_{xy} is in front of the pressurized inclusion, but moves to $x < a$ as a increases. Nevertheless, this change is gradual and allows for an approximation of the pressurized width, a. Shear strains are approximately one order of magnitude less than normal strains.

Tilt is away from the origin in the shallow subsurface. The maximum is on the order of 0.1 μrad for the defined conditions. When $a < h$, the x coordinate of the maximum tilt is less than a. As a increases, the location of maximum ω_{xy} moves outward such that it passes a when $a > h$. In contrast to the normal strains, ω_{xy} continues to increase as a exceeds h. Nevertheless, for $a \gg h$, the magnitude of tilt also decreases.

Deformation scales with model dimensions. If the ratios between a, b, h, and $h_{monitor}$ are constant, then the deformation does not change along $h_{monitor}/h$. Increasing b while the other geometric parameters are constant, results in matching deformation patterns, however, the magnitude of deformation increases in an amount proportional to the increase in b (Figure 2.10).

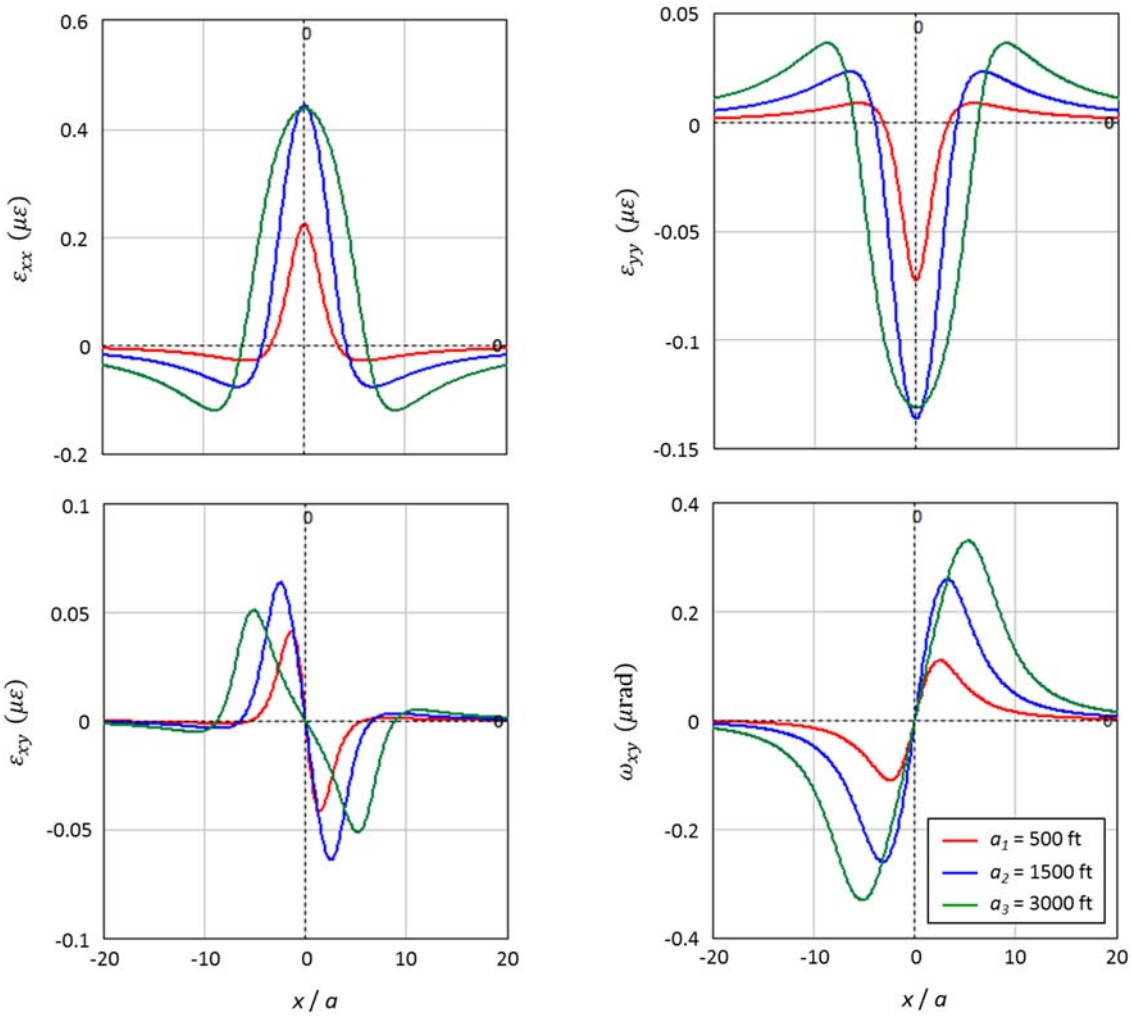

Figure 2.9. Strains and tilt occurring at the shallow depth of 150 ft due to the pressurization of an elliptical inclusion with increasing major axis, a, at a depth h = 1500 ft .

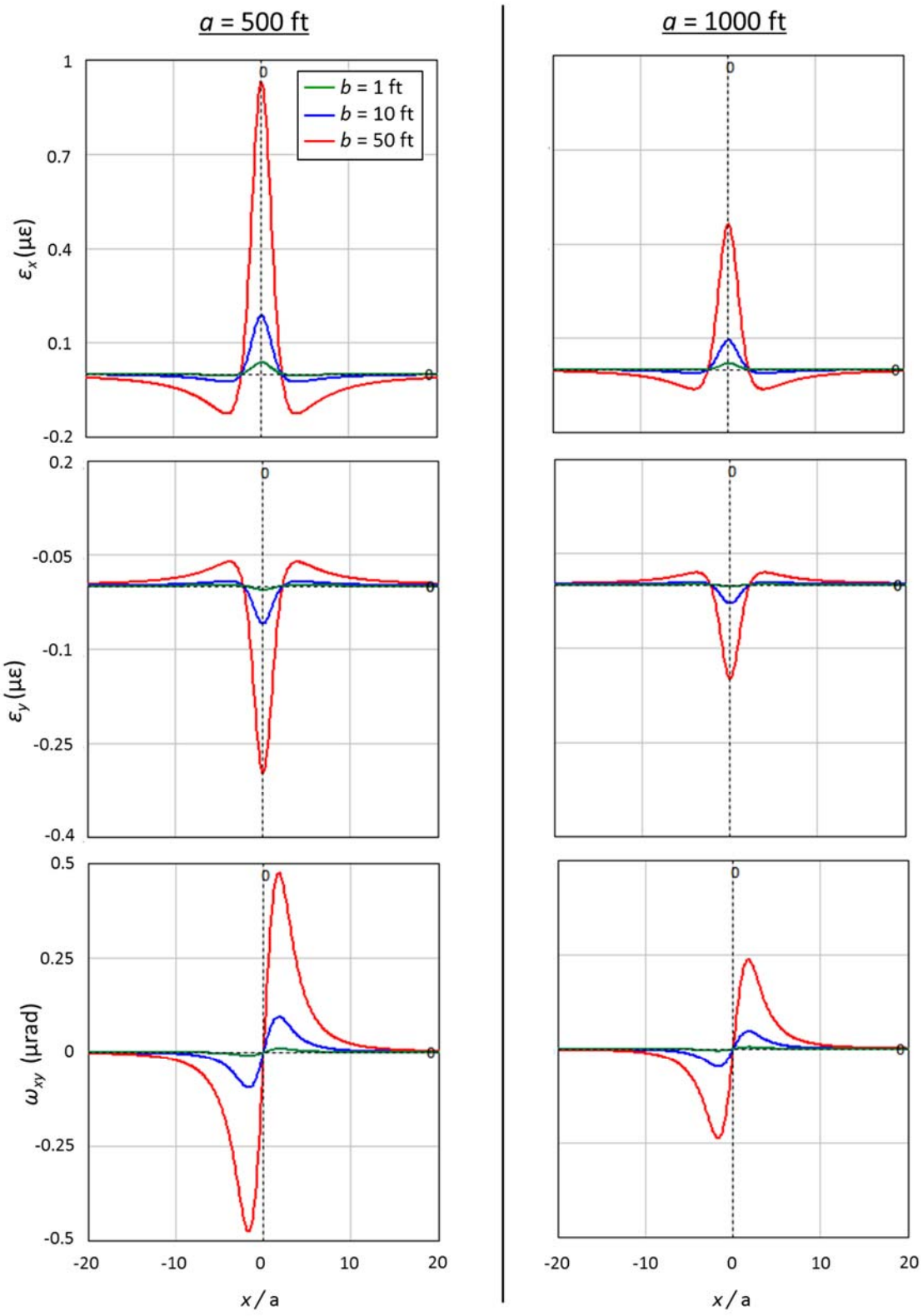

Figure 2.10. Plots of normal strains and tilt at a monitoring depth $h_{monitor}/h$ = 0.1. The ratio h/a = 2 is maintained for the changing ellipse size and the minor axis b varies from 1, 10, and 50 ft.

For the parameters chosen in Figure 2.10, normal strain reversal occurs at an approximate lateral distance $x = 2.5a$ and tilt reversal occurs at $x = 1.75a$. The lateral distance of the strain reversal gradually decreases as the monitoring depth increases; however this distance is independent of b.

If b, $h_{monitor}$, and a:h are constant, while a and h increase, the normal strains reverse signals at a lateral distance of $x/a = 10$. Although the decrease in normal strain magnitude is nearly proportional to the change in a, the decrease in tilt shows the effect of increasing a. Increasing a and h, results in a longer ellipse at greater depth. This shifts the depth of tilt reversal to greater depths, while the monitoring depth, $h_{monitor}$ remains constant. At a given depth, the maximum values of ε_x are approximately three times ε_y and two times the maximum value of ω_{xy}.

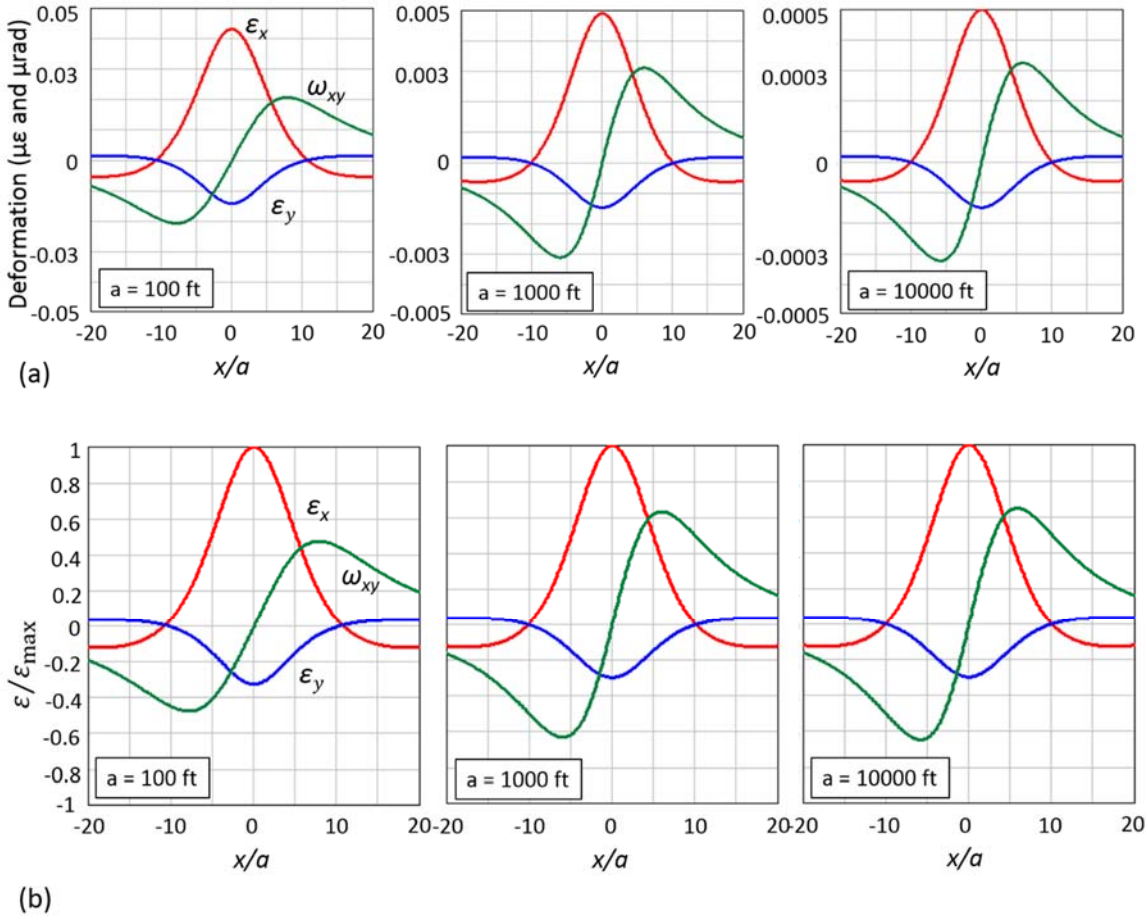

Figure 2.11. (a) Plots of normal strains and tilt at a monitoring depth $h_{monitor}$ 100 ft. The ratio $h/a = 10$ is maintained for the changing ellipse size, while $b = 10$ ft. (b) Dimensionless plots of deformation normalized by the maximum strain ε_x = 43, 4.9, and 0.5 nε for a = 100, 1000, and 10000 ft, respectively.

2.4.3. Pressurized 3-D inclusion

Solving for the strains induced by an arbitrary 3-D reservoir geometry and arbitrary inclusion pressure distribution can be done directly by using the classic *Mindlin and Cheng* [1950a, 1950b] result for a point source in a homogeneous elastic half-space. Essentially, they expressed the solution for a half-space through a simpler solution for the corresponding full space with the same point source. We use their solution as a Green's function as our model (Figure 2.12a) includes a region, *V*, that undergoes a volumetric transformation strain, $\varepsilon_0 = \alpha\Delta p/K$, where Δp is the local pressure change, α is the poroelastic Biot-Willis coefficient, and *K* is the drained bulk modulus of the reservoir rock. This section is based on the results of *Germanovich* [2017]. The vertical displacement at point $r = \{x, y, z\}$ in the half-space $z \geq 0$ (Figure 2.12a) is expressed as

$$u_i(x,y,z) = u_i^0(x,y,z) + (3-4\nu)u_i^0(x,y,-z) + (-1)^\delta 2z\frac{\partial}{\partial z}u_i^0(x,y,-z) \qquad (2.9)$$

where $i = 1, 2,$ or 3, corresponds to the *x*, *y*, and *z* directions, respectively, and $\delta = 1$ for $i = 1, 2,$ while $\delta = 0$ for $i = 3$. The displacements

$$u_i^0(x,y,z) = -\frac{1}{4\pi}\frac{\partial \varphi_0}{\partial x_i} \qquad (2.10)$$

would occur in the infinite space, $-\infty < z < \infty$, with region *V* at the same location in its lower half-space $z \geq 0$. The potential

$$\varphi_0(x,y,z) = \frac{1}{3}\frac{1+\nu}{1-\nu}\int_V \frac{\varepsilon_0(r_1)d^3r_1}{|r-r_1|} \quad (r_1 = \{\xi_1, \xi_2, \xi_3\} \in V) \qquad (2.11)$$

where $|r - r_1| = [(x-\xi_1)^2 + (y-\xi_2)^2 + (z-\xi_3)^2]^{1/2}$, integration variables ξ_1, ξ_2, and ξ_3 are the *x*, *y*, and *z* coordinates inside *V*, respectively, and ν is the Poisson's ratio.

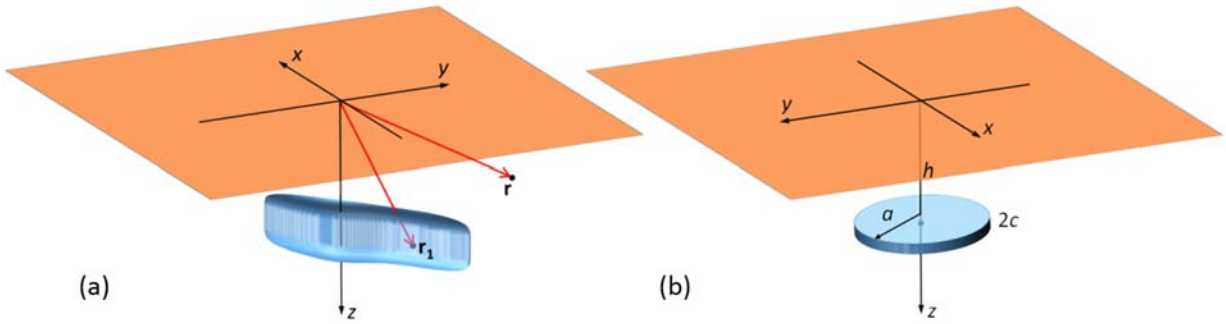

Figure 2.12. (a) Pressurized inclusion within an elastic half-space described by equations (2.9) through (2.11). (b) Geometry of the cylindrical pressurized region with a radius *a* and thickness *2c* embedded at a depth of *h.*

Therefore, finding displacements, and hence, tilts and strains in the half-space with a region undergoing transformation strain is essentially reduced to evaluating the integral in (2.11), which is a classic task of the potential theory and is relatively straightforward for many pressure distributions and inclusion geometries [e.g., *Germanovich et al.*, 2012; *Helms*, 2014; *Guido et al.*, 2015].

2.4.4. Deformation induced by a pressurized cylindrical region

As an estimate of deformation during fluid injection into a geologic formation, we consider the case of a pressurized cylindrical region in an infinite half-space (Figure 2.12b). The volume of a pressured region dominates deformation within an infinite half-space [e.g., *Germanovich et al.*, 2012]. In a confined horizontal reservoir, the pressurized zone will expand radially in a cylindrical pattern. This is representative of long-term injection (i.e., near uniform pressure distribution) into a reservoir (k_1) of finite dimensions embedded in a very low permeability medium (k_2), such that $k_1 \gg k_2$. Alternatively, this may be viewed as the pressure distribution (albeit very approximate) during injection into a homogeneous reservoir at a specific time. In this case, the pressurized region represents a zone of pressure influence, where the radius of the cylindrical region grows in time and can be considered a proxy of time. Solving the 3-D analytical solution allows insight into measurable values of deformation that may occur in field testing.

The strains induced by a pressurized cylindrical region were solved analytically using equations (2.9) through (2.11), for a homogenous material of Young's Modulus E = 15 GPa, Poisson ratio ν = 0.23, and Biot-Willis coefficient α = 0.75. An inclusion of thickness $2c$ = 50 ft is imbedded at a depth of h = 1500 ft. Free displacement is allowed on the xy plane at z = 0 as the cylindrical region is uniformly pressurized to p = 300 psi.

We investigate the deformation as the radius of the pressurized region a_i increases. In particular, we consider the strains and tilts at radii of r_1 = 500 and r_2 = 1000 ft when the inclusion has radius a_1 = 200 ft, a_2 = 400 ft, a_3 = 800 ft, and a_4 = 2000 ft (Figure 2.13). The magnitudes of strains are typically greatest at depths approaching the depth of the inclusion, however, we focus on the deformation in the shallow subsurface where monitoring instruments would be located. Signals decrease at shallower depths, reach a turning point, and increases again towards the free surface. Generally, ε_r and ε_ϕ are tensile and ε_z is compressive. They are on the order of 0.1 με in

the shallow overburden. When a << r, strains are nearly 1 order of magnitude smaller and ε_r becomes compressive and ε_v tensile at greater depths. For $a_i < r_i$, the difference of the local minimum and strain values at z = 0 to z = 500 ft is small (Figure 2.13). When $a_i > r_i$, strain magnitudes increase and the difference between maximum and minimum signals becomes more pronounced (Figure 2.13b) and the depth of local minimums of strain increases gradually as the radius of the pressurized region spreads.

Tilt decrease nearly linearly with depth in the shallow overburden. It is negative at depths approaching the inclusion, but becomes positive at shallow depths due to the bulging effect on the free surface. The vertical gradient of tilt remains relatively constant for small r. At greater r, gradient is initially very small, but doubles as a becomes greater than r. The depth of tilt reversal increases as a increases. This may have important implications for monitoring an injection

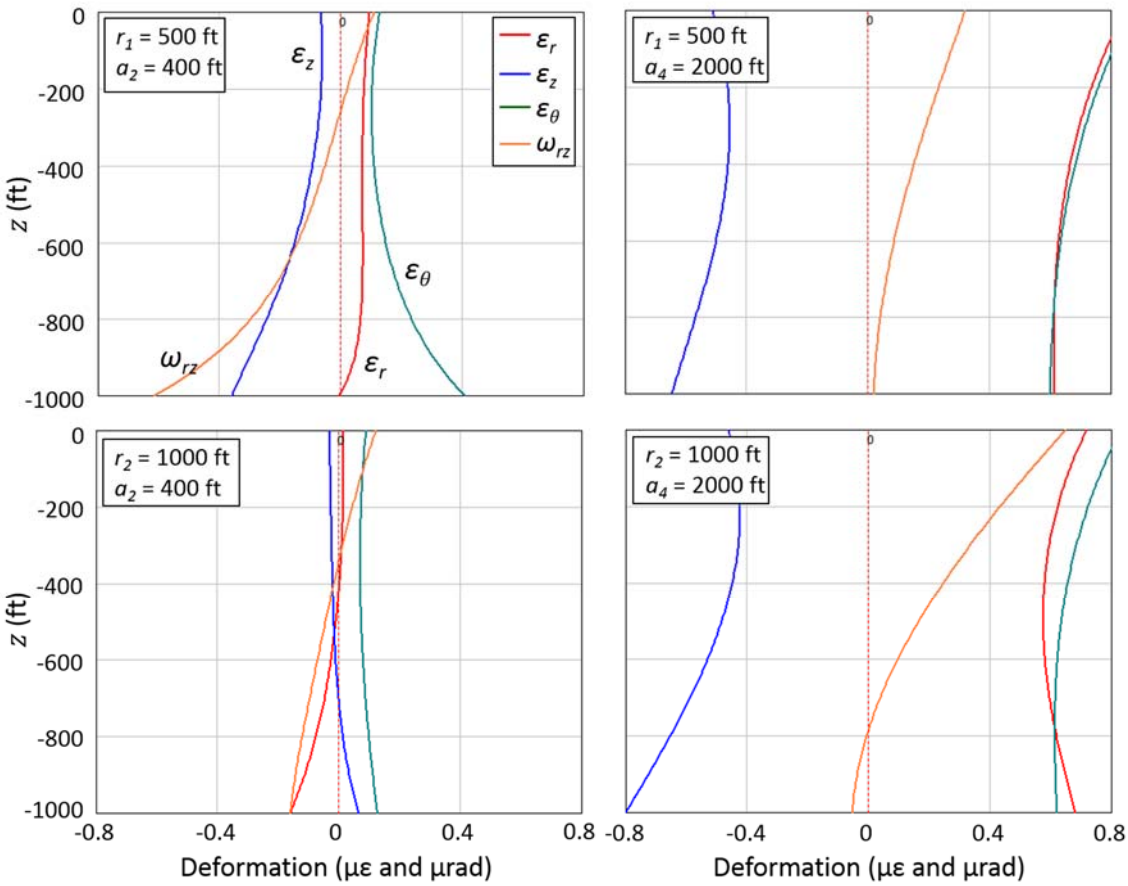

Figure 2.13. Vertical profiles of deformation at radial distances of r_1 = 500 and r_2 = 1000 ft. Signals are recorded for the pressurized cylindrical region in Figure 2.12 when a_2 = 400 ft and a_4 = 2000 ft.

process. If the instrument is placed below the depth of the tilt reversal at early times, the measured signal will approach zero as the tilt reversal shifts to deeper depths. In contrast, if the instrument is placed above the depth of tilt reversal at early times, the measured signal will always increase with increasing injection.

A major objective of this work is to determine the best locations for strainmeter measurements, yet the deformation occurs in a complex pattern that evolves with injection (Figure 2.13). One possible way to characterize deformation is to determine locations of greatest signal strength, yet it is challenging to characterize this range as locations of minimum strains and tilt inversion do not coincide and vary as the radius of the pressurized region spreads. The strain transient suggests there may be a range of depths that are best avoided during instrument siting.

Deformation is best portrayed by a combination of three signals that can be directly measured by borehole strainmeters. The summation of absolute values of one measurement of tilt and two normal strains are combined into the function

$$\delta = |\omega_{rz}| + |\varepsilon_{\phi}| + |\varepsilon_{z}| \tag{2.12}$$

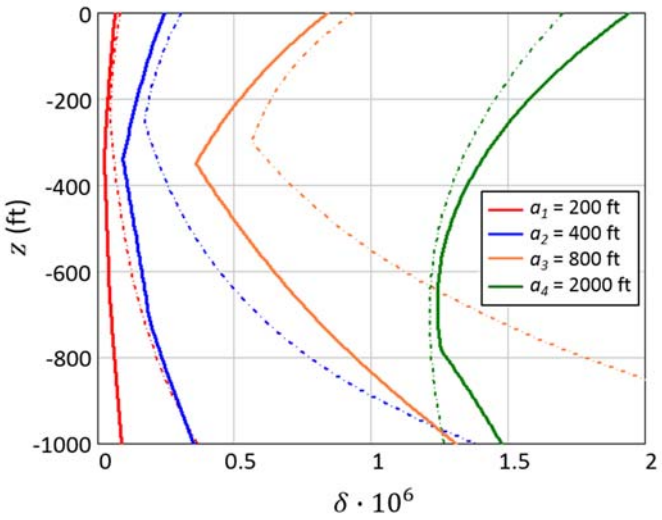

Figure 2.14. The function δ at r_1 = 500 ft (dotted lines) and r_2 = 1000 ft (solid lines). Plots are for pressurized regions of a_1 = 200 ft (red), a_2 = 400 ft (blue), a_3 = 800 ft (orange), and a_4 = 2000 ft (green).

Together, these signals results in a function of deformation that has a distinct minimum value of deformation (Figure 2.14). This value occurs as a discontinuity due to the reversal of the tilt at a depth of several hundred feet, while the depth of minimum δ is also dependent on the vertex of the ε_{ϕ} and ε_{z} profiles. The discontinuity becomes more apparent as a increases, until a

>> *r*. The signal increases as the radius of the pressurized region increases. For the *a* plotted in Figure 2.14, the minimum signal lies at a depth exceeding 300 ft. As *a* increases, the minimum value δ of shift to deeper depths and the signal is stronger closer to the surface. If *a* increases by a factor of two, the strength of the signal increases roughly three to four times.

Defining the deformation in ways other than δ posed several challenges. For example, if the function is reduced to the volumetric strain, then the magnitude of the signal declines by approximately a factor of two as the function is now a competition between the tensile lateral strains and compressive vertical strain (Figure 2.15). The function no longer has a local minimum near the surface and δ always decreases with depth. Adjusting δ to the summation of the magnitude of the normal strains results in an apparent local minimum in the signal. This minimum cannot be clearly observed at smaller monitoring radii and varies by several hundred feet as the

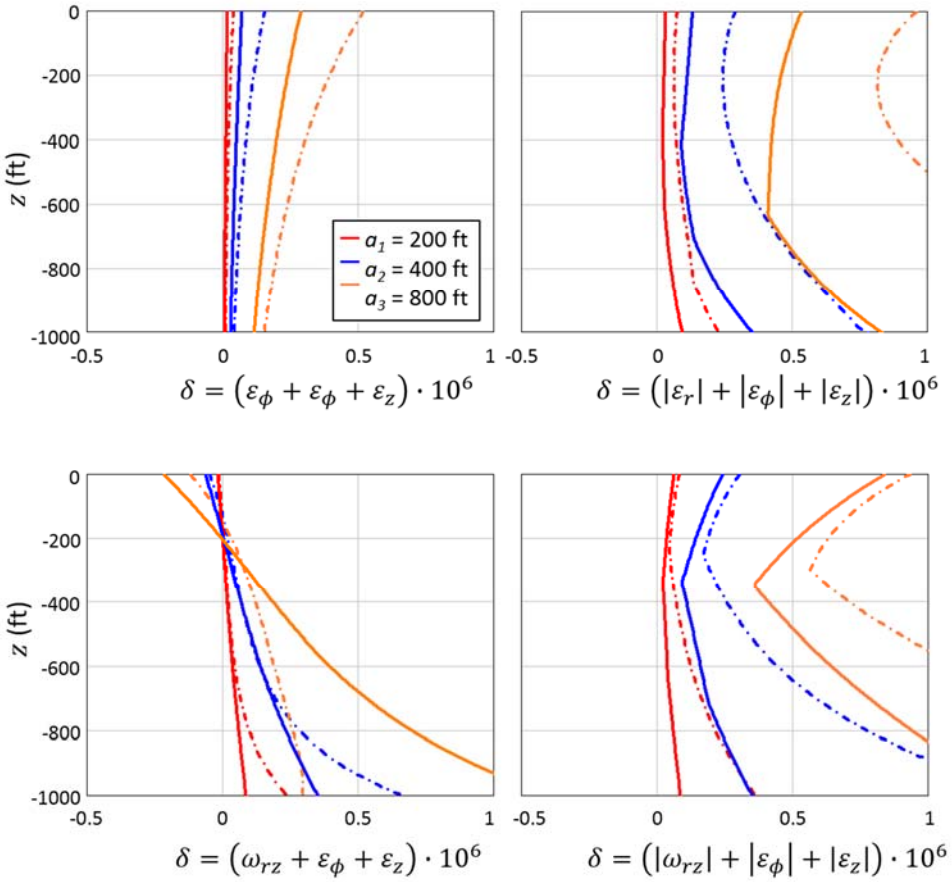

Figure 2.15. Profiles of alternative deformation functions at radial distances of 500 ft (dotted lines) and 1000 ft (solid lines) for inclusions of radii a_1 = 200 ft, a_2 = 400 ft, and a_3 = 800 ft.

pressurized region increases or the monitoring radius increases. Replacing ε_r with ω_{rz} causes δ to be negative at shallow depths 250 ft or less. As the depth increases, δ generally increases. Nevertheless, ε_ϕ is tensile, ε_z is compressive, and ω_{rz} is positive at shallow depths before becoming increasingly negative with depth. This dampens the value of δ. Once δ is defined by equation 2.17, distinct minimum values occur as discontinuities and the magnitude of δ is typically greater than the functions described above. The δ function suggests a zone of minimum deformation that may be best avoided during instrument siting. In this zone, the strains are near their minimum values and ω_{rz} may be below strainmeter resolution.

2.5. Simulated injection at the North Avant field, Osage County, OK

2.5.1. Governing equations of poroelasticity

Most transient models of fluid injection that involve heterogeneities in the field lack an analytical solution. During fluid injection, the addition of the fluid to the reservoir has a mechanical effect on the enveloping rock and this interaction can be described within the framework of linear poroelasticity [e.g., *Detournay and Cheng*, 1993; *Wang*, 2000]. The injection fluid is assumed to be of constant and uniform density such that the conservation of mass of the fluid gives

$$\rho S \frac{\partial p}{\partial t} + \nabla \cdot (\rho \mathbf{u}) = -\rho \alpha \frac{\partial \varepsilon_v}{\partial t} \tag{2.13}$$

where α is the Biot-Willis coefficient, ε_v the volumetric strain, and t is time. The storage coefficient S is defined as $S = \phi\chi_f + \frac{(\alpha-\phi)(1-\alpha)}{K}$ where χ_f is the fluid compressibility. Darcy's Law relates the fluid velocity to pressure change by

$$\mathbf{u} = -\frac{\nabla k p}{\mu} \tag{2.14}$$

where k is the permeability, and μ is the fluid viscosity. Conservation of momentum with Hooke's Law in the poroelastic medium gives [e.g., *Wang*, 2000]

$$\frac{E}{2(1+\nu)}\nabla^2 \mathbf{u} + \frac{E}{2(1+\nu)(1-2\nu)}\nabla \cdot (\nabla \mathbf{u}) = \alpha \nabla p \tag{2.15}$$

where p is pressure, $\mathbf{u}$ is total displacement of the solid, and E is drained Young's modulus, and ν is drained Poisson's ratio.

Seven independent equations (2.13) to (2.15) contain seven unknowns q_i, u_i, and p. To solve these equations (with boundaries and initial conditions formulated below), we use the commercial finite element software, Comsol Multiphysics. This uses the Galerkin finite element

method, adaptive time stepping, and provides considerable flexibility in meshing. Boundary conditions, governing equations, and geometries can be modified to represent particular problems.

Comsol has become a standard geomechanical software with poroelastic capabilities, and has been tested on numerous occasions [e.g., *Murdoch and Germanovich*, 2012; *Holzbecher and Göttingen*, 2013]. *Murdoch et al.* [2016] compared poroelastic simulations in Comsol to FLAC [*Itasca*, 1997], a finite difference code and Abaqus [*SIMULIA*, 2015], a finite element deformation model and determined the resulting deformation generally differed by less than 2% between the software. Additionally, the numerical model of pressurized inclusions in a half-space approaches the close-form poroelastic solutions in both 2-D (Appendix A.1) and 3-D, where improved meshing and increased distance to model boundaries result in greater accuracy of numerical results.

2.5.2. Benchmark axisymmetric injection model

The conceptual model of the North Avant field developed in section 2.3.6 is the basis of our numerical models. The stratigraphy at North Avant field is relatively flat lying with the C zone extending laterally for a distance much greater than the reservoir thickness. As a benchmark model, the injection into the reservoir is represented with an axisymmetric model of injection into a homogeneous, anisotropic layer confined within a domain of lower permeability. This extends on the approach of *Murdoch et al.* [2016] to characterize the deformation at the North Avant field (Appendix A.2). Excluding any heterogeneities, like high energy channels, or variance in material properties allows for an approximation of the deformation expected during injection.

The reservoir is 110 ft thick, overlain by a confining layer 1620 ft thick, and underlain by an 810 ft thick confining layer (Figure 2.16). The lower confining layer is half the thickness of the overburden and roughly corresponds to the maximum expected depth to rigid crystalline rock. We assume average material properties such that homogeneous and isotropic overburden and basement layers confine the reservoir (Table 2.2) The well casing is assumed sufficiently rigid such that displacement does not occur normal to the boundary (roller-type boundary conditions). This neglects well casing and screen effects, however, these effects are limited to strains at small radial distances and do not affect the far-field strains where instruments will be installed (i.e., $r > 200$ ft, Appendix A.5). The boundary at radius r = 5 mi is beyond the region of deformation during simulations up to 100 days and roller-type boundary conditions are applied to the radial

boundaries. The lower boundary also has a roller-type condition and the upper boundary is traction free to allow free displacement at the surface.

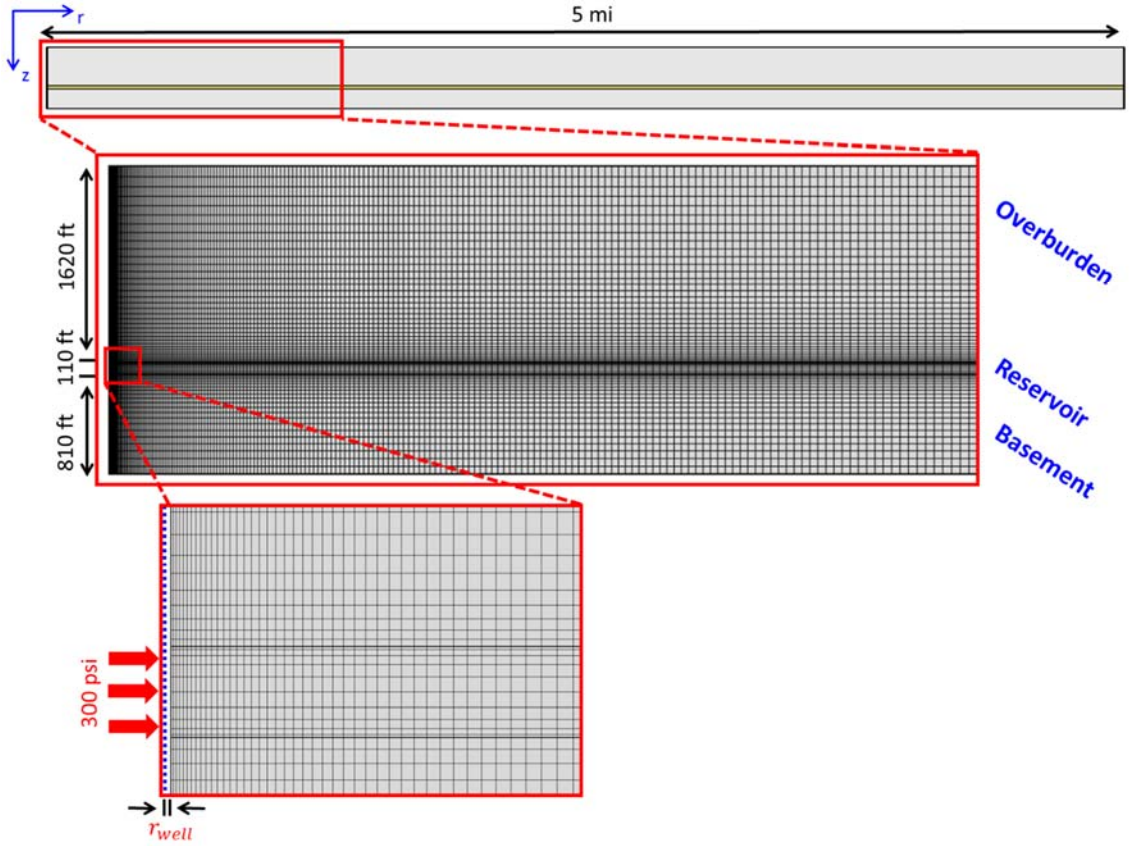

Figure 2.16. Geometry and mesh of the axisymmetric model. The well is not included in the geometry and is represented by an infinite cylindrical radius r_{well}.

We assign constant and uniform elastic properties in all model layers (Table 2.5) using the conceptual model described in section 2.36. Models are initially in static equilibrium with uniform hydraulic head before the onset of injection such that all calculated pressures and displacements are relative to initial conditions. The wellhead pressure during sustained injection was approximately 100 psi (Figure 2.4), and assuming the water level remains constant throughout the injection process, there is an additional 200 psi of hydrostatic pressure in the well. Hence, we apply a constant pressure $p = 300$ psi uniformly along a linesource (radius r_{well} = 6 inches) from the start of simulations. Fluids enter the reservoir at $r = r_{well}$ and are allowed to exit the model through the reservoir at $r = 5$ mi, where the hydraulic head is fixed. Values of permeability $k = 10$ mD and porosity $\phi = 0.20$ were derived by matching simulations of the injection flow rate

against the predicted bottomhole pressure at well 9A (Appendix A.6) and are consistent with measurements made on core and well logs (section 2.3.5).

Table 2.4 Boundary conditions used in numerical models**.**

Boundary	Fluid Flow	Elasticity
Upper surface ($z = 0$)	no flow, $dp/dz = 0$	free, $\sigma_z = 0,\ \tau_{rz} = 0$
Bottom surface	no flow, $dp/dz = 0$	roller, $u_z = 0, \tau_{rz} = 0$
Far extent of confining layer	no flow, $dp/dz = 0$	roller, $u_r = 0, \tau_{rz} = 0$
Well within confining layer ($r = 0.1$ m)	no flow, $dp/dz = 0$	roller, $u_r = 0, \tau_{rz} = 0$[2]
Well within reservoir ($r = 0.1$ m)[1]	pore pressure, $p = 300$ psi	roller, $u_r = 0$[2]
Far extent of reservoir	pore pressure, $p_{out} = 0$	roller, $u_r = 0$

[1]r= 0 in 3-D models

[2]replaced with $\sigma_r = -\alpha p$ for Appendix A.5 (e.g., casing and screen included)

Table 2.5. Poroelastic properties input into numerical models.

Domain	k_h [mD]	k_v / k_h	ϕ	ρ [kg/m^3]	E [GPa]	ν	α
Confining units	0.01	1	0.15	2500	15	0.23	0.75
C zone	10	0.25	0.20	2500	15	0.23	0.75
High energy channel	1000	0.25	0.25	2500	15	0.23	0.75

2.5.3. Subsurface deformation during fluid injection

The formation expands with increasing fluid pressure, pulling confining layers radially outward with it. In general, deformation is greatest at the reservoir depth and there is a bulging effect on the free surface. The vertical strain ε_Z is always compressive and the circumferential strain ε_ϕ is always tensile at depths less than 1000 ft. Strains reach a minimum at shallow depths and increase again toward the free surface (Figure 2.17c). At shallow depths ($z < 1000$ ft) and over the first 100 days of injection, strains are greatest near the well and decrease logarithmically from the well (Figure 2.17a) such that they are tens of nε up to 1 mi from the injection well (Figure 2.17a). Interestingly, ε_r changes from tensile to compressive radially at some distance ahead of the pressure front. The strains ε_ϕ and ε_z increase in time, however, their minimum values nearly

coincide at a depth of 300 ft at all times over 100 days of injection (Figure 2.17c). Normal strains ε_r and ε_z are 50% of their maximum at a radial distance $r = 1000$ ft, while ε_ϕ drops at roughly half the rate.

Adjacent to the wellbore, there is always no tilt due to the symmetric pressure distribution. Tilt moves radially outward in time. Over 100 days, tilt $(\partial u_r/\partial z)$ has a maximum value at radial distances between 1000 to 2000 ft and approaches negligible values as *r* approaches infinity (Figure 2.17b). The tilt is negative at large depths, increases towards the surface, reverses at a depth of 300 to 400 ft, and remains positive up to the free surface. The turning point of tilt occurs at a depth that nearly corresponds with the minimal strains, ε_ϕ and ε_z (Figure 2.17d).

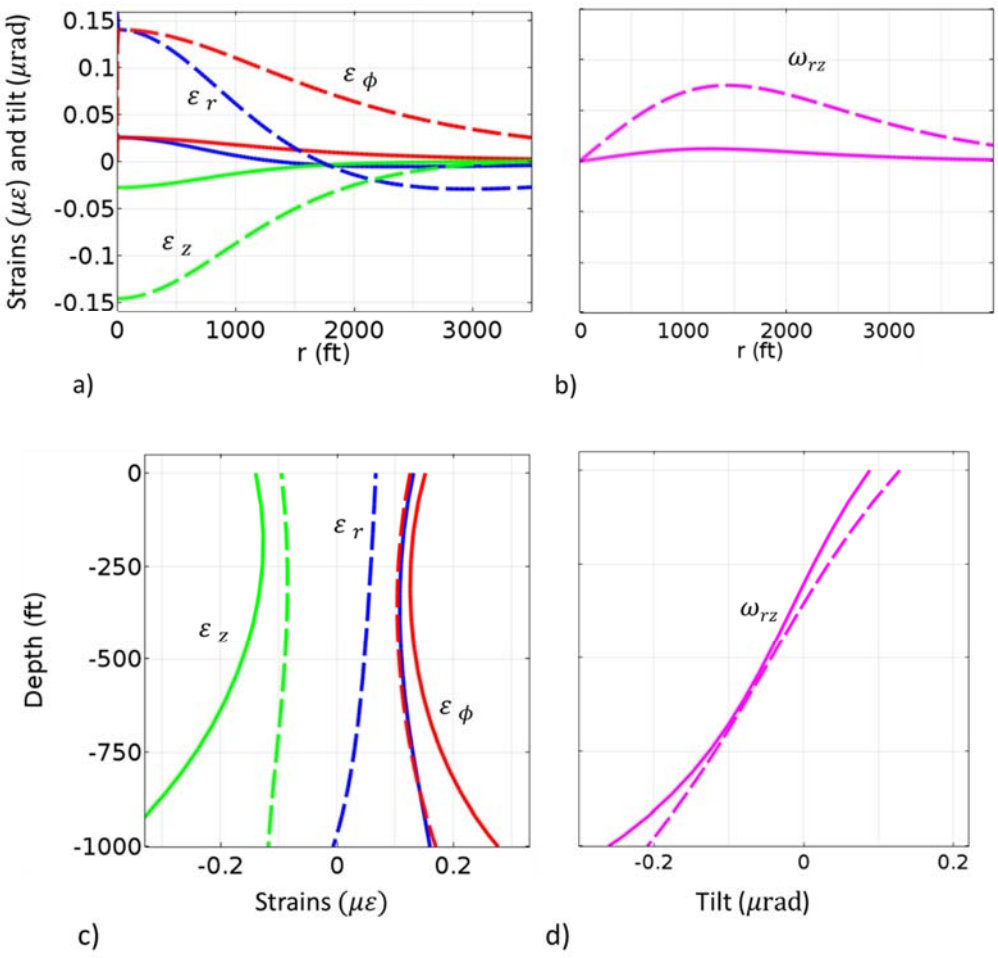

Figure 2.17. Radial profiles of (a) strains and (b) tilt $\omega_{rz} = \partial u_r/\partial z$ at $z = -150$ ft after 1 day (solid lines) and 10 days (dotted lines). Vertical profiles of (c) strains and (d) tilt at $r = 500$ ft (solid lines) and $r = 1000$ ft (dashed lines) after 10 days.

Inspecting strains at a monitoring point is analogous to instrument recordings and two representative recordings are shown in Figure 2.18 for $r = 500$ ft and $r = 1000$ ft at a depth of 150 ft. Strains exceed 0.1 με within a few days and are approximately four times greater than the tilt. At greater radii, strains decrease, but the tilt increases. All measurements are measurable with instrument resolution [e.g., *DeWolf et al.*, 2015] after a few hours of injection and remain measurable throughout the modeling.

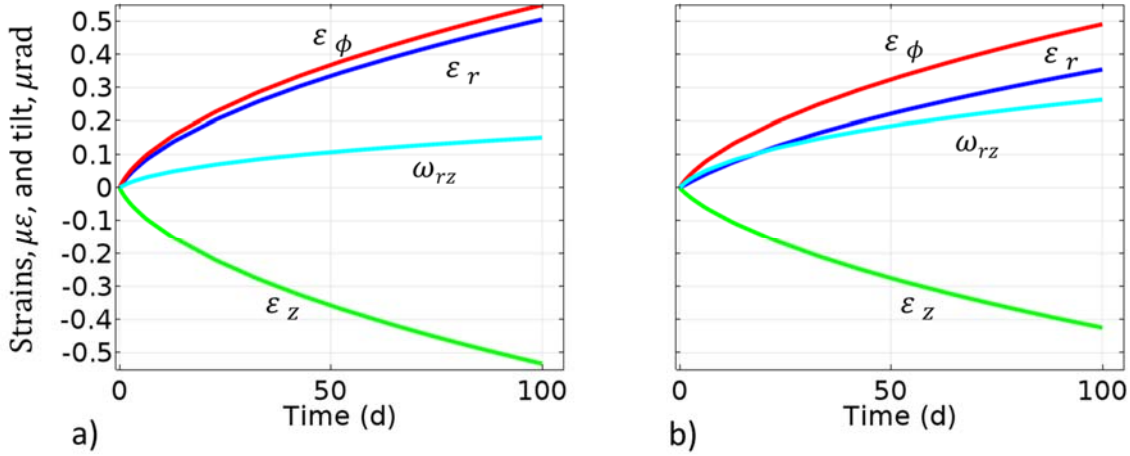

Figure 2.18. Deformation at a depth of 150 ft. Strain and tilts are monitored at radii *r* = 500 ft (a) and *r* = 1000 ft (b).

2.5.4. Zone of greatest deformation signal

The pattern of the function δ (Figure 2.19) in equation (17) is similar to that of the model of a cylindrical pressurized region (section 2.4.3). A distinct local minimum occurs at shallow depths and the discontinuity becomes more pronounced with time. The function also shifts to greater depths with continued injection. Magnitudes of the signal are also comparable between the two models, however, this axisymmetric model shows the evolution of δ in time after injection.

The δ function is greatest at depths near the reservoir. The signal decreases towards the surface, reaching a minimum at a depth between 300 to 400 ft. Locally, the signal increases again towards the surface. In general, δ increases by a factor of four from 2 to 10 days and increases by over another factor of four from 10 to 100 days (Figure 2.19). As in the analytical case, the local minimum moves to deeper depths as injection continues. This further suggests monitoring should be done above the turning point of δ.

Radially, instruments must be close to the well to record the strain, but not so close where the tilt signals are below instrument resolution. The location of maximum signal gradually moves outward with time as the tilt maximum shifts to greater radii. We suggest a lateral range of 500 to 1000 ft, although signals can be detected outside this range.

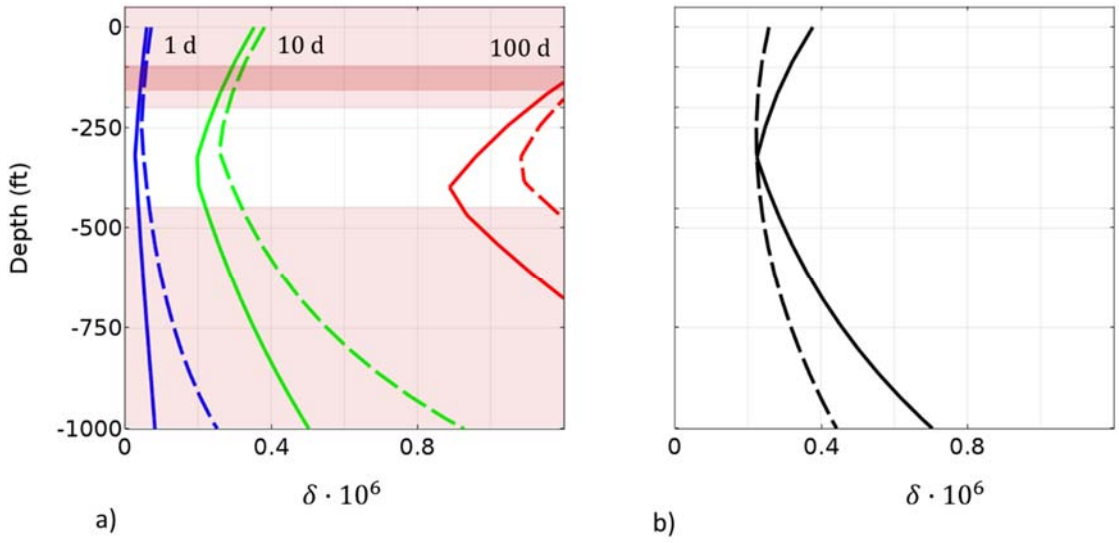

Figure 2.19. (a) Blue, red, and green lines show the vertical profiles of δ at 1, 10, and 100 days, respectively. Dashed lines are profiles at $r = 500$ ft and solid lines are profiles at $r = 1000$ ft. Light red regions are areas of greatest deformation signal and the deep red region is the zone of suggested instrument deployment. (b) Plots of δ (solid line) and $\delta' = |\varepsilon_z| + |\varepsilon_\phi|$ (dotted line) at $r = 750$ ft at t = 10 days.

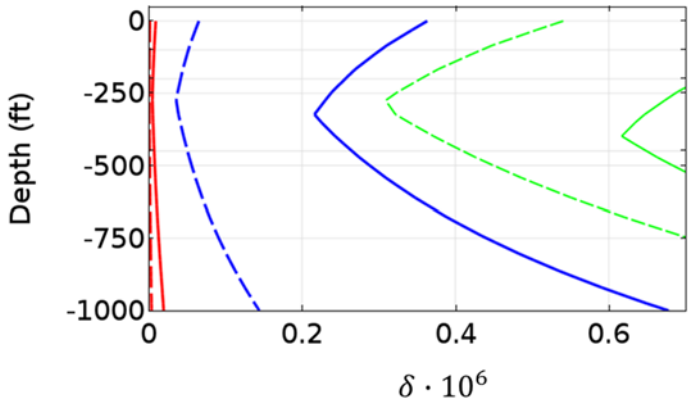

Figure 2.20. Vertical profile of the function delta for reservoir permeabilities varying by three orders of magnitude: k = 0.1 mD (red), k = 10 mD (blue), and k = 100 mD (green) at r = 750 ft. The deformation function is shown after 1 day (dotted lines) and 10 days (solid lines).

We focus on signal magnitude for the δ function to remove complications due to the signs of signals; as ε_z is compressive, ε_ϕ is tensile, and ω_{rz} reverses at a depth of several 100 ft. Other components of strain are not included in the δ function as they obscure the signal. For example, the reversal of the radial strain is at a depth of approximately 1000 ft after 1 day, but shifts towards the surface at greater times such that it is above 500 ft after 10 days (Figure 2.17b). This may have important implications for interpreting the deformation, but results in more variability in the δ function with time. Alternatively, if δ is reduced to only two independent deformation signals (e.g., Figure 2.19b), the parametric curve becomes smoother and minimum values are more difficult to distinguish.

If the permeability of the reservoir differs from what the geologic analysis suggests (section 2.3), the pattern of δ remains consistent (Figure 2.20). Greater reservoir permeability results in greater deformation. At early times, the vertical profile of δ has the local minimum at the same depth regardless of reservoir permeability. As the injection time increases, the minimum value of δ shifts to deeper depths as the pressure diffuses more rapidly through the reservoir. It is worthwhile to note that an increase in reservoir permeability is representative of higher injection rates due to the prescribed constant pressure at the injection site.

2.5.5. Comparison to analytical solution

Our analysis suggests it may be sufficient to use the robust analytical solution to determine where to place instruments to monitor injection to limit the use of more computationally expensive numerical models to inverse modeling of measured strainmeter signals. At early injection times, the deformation of the numerical model closely matches the analytical solution (Figure 2.21). This is due to the constant pressure boundary condition, which has a sharp pressure gradient near the injection site at the onset of injection. During continued injection, the radial gradient becomes less pronounced as the fluid diffuses radial. This results in greater divergence of the solutions at greater times. More specifically, for increasing *a*, the deformation increases more rapidly at smaller *r*, but the rate of increase is less at greater *r*. If *a* is selected to match the discontinuity (minimum δ), the vertical gradient of δ increases more rapidly such that deformation in the analytical solution in greater than the numerical model. This reflects the steep drop in the pressure across the boundary of the pressurized inclusion compared to the Gaussian distribution of reservoir pressure in numerical models.

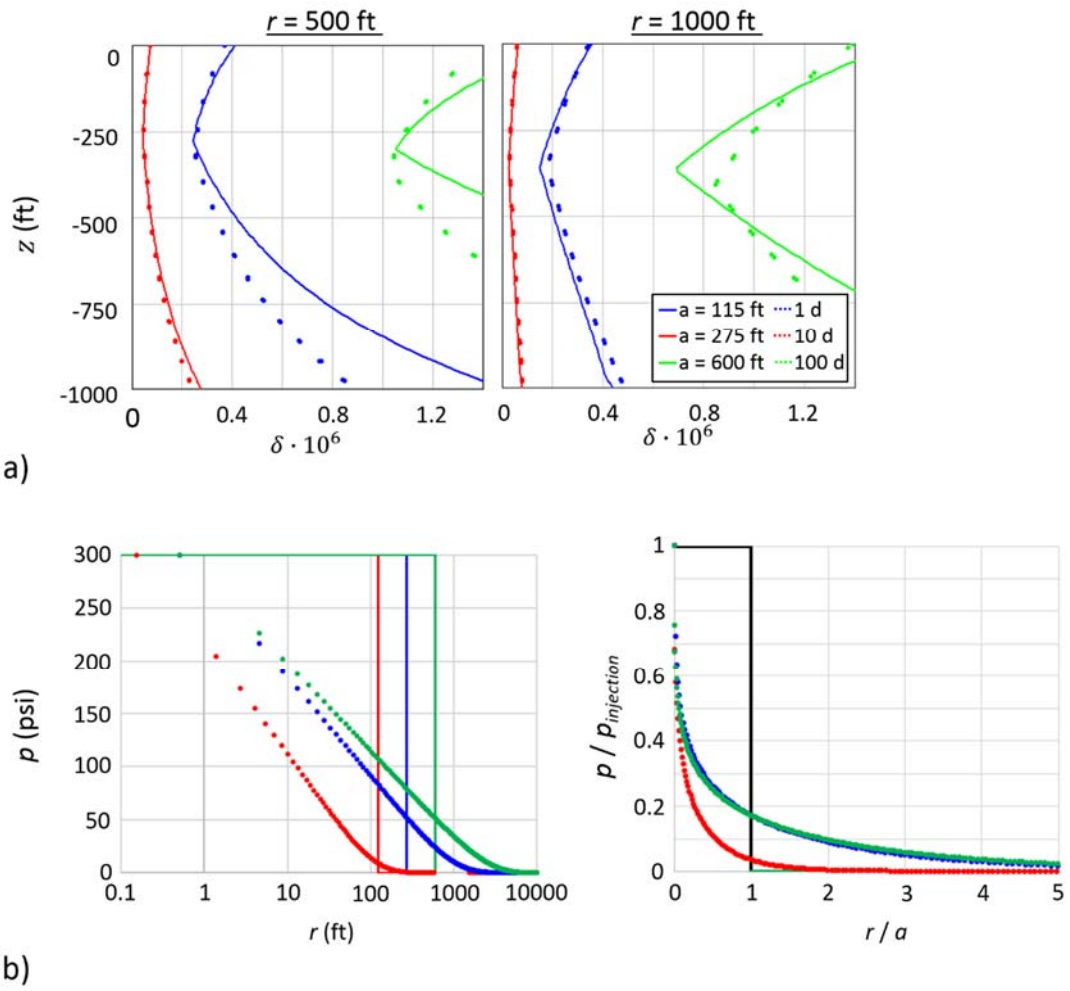

Figure 2.21. Comparison of (a) the δ function and reservoir pressure (b) for analytical solution (solid lines) and numerical model (dotted lines) for the pressurized cylindrical inclusion and axisymmetric model, respectively. Times plotted are t = 1 day (blue dotted line), 10 days (red dotted lines), and 100 days (green dotted lines).

2.6. Permeability variations within Bartlesville sandstone

2.6.1. 3-D model of injection into high permeability channels

Reservoir heterogeneities alter the pressure distribution in the reservoir and affect the deformation pattern within the overburden [*Murdoch et al.*, 2016]. Within fluvial deposits such as the Bartlesville sandstone, variable permeability within reservoirs is common [e.g., *Barwis et al.*, 2012]. At the North Avant field, well 9A intersects a high energy channel 35 ft thick that trends along a northeast axis with a width of approximately 2000 ft. The channel allows for higher

injection rates (at a constant pressure) and focuses the flow of injected fluids. The length of the channel is poorly constrained (Figure 2.7b), resulting in uncertainty in the migration of fluid. We suggest a spatial arrangement of strain and tilt measurements may be able to characterize the dimensions during an injection test.

The benchmark model (section 2.5.2) was modified to a 3-D model with a high energy channel at the base of the C zone. Two simulations of fluid injection into a homogeneous reservoir underlain by *(i)* a finite channel 7920 ft long and *(ii)* an infinite length (Figure 2.22) were compared against the benchmark case of a homogeneous reservoir. For the benchmark case of a homogeneous reservoir, the C zone is 110 ft thick throughout the model. In the heterogeneous models, the C Zone is reduced to the upper 75 ft, and the lower 35 ft is a high energy channel. In effect, this results in variations of the reservoir thickness. In the homogeneous model, the C zone is continuous throughout the model, however, models that include the high energy channel have lateral boundaries along the high energy channel. This reduces the reservoir to only a 75 ft thick C zone at locations away from the high energy channel. Laterally, we utilize the symmetry along channel axes to reduce the geometry to $x > 0$ and $y > 0$. Injection occurs along -1730 ft $> z > -1620$ ft at $x = 0, y = 0$. The high energy channel is 1000 ft wide along the y-axis from $0 \leq y \leq 1000$ ft. For the case of an infinite channel, the high energy channel extends continuously along the x-axis. The finite channel has a length that extends from $0 \leq x \leq 3960$ ft. The overburden remains 1620 ft thick, but the lower confining layer is reduced to 540 ft ($1/3$ the overburden thickness) and radius of the model to 21120 ft. This was done to facilitate calculations, but is expected to have a small effect on the overburden at shallow depths.

Overburden deformation due to channel inclusion is much greater than deformation due to channel shape. For example, if the basal contact of the high energy channel is changed from an ellipse to a rectangle in a 2-D plane strain model, strains are already within 5% of each other at a depth of 600 ft. The difference will become even less at shallower depths, so we assumed a rectangular channel to facilitate computations.

Parameters of the high energy channel models are consistent with the axisymmetric benchmark case, except for permeability. The high energy channel permeability (k = 1000 mD) is two orders of magnitude greater than the permeability of the overlying reservoir (k = 10 mD) and four orders of magnitude greater than the permeability of the confining layers (k = 0.01 mD) (Table 2.5). The largest strain rates occur at early times, so we simulate injection for 10 days.

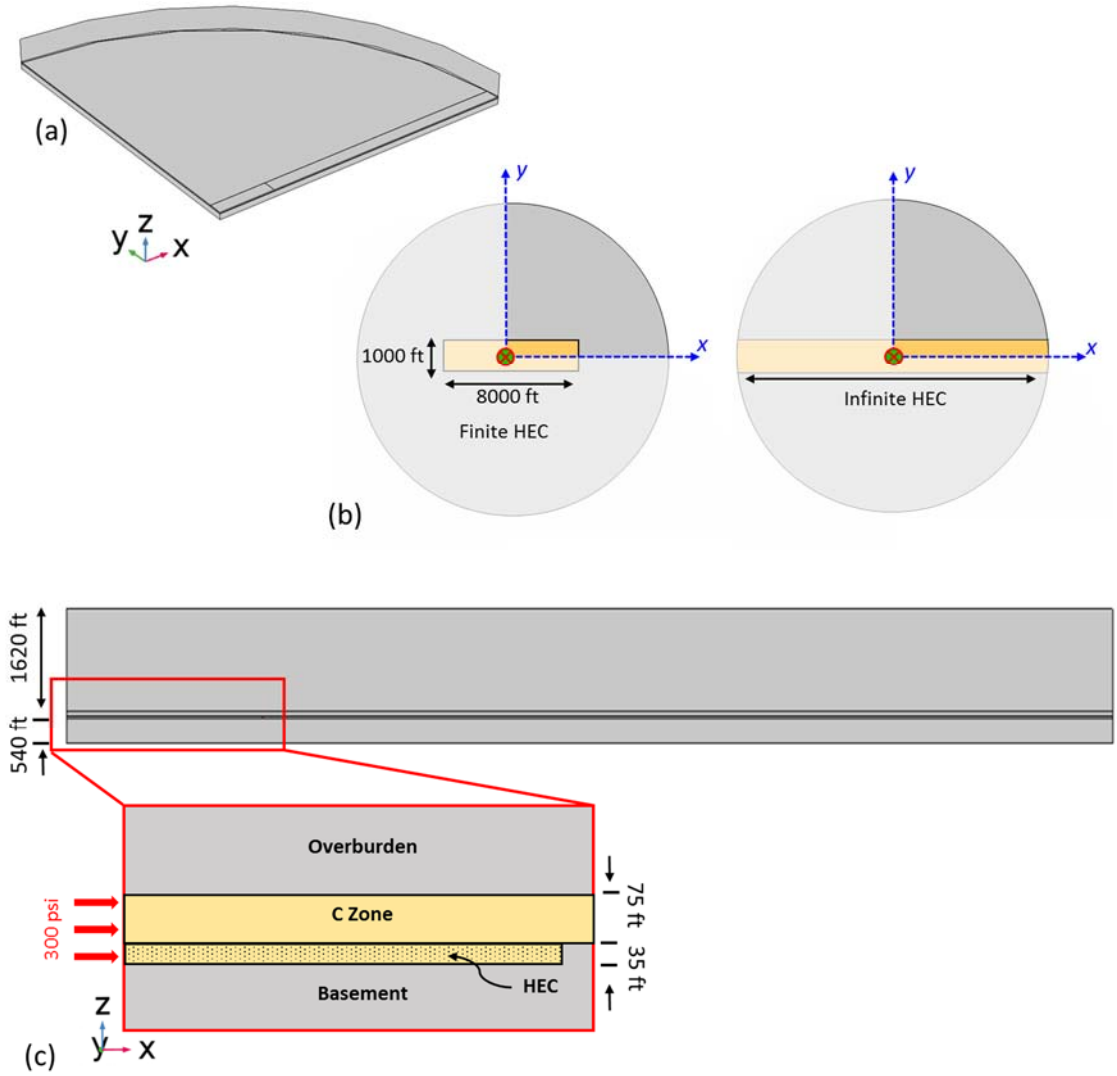

Figure 2.22. (a) Geometry, (b) plan view, and (c) cross-section of the 3-D model of variable channel length. Axial symmetry is applied along the axis of the channel at $x = 0$ and $y = 0$ such that a quarter section of the subsurface is modeled. The channel extends along the x-axis. Injection at a constant pressure of p = 300 psi occurs at $x = y = 0$ (yellow star in (a) and 9b), red arrows in (c). (a) The upper surface and boundaries at x = 0 and y = 0 are hidden to show the underlying channel geometry. (b) Two cases of channel length were modelled: a finite channel 1.5 mi long and a channel that is continuous across the model. Injection occurs at the center of the channel. (c) The reservoir is 110 feet thick at the injection site in all cases, but is reduced to 75 ft away from the high energy channel. In the benchmark case, the C zone is always 110 ft thick and no high energy channel (HEC) is present.

2.6.2. Zone of greatest deformation signal

Lateral permeability change result in more rapid deformation such that δ is several times greater in models that include the high energy channel. The function δ increases with added borders, even at monitoring distances significantly less than the lateral distance to boundaries of permeability change (Figure 2.23). The profile of δ is similar, with a local minimum at a depth of several hundred feet, however, the inclusion of a high energy channel causes the minimum δ to shift to approximately 25% greater depth. As the number of lateral permeability boundaries increases, the depth of minimum δ further increases, although this is on the scale of feet to tens

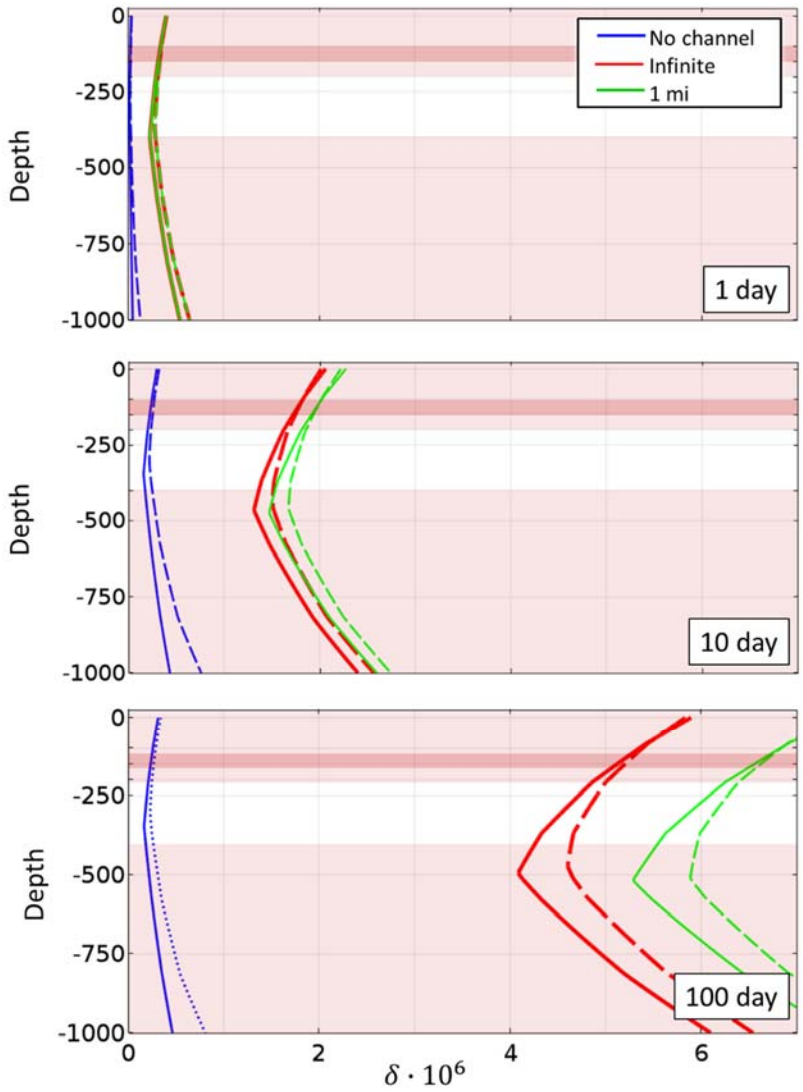

Figure 2.23. Vertical profile of δ at r = 500 ft (dotted) and r = 1000 ft (solid) for the 3-D that excludes the channel (blue lines), infinite channel length (red lines), and channel with a length of 1 mile (green lines). The radial distance $r^2 = \sqrt{x^2 + y^2}$, where $x = y$.

of feet. Nevertheless, this analysis suggests that permeability variations in the reservoir do not greatly alter the vertical trend of δ and the benchmark model accurately predicts the correct depth of the minimum deformation signal.

2.6.3. Effect of high energy channel on shallow deformation pattern

During injection at a constant pressure, the formation pressure rises more rapidly in the high energy channel than in the overlying C zone and this is reflected in the deformation pattern. Deformation focuses over and adjacent to the high energy channel and increases with added boundaries. Below, we discuss the effect of the high energy channel on the deformation at a monitoring depth of 150 ft and time of 10 days.

The change in strain compared to the benchmark case is greatest over the high energy channel. Differences to the strain field are greatest near the injection well and decrease at greater radii (Figure 2.24). In both cases, maximum and minimum differences in strain are nearly equal for both cases of high energy channel inclusion. Lateral strains increase by a maximum of 0.5 $\mu\varepsilon$ and 1 $\mu\varepsilon$ for ε_x and ε_y, respectively (Figure 2.24). This is a clear indication of a permeability boundary being crossed. Interestingly, there is also a small drop (approximately 20% of the maximum value) outside of where borders are encountered perpendicular to the strain component. At the border x = 3960 ft, the decrease of ε_x is three times greater for the finite channel than for the case of an infinite channel (where there is no permeability change). In contrast, ε_y is similar, regardless of the channel length. Hence, differences from the benchmark model (homogeneous conditions) in the horizontal strain pattern may be used to determine channel orientation (and the corresponding preferential flow path). An increase in lateral strains is expected over high permeability regions in the reservoir. Further, a decrease in horizontal strains is a sign of a permeability boundary being crossed.

The increasing lateral strains corresponds to a decrease in vertical strain over the channel (Figure 2.24). After 10 days, ε_z decreases by a maximum of approximately 0.75 $\mu\varepsilon$ near the injection site. The infinite channel has a more gradual drop in ε_z along the axis of the channel compared to the sharp decrease at the border of the finite channel. Therefore, a decrease in ε_z is also a clear sign of a more permeable zone in the underlying reservoir.

At the monitoring depth, the tilt ω_{xz} increases by up to 0.4 $\mu\varepsilon$ adjacent to the region overlying the high energy channel (Figure 2.25). The difference is greatest at locations adjacent

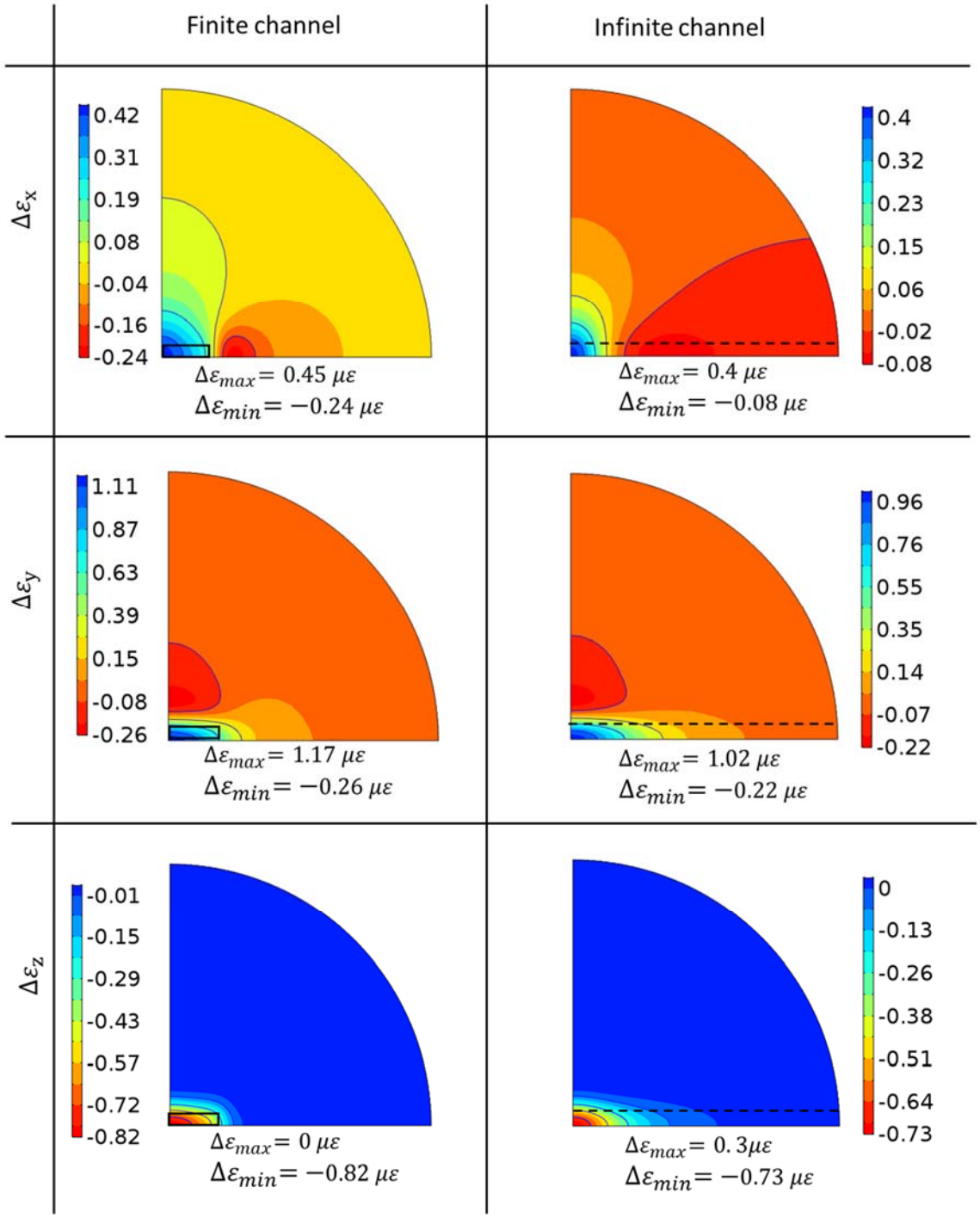

Figure 2.24. Differences in normal strains (strain for cases of high energy channels minus strain of homogeneous reservoir) at a depth of 150 ft after 10 days for the 3-D model of channel length. Contour lines show the difference in strain compared to the general case of no channel. The solid black rectangle is the location of the underlying high energy channel in the finite case, and the dotted black line is the boundary of the infinite channel.

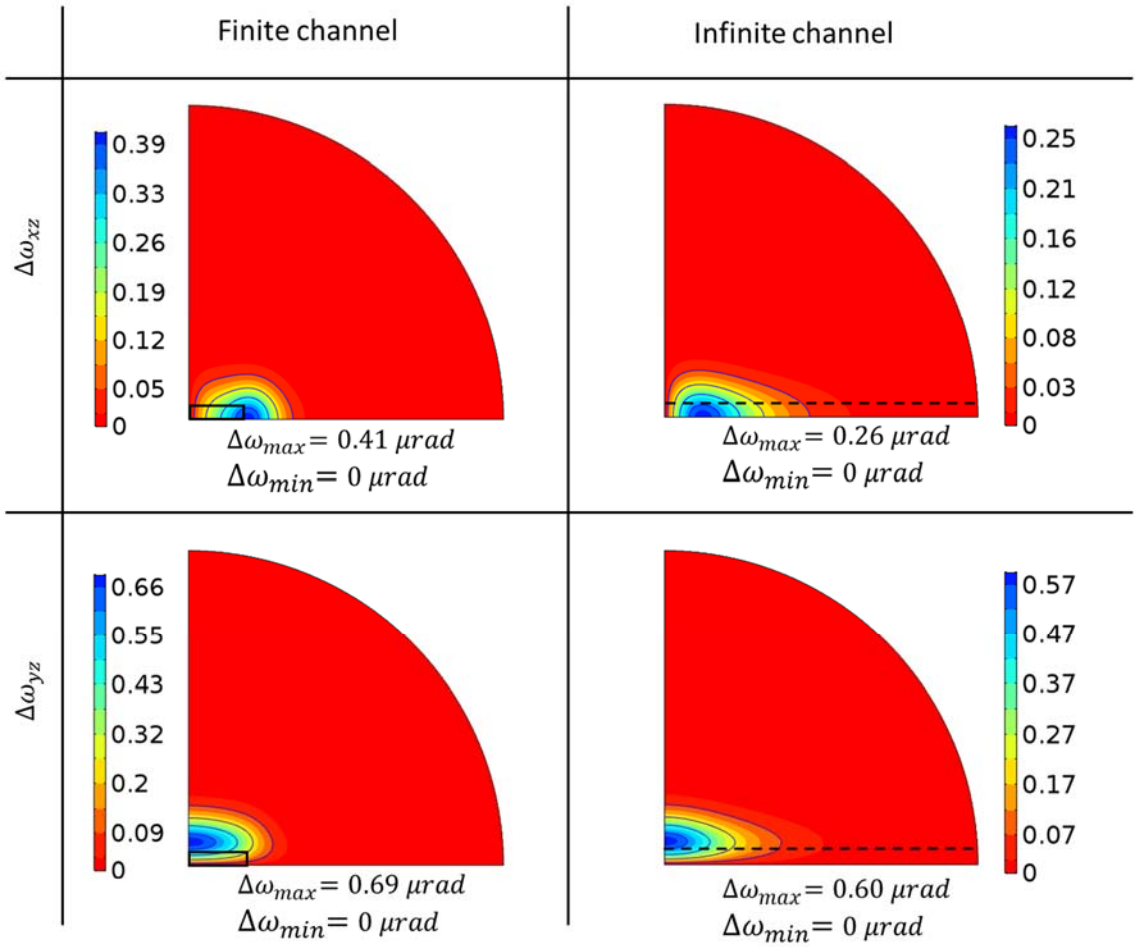

Figure 2.25. Differences in tilts (tilt for cases with high energy channel minus tilt of homogeneous reservoir) at a depth of 150 ft after 10 days for the 3-D model of channel length. Contour lines show the difference in tilt compared to the general case of no channel. The solid black rectangle is the location of the underlying high energy channel in the finite case, and the dotted black line is the boundary of the infinite channel.

to borders perpendicular to the displacement component of tilt. Hence, the maximum of tilt ω_{xz} along the *x*-axis for the case of a finite channel is almost half that of the finite channel, where the lack of a permeability boundary results in a significantly more gradual change in ω_{xz} along the *x*-axis of the infinite channel. The profiles of $\Delta\omega_{yz}$ are similar for both cases of high energy channel inclusion. The maximum increase in ω_{yz} is adjacent to the area overlying $y = 1000$ ft. This value (exceeding 0.6 $\mu\varepsilon$) is slightly greater than $\Delta\omega_{xz}$, likely due to the closer proximity of the boundary along the *y*-axis. The maximum $\Delta\omega_{xz}$ occurs at approximately half the distance of x when compared to the case of a finite channel, yet the gradient is small such that a difference in tilt still occurs. Similar to the gradient of ω_{xz}, the gradient of ω_{yz} is also more gradual along the channel.

A time series of deformation signals at points in the subsurface are representative of measurements recorded by borehole strainmeters. The strains and tilts at four points at calculated for all three cases (Figure 2.26). Points are located 200 ft on either side of the high energy channel boundaries. Both points 1 (1920, 800, -150 ft) and 2 (1920, 1200, -150 ft) are across the high energy channel boundary at y = 1000 ft and points 3 (3760, 500, -150 ft) and 4 (4160, 500, -150 ft) are across the high energy channel boundary at x = 3960. The horizontal distances are greater than those suggested for monitoring, however, this highlights the effect of permeability boundaries on the deformation pattern.

Including the high energy channel in the models causes a significant increase in deformation at all locations. At all points, ε_x is slightly compressive ($\sim\eta\varepsilon$ after 10 days) at the depth of z = 150 ft in the benchmark case. If a high energy channel underlies the C zone, ε_x is in tension and undergoes a nearly identical evolution at points 1 and 2. The strain increases to 0.2 $\mu\varepsilon$ and 0.3 $\mu\varepsilon$ within 10 days for the model of the infinite and finite channel, respectively. For the case of a finite channel at points 3 and 4, the high energy channel causes a more compressive ε_x at early times, but increases in time. This results in strain reversal at point 3 after several days, but ε_x remains compressive outside of the high energy channel (point 4). The strain changes from compressive to tensile in half the time for the finite channel compared to an infinite channel.

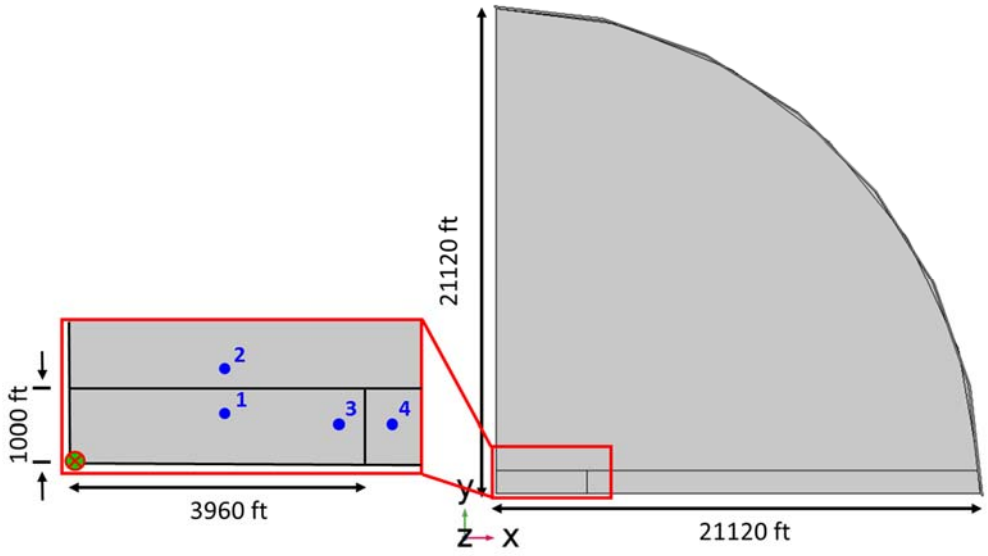

Figure 2.26. Plan view of monitoring points near the boundaries of high energy channels. Blue numbers are the locations of monitoring points (see Figure 2.27) at a depth of *z* = 150 ft: 1 (*x* = 1920, *y* = 800), 2 (*x* = 1920, *y* = 1200), 3 (*x* = 3760, *y* = 500), and 4 (*x* = 4160, *y* = 500).

The magnitude of ε_y is approximately twice as great as ε_x over the high energy channel (points 1 and 3). It is tensile at all points, and the high energy channel inclusion results in similar ε_y, regardless of channel length. At point 1, the strain is approximately 10% greater, but this difference decreases at greater distance from the injection source. The vertical strain is always compressive at the monitoring depth. Over a high energy channel of finite length, ε_z increases nearly linearly in time, while the rate decreases at greater times for an infinite channel. The vertical strain is on the order of 0.1 $\mu\varepsilon$ when the high energy channel is included in the model.

The inclusion of a high energy channel causes the tilts to increase by over one order of magnitude. Tilts parallel to high energy channel boundaries nearly match, regardless of channel length. The most significant variation in tilt signal is the nearly linear increases in $\Delta\omega_{xz}$ across the high energy channel border at 3960 ft. In contrast, over the high energy channel of infinite length, $\Delta\omega_{xz}$ undergoes logarithmic increase. The diffusion of pressure along the infinite high energy channel also results in a smaller $\Delta\omega_{xz}$ at the high energy channel border at y = 1000 ft.

The dimensions of the high energy channels are not well defined by current field data and monitoring wells are unlikely to be installed near the lateral permeability boundaries. In section 2.5.4 we suggest installing instruments significantly closer to the injection well. Compared to measurements near the permeability boundary (2.20 through 2.22), the deformation within our suggested monitoring range is approximately one order of magnitude greater. We investigate three locations near the well, where x, y , and r = 500 ft and 1000 ft (Figure 2.30). Compared to the benchmark model, the vertical strain increases approximately five times and six times if the channel is infinitely long or 1 mile long, respectively over the course of 100 days of injection. Near the injection well, the profiles are similar and variability increases as the lateral monitoring distance increases. Horizontal strains increase by a factor of two when the high energy channel is present, however, these strains have a greater dependence on the horizontal location of the monitoring point. The increase is greatest at locations near lateral permeability boundaries, reflecting the interaction of the pressure redistribution near the permeability boundary as injected fluid flows along the channel. The boundary at y = 1000 ft is nearest to the monitoring point. While the strains ε_r and ε_ϕ are of similar values at r = 500 ft, ε_r is greater at x = 500 ft and ε_ϕ is greater at y = 500 ft. Values of tilt remain significantly less (by several factors) than the strain. Similar to ε_r, ω_{rz} increases more rapidly at y = 500 ft and decreases as the monitoring locations are shifted away from the lateral permeability boundary.

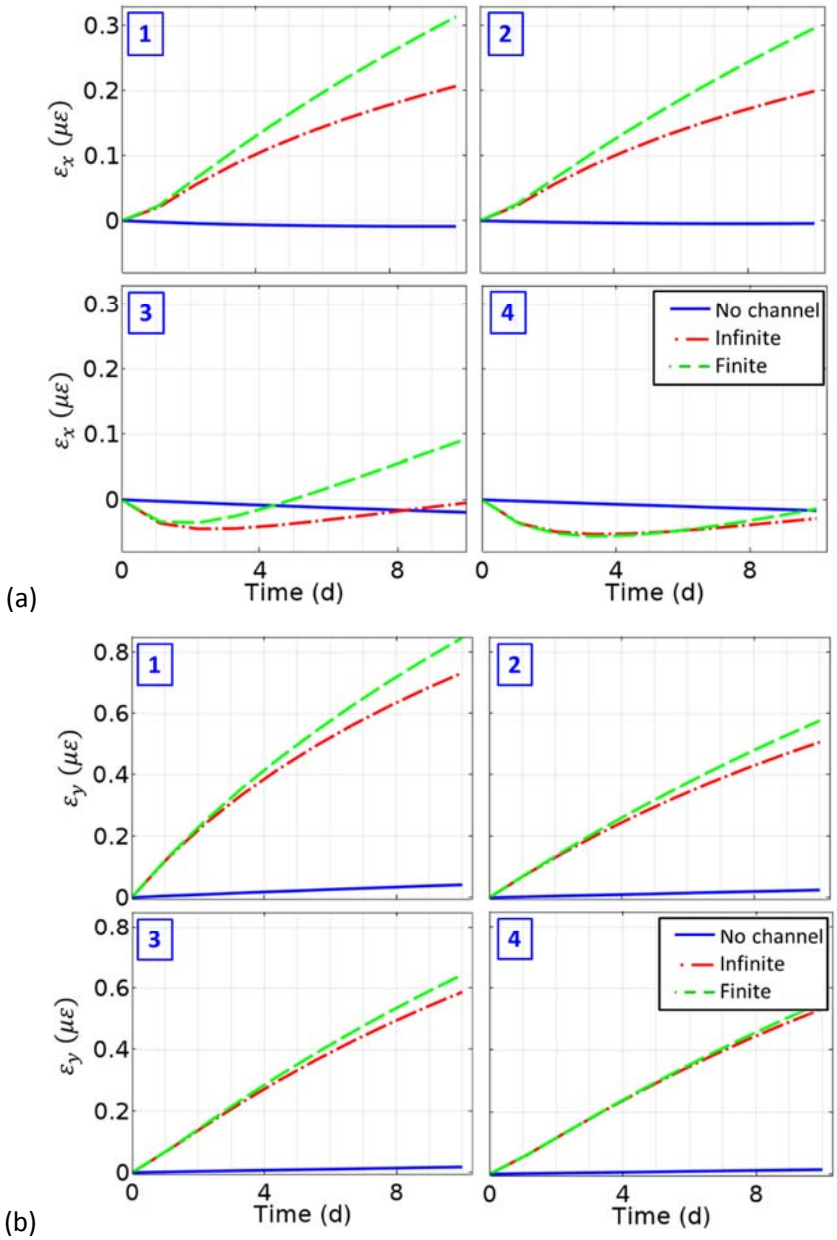

Figure 2.27. Evolution of (a) ε_x and (b) ε_y at the four monitoring points in the 3-D model of channel length. Coordinates of the points are: 1 (1920, 800, -150 ft), 2 (1920, 1200, -150 ft), 3 (3960, 500, -150 ft), and 4 (4160, 500, -150 ft).

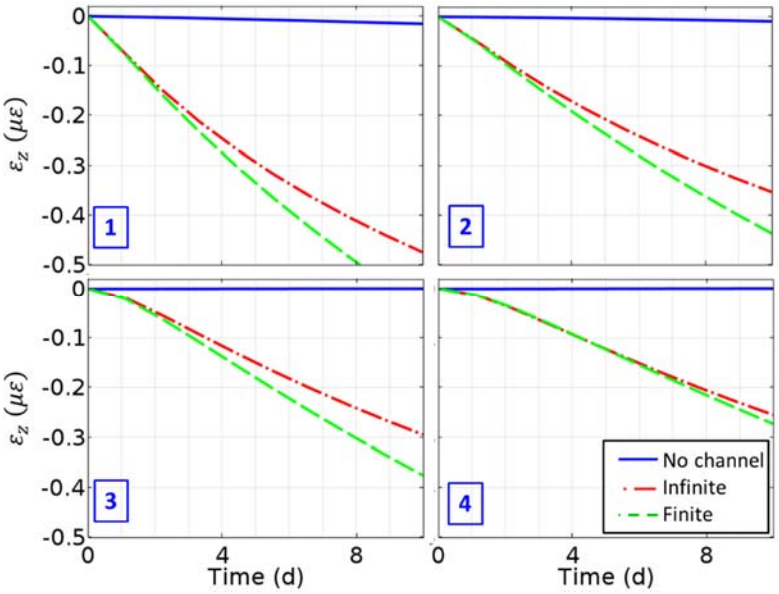

Figure 2.28. Evolution of ε_z at the four monitoring points in the 3-D model of channel length. Coordinates of the points are: 1 (1920, 800, -150 ft), 2 (1920, 1200, -150 ft), 3 (3960, 500, -150 ft), and 4 (4160, 500, -150 ft).

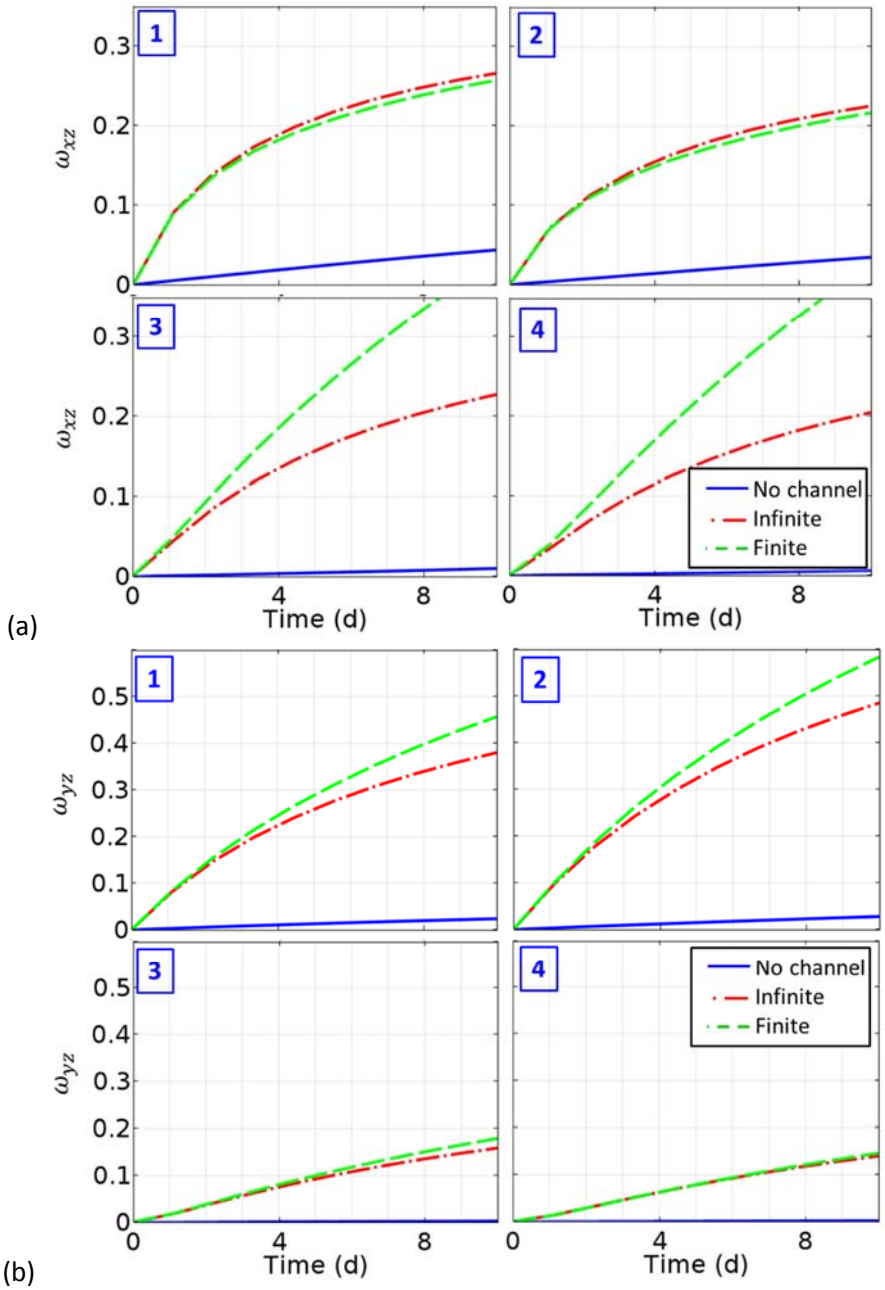

Figure 2.29. Evolution of (a) ω_{xz} and (b) ω_{yz} at the four monitoring points in the 3-D model of channel length. Coordinates of the points are: 1 (1920, 800, -150 ft), 2 (1920, 1200, -150 ft), 3 (3960, 500, -150 ft), and 4 (4160, 500, -150 ft).

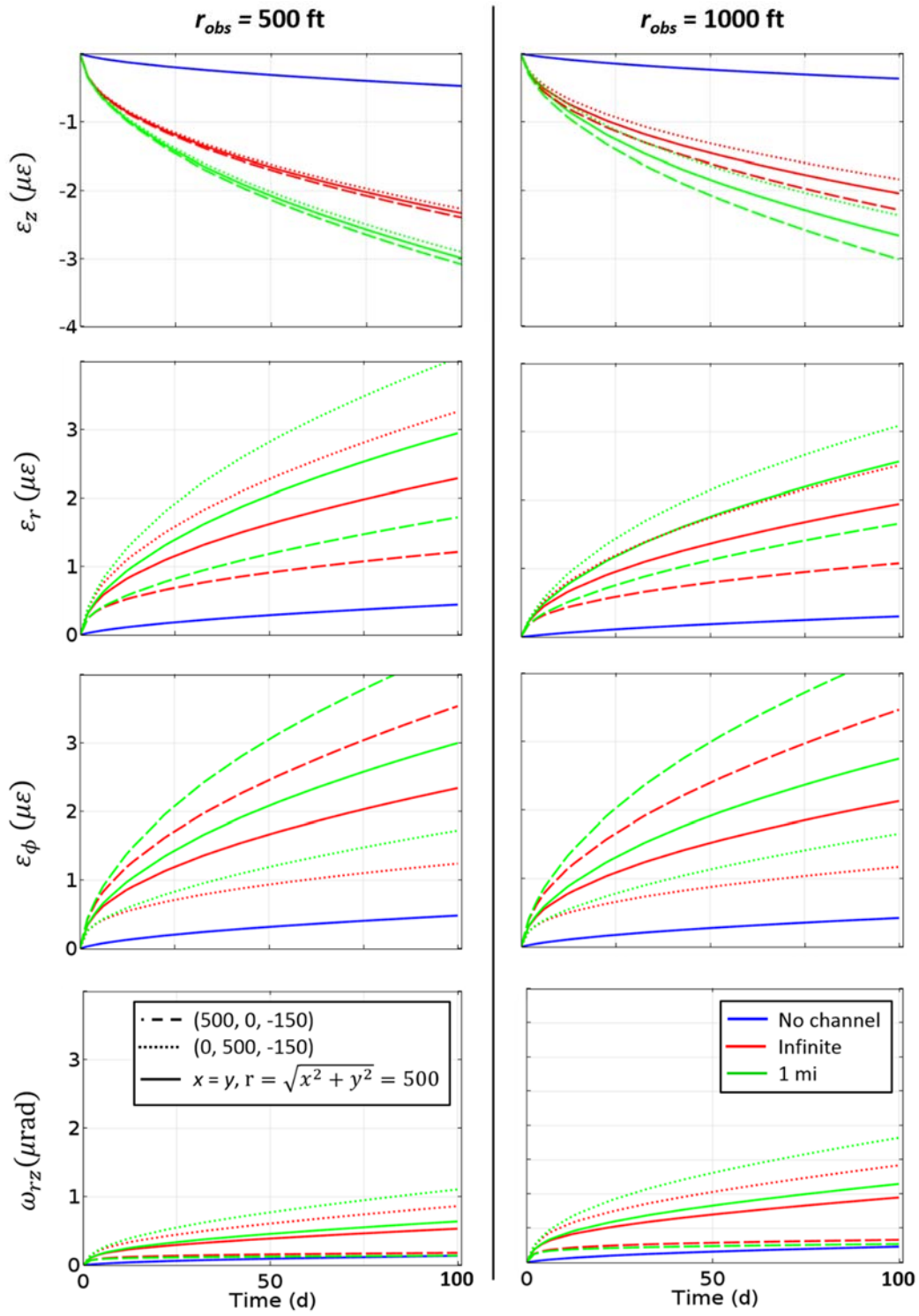

Figure 2.30. Strain signals for 100 days of injection at x, y, r = 500 ft and 1000 ft, and z = -150 ft.

2.7. Discussion

2.7.1. Application to field demonstration of analog CO_2 sequestration

The analytical solution of the induced strains in the vicinity of a pressurized region is very fast and accurate and provides an initial basis for interpreting field data. If injection occurs into a sufficiently confined reservoir over an appropriate timescale, this solution may suffice for estimating deformation during injection. At the North Avant field, the high energy channel at the base of well 9A is likely to be much longer than its width, approaching plain strain conditions. If the channel is rapidly pressurized, and pressure is focused within this layer, then the 2-D analytical model may be a sufficient characterization of subsurface deformation for instrument siting. This analysis is orders of magnitude faster than the numerical solution of fully coupled, 3-D poroelastic problems.

Utilizing analytical, closed-form solutions whenever possible will provide a fast preliminary analysis. This may limit the use of slower numerical models to the inverse analysis of field measurements. Inverse analysis of heterogeneous, 3-D structures requires the best available computer resources and large computation times. Nevertheless, analytical solutions are able to considerably narrow down the parametric space, so that the fully-coupled transient solutions will only be needed in a few instances.

During transient models of injection, the pattern of deformation evolves as the pressurized region expands from the injection well. In the reservoir, the formation compresses radially and expands vertically and circumferentially in advance of the pressure front. Therefore, radial strain could be an indicator of the pressure front within the reservoir [*Murdoch et al.*, 2016]. Interestingly, this effect also occurs in the confining unit, with compressive radial strains and tensile circumferential strain occurring in advance of the underlying reservoir pressure front. This suggests the pressure distribution at depth may be interpreted using normal strains in confining units. In general, signals decreases towards the surface, however they remain on the order of 0.1 με, well above the resolution of borehole strainmeters.

The primary objective of this work was to identify a zone of greatest deformation that is optimal for strainmeter deployment during water injection at the North Avant field. The function δ is composed of components of strain and tilt directly measureable with portable borehole strainmeters [e.g., *Hisz et al.*, 2013; *DeWolf et al.*, 2015]. The analysis indicates that monitoring instruments at the North Avant field should be located at a radial distance between 500 ft and

1000 ft from the well and at depths above 200 ft or below 450 ft. Maximum deformation signal is predicted to lie within this range for at least 100 days of continuous injection.

The function δ is composed of three distinct measurements with a well-defined local minimum. This signal is easily distinguishable on plots and allows for clear understanding of the depth to avoid. If one of the signals is removed, then the curve becomes smoother. For example, we remove the tilt from the function in Figure 2.18b. The resulting signal remains a quadratic

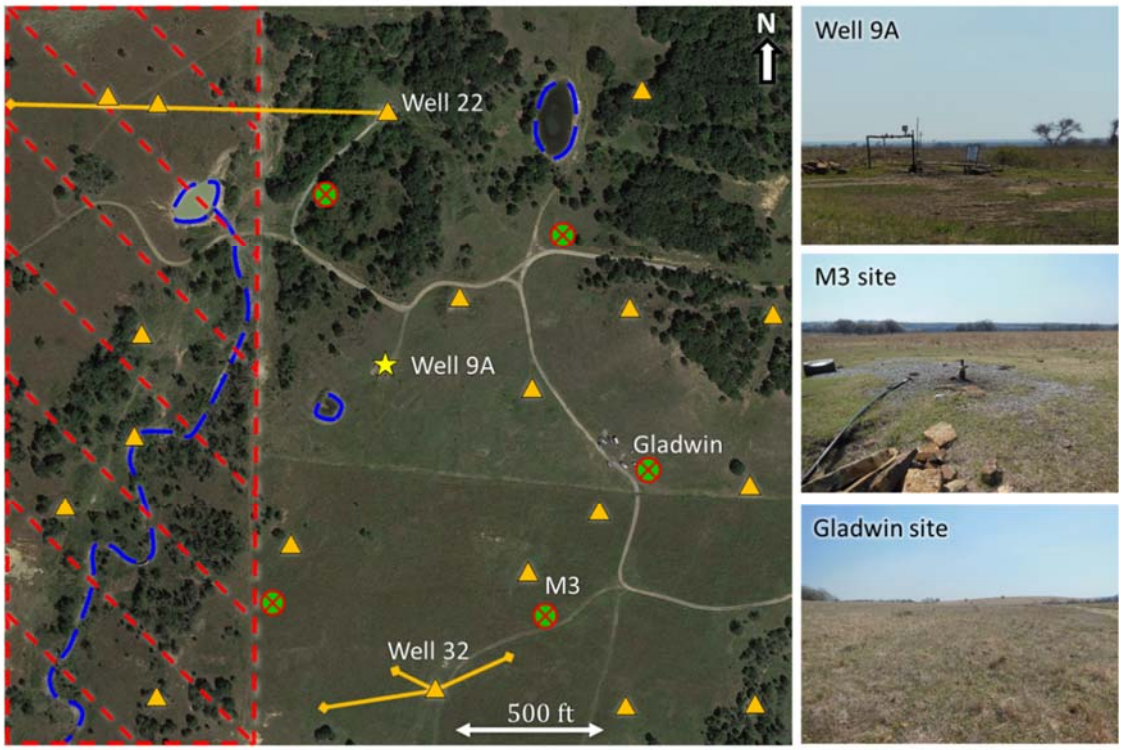

Figure 2.31. Plan view of the injection test site at the North Avant field in in the northwest quadrant of section 25, T23N, R12E. Surface water features (blue dashed lines) lie in the vicinity of well 9A (yellow star). Tucker Creek flows north to south in an area (red slashed zone) that is unavailable to field testing. Orange triangles (lines for horizontal wells) are locations of existing wells, and green and red crosshairs are proposed monitoring sites. The wellhead shown at M3 is one of several abandoned wells in the vicinity not used for multiple years that may or may not be refitted for monitoring instruments.

function with identical focal point, however, the curve is much less pronounced and less distinguishable. In particular, the modified function suggests a significantly lower signal at very shallow depths. This may result in instruments being placed below the focal point, at significantly greater expenditure.

It would be best to place the instrument near the surface, where the signals increase near the free surface. This may prove problematic due to weathering (i.e. fracturing and chemical alteration), ground water or temperature fluctuations, and surface features (i.e., topography). The depth where these effects become negligible will depend on the local conditions, and at the North Avant field, they will likely diminish significantly below a 100 ft depth. For this reason, we suggest deploying the instruments at depths between 100 and 150 ft, however, factors such as access to the location and proximity to surface features will determine specific locations of monitoring wells.

The field test of water injection at the North Avant field is an analog to carbon storage. The injection process will occur at a somewhat shallower depth and pressure; however, the physics governing the processes are the same and reservoirs similar to the Bartlesville sandstone are being considered for carbon storage. The minimum depth of current test sites of CO_2 injection are at depths exceeding 2500 ft [e.g., *Förster et al.*, 2006], which corresponds to the minimum depth necessary to store supercritical CO_2 [*Lin and Ray*, 1994; *Shafeen et al.*, 2004; *Svenson et al.*, 2007]. In Appendix A.2, we confirmed our modeling procedure with the work of *Murdoch* [2014] for injection at half the rate into a reservoir at more than double the depth. Deformation occurs in a similar pattern and values remain on the order of 0.1 to 1 $\mu\varepsilon$.

Instruments must be installed directly within formations to measure strains. Coupling to the soft or damaged materials, like shale, may be difficult and result in a decreased signal. In contrast, limestone is stiff and forms good material for coupling to the instrument. A limestone layer injects shales at a depth of 96 ft in the vicinity of well 9A. Therefore, a monitoring well was drilled at (36.53212, -96.081021) (Figure 2.31) and a Gladwin Tensor Strainmeter [*Gladwin and Hart*, 1985] was grouted into the limestone. It is currently operational, and strainmeter data are available at *UNAVCO* [2017]. Monitoring well M3 was drilled to a depth of 240 ft, where another limestone facies is present. This well contains the [*DeWolf et al.*, 2015]. Piezometers will be installed in abandoned wells, and a combination meteorological station (Vaisala WXT520) will be deployed on site to measure barometric pressure, air temperature, rainfall, wind speed and direction.

Well 9A was chosen as the injection site to minimize the effect of topography. The relief in the vicinity of the injection site is 160 ft relief across 2000 ft from the hill to the east to the drainage basin in the west. All models maintain a smooth topography. If a feature (i.e. hill or valley) with 100 ft vertical relief over 600 ft from the injection site is included in the axisymmetric

model, then strains will differ by over 10% at depths of 150 ft and horizontal distances of hundreds of feet (Appendix A.7). Once depths greater than 800 ft are reached, all differences in deformation virtually disappear (Figure A.15). Radially, the signal is no longer parabolic and δ is dampened below the hill (Figure 2.32).

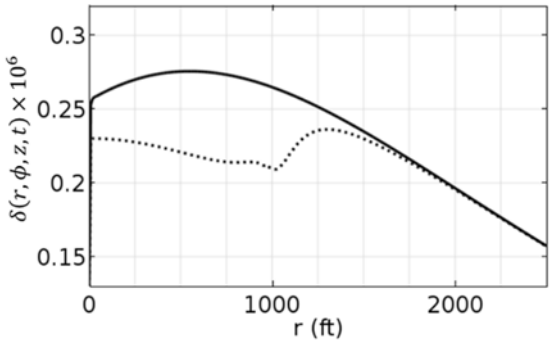

Figure 2.32. The function δ at a depth of 150 ft after 10 days for the benchmark axisymmetric model of a flat upper surface (solid line) and hill above the injection well (dotted line). See Appendix A.7 for model details.

2.7.2. Effects of stratigraphic column

Our modeling has assumed the overburden and basement layers of models consist of homogeneous and uniform properties, however, the subsurface of the North Avant field consists of stratigraphic layers of sedimentary rocks with different properties that may affect the strain. During the drilling of monitoring wells, a competent limestone layer was intersected at a depth of 100 ft. Instruments were installed within this layer, which is expected to be stiffer than other strata within the sequence.

To investigate the effect of the limestone formation, we modified the benchmark model (Figure 2.16) to include a layer 20 feet thick at a depth of 100 ft. This layer is stiffer than the enveloping strata, with mechanical properties: ρ = 2700 kg/m^3, E = 50 GPa, ν = 0.3. In general, the deformation during injection is consistent with the induced deformation during the benchmark case. Lateral strains are not altered at a scale noticeable in Figure 2.33. The vertical strain ε_z is consistent with the benchmark for greater depths. Towards the surface, ε_z decreases at shallower depths approaching the stiff layer. The maximum deviation from the benchmark model, approximately 10% at a radial distance of 500 ft and after 10 days, occurs within the stiff layer. At

the upper boundary of the stiff layer, the difference decreases and ε_z remains less than 5% than the benchmark case.

At depths less than the stiff layer, the tilt ω_{rz} is consistent with the benchmark case at the scale of Figure 2.33. The upper boundary coincides with a jump in tilt that exceeds 50% the tilt in benchmark case at a radius of 500 ft after 10 days. The difference in the tilts decreases at greater depths, nevertheless, the inclusion of the stiff layer causes the reversal in tilt to occur at depths tens of feet less than in the benchmark case and tilts still differ by 5 to 10% at a depth of 1000 ft.

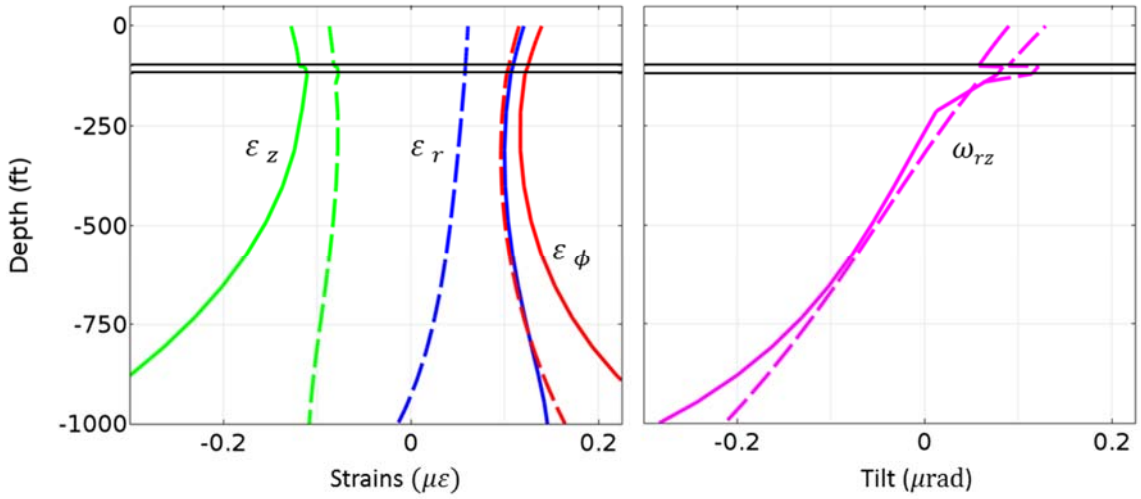

Figure 2.33. Profiles of strains and tilts after 10 days of injection at distances of *r* = 500 ft (solid lines) and *r* = 1000 ft (dashed lines). A stiffer layer lies between the horizontal solid black lines.

The dependence of deformation on the mechanical properties of the subsurface can is better illustrated by varying one parameter throughout the confining units. We demonstrate this effect by varying the Young's Modulus of the strata that envelops the reservoir as a periodically with depth (Figure 2.34). The period is approximately 200 ft and the amplitude is 10 GPa, while the average *E* = 15 GPa. Changes to the deformation occur at the same period as *E*(*z*) and are also correspond to deviations in the profile of pressure. All variations in the deformation are less the strength of the signals. The amplitude of the deformation increases with depth lateral strain decrease from the benchmark model, however, the average vertical strain and tilt remain comparable to the benchmark model.

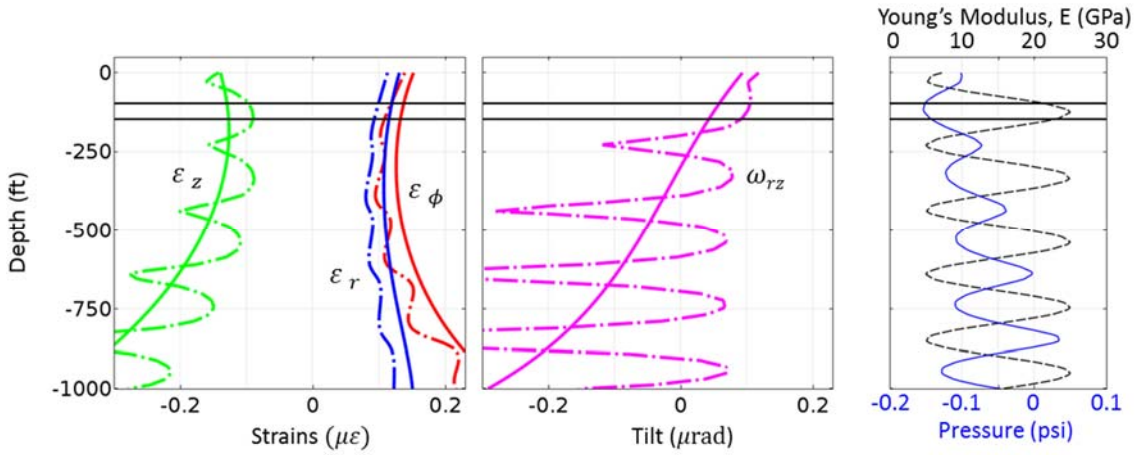

Figure 2.34. Profiles of strains and tilts after 10 days of injection at distances of *r* = 500 ft. Solid lines denote the deformation in the benchmark case, while dash-dot lines are the deformation when Young's Modulus is a function of depth. In this case, the horizontal solid lines denote the area of minimum deformation strength.

2.7.3. Characterization of highly permeable channels

Heterogeneities are expected within sedimentary formations, and will result in anomalies to the deformation pattern on the scale of the deformation due to pumping [e.g., *Fabian and Kümpel*, 2003; *Urlaub and Fabian*, 2011]. Heterogeneous reservoir permeabilities are common within lithified fluvial deposits [*Slatt*, 2006]. Including the high energy channels at the base of the Bartlesville sandstone in models suggests deformation at shallow depths reflects the pressure distribution in the underlying reservoir (section 2.6). Deformation signals are amplified in areas overlying permeability boundaries. In particular, strains are greatest over the high energy channel and tilt signals are greatest just outside of the high energy channel. Hence, an array of instruments may be able to capture heterogeneities within the field.

The ability to identify channels of high permeability has important implications for fluid injection operations. During oil production, channels act as preferential pathways and fluids collect within these channels, which affects the location of future pumping wells. At the North Avant field, the high energy channels of greater permeability within the Bartlesville sandstone are the most prominent heterogeneity. Monitoring wells in the vicinity of well 9A will be spatially distributed to intersect the high energy channel at different thicknesses. Characterizing high-permeability regions during CO_2 storage is also important because of their greater storage capacity.

2.7.4. Constant injection pressure or constant injection rate

In sustained operations, injection rate is typically controlled and the resulting wellhead pressure is monitored. Long-term injection may operate at a constant rate at early times, but as the formation pressure increases, wells operate at a relatively constant pressure. This is done in order to avoid exceeding pore pressures that damage the formation or result in wellbore instability. This typically results in a pulsating flow rate.

In our modeling, strain increase is directly proportional to the pressure change as poroelastic properties are independent of the fluid pressure. This isolates the strain dependency on resulting pressure changes within a reservoir. Effects due to such phenomena as tidal forces and barometric pressure were ignored to focus purely on the response due to injection. These forces can be removed from field data using additional measurements at the site.

The field data at well 9A (Figure 2.6) suggests a constant injection rate results in a relatively constant pressure on the scale of tens of days. The approximate rate of 500 barrels per day is expected to result in a bottomhole pressure of 300 psi. Using this field data, we tested how the reservoir permeability affects pressure and deformation for the cases of constant injection rate versus constant injection pressure (Appendix A.6). Keeping all other formation properties constant within the two cases, a permeability of 12 mD results in a reservoir pressure that is equal at approximately 3 days. This is consistent with the permeability measurements in section 2.3.5. Prior to this time, the pressure is greater for the case of constant injection pressure. After 100 days, the constant rate condition results in reservoir pressures that are approximately 20% higher. The difference in deformation is less than 0.1 $\mu\varepsilon$ and μrad for depths less than 700 ft for the first 100 days. Nevertheless, changes in wellhead pressure are known during injection and can be incorporated in to any inverse analysis.

2.7.5. Effect of casing

The wellbore is incorporated into the geometry of axisymmetric models, however, 3-D models assume pressure is maintained along a linesource and the wellbore is removed from modeling. All models impose pressure along an injection line and neglect the effect of the wellbore casing and screen on deformation. In Appendix A.5, we test the effect of the casing and screen on the deformation pattern.

Changes to the deformation pattern are most prominent adjacent to the wellbore and at early times. Excluding the casing and screen generally results in more undulated curves near the casing, and in some cases, results in a reversal of signal (Figure A.12). Vertical strains match at all times and locations, however the roller-type boundary results in local differences in strain at the wellbore. Nevertheless, these differences decrease away from the well such that strains in the two cases of boundary conditions converge to the same values at all depths for radii greater than approximately 100 ft. This distance is much greater than that of monitoring wells to the injection well during the proposed field test, so we simplified the geometry of our models to exclude casing or screens.

2.8. Conclusion

We analyzed data in literature, in the reports of our industrial partner, Grand Directions, and from field reconnaissance to develop a conceptual model of the reservoir at the North Avant field. The reservoir was divided into a continuous homogenous unit, or C zone, of the Bartlesville sandstone underlain locally by elongated channels of higher permeability. The higher permeability of the channels is the result of coarse sands deposited in a high energy environment. The conceptual model of the North Avant field was the basis for the mathematical models presented in this work.

We presented the analytical solution in both 2-D and 3-D of deformation induced by pressurized inclusions in an infinite half-space. These models show the principle of monitoring deformation to interpret the pressure increase in a reservoir. The strain tensor is distinctive and forms a characteristic signature from pressurized geometries representative of injection into reservoirs. Strains and tilts are measurable up to the ground surface, suggesting it is feasible to use measurements of deformation in shallow boreholes. A function was introduced to determine the range of greatest deformation signal. This correspond to the target depth of strainmeter deployment. The function has a distinct minimum at a depth of several hundred feet, which suggests there may be a range of depths that are best Multiple components of strain are more effective than single components, or pressure signals, at constraining pressurized geometries.

More realistic transient simulations of an injection process were modeled numerically. These models are consistent with the deformation in the analytical solutions and show the evolution of the deformation pattern due to fluid injection may be used to monitor fluid injection

processes. A benchmark axisymmetric model is representative of the most idealized conditions possible at a planned water injection test at the North Avant field, Osage County, Ok. Our results suggest a range of $z \leq 200$ ft or $z \geq 450$ ft for instrument deployment. Laterally, instruments should be installed away from the wellbore to register tilt signals, but within 1000 ft to measure strains. If fluid is injected at a rate of 300 psi into the Bartlesville sandstone, the resulting deformation is on the order of 1×10^{-7}. From this analysis, two monitoring wells have been drilled at the North Avant field in preparation of a field demonstration, with more scheduled for drilling.

We developed a 3-D model of injection into a reservoir to determine the effect of heterogeneous permeability distribution on the deformation pattern. Permeability boundaries result in an increase of deformation compared to the benchmark model that is most prominent near lateral permeability boundaries. When injection occurs at a well intersecting the high energy channels, strains in the shallow subsurface increase over the channel. Adjacent to the channel, strains decrease, but vertical tilts increase perpendicular to boundaries in the direction of the component of tilt. This suggests that a spatial array of measurements of the strain tensor can characterize the high energy channels. This result holds important implications for identifying the signals of additional heterogeneities.

2.9. References

Amy, L. A., S. A. Peachey, A. R. Gardiner, G. E. Pickup, E. Mackay, and K. D. Stephen (2013), Recovery efficiency from a turbidite sheet system: numerical simulation of waterflooding using outcrop-based geological models, *Pet. Geosci.*, *19*, 123–138, doi:10.1144/petgeo2011-041.

Andrews, R. D. (1997), Fluvial-Dominated Deltaic (FDD) Oil Reservoirs in Oklahoma: The Bartlesville Play (Special Publication 97-6, ISSN: 0275-0929), *Ok. Geol. Survey*, Norman, Oklahoma.

Barwis, J., J. McPherson, and J. R. J. Studlick (Eds.) (2012), *Sandstone Petroleum Reservoirs*, Springer Science & Business Media, New York, USA.

Bass, N. W. (1934), Origin of Bartlesville Shoestring Sands, Greenwood and Butler Counties, Kansas, *Am. Assoc. Pet. Geol. Bull.*, *18*, doi:10.1306/3D932C7A-16B1-11D7-8645000102C1865D.

Bass, N. W. (1942), *Subsurface geology and oil and gas resources of Osage County, Oklahoma, Part II. Summary of subsurface geology with special reference to oil and gas*, Washington, D.C.

Berryman, J. G. (1995), Mixture Theories for Rock Properties, in *Rock Physics and Phase Relations: A handbook of Physical Constants*, edited by T. J. Ahrens, p. 236, AGU, Washington, D.C.

Biot, M. A. (1941), General Theory of Three-Dimensional Consolidation, J. Appl. Phys., 12(2), 155–164, doi:10.1063/1.1712886.

Biot, M. A. (1955), Theory of Elasticity and Consolidation for a Porous Anisotropic Solid, J. Appl. Phys., 26(2), 182–185, doi:10.1063/1.1721956.

Biot, M. A., and D. G. Willis (1957), The elastic coefficients of the theory of consolidation, J. Appl. Mech., 24, 594–601.

Buckley, S. E., and M. C. Leverett (1942), Mechanism of fluid displacement in sands, *Trans. AIME*, *146*(1), 107–116, doi:10.2118/942107-G.

Cappa, F., and J. Rutqvist (2011), Impact of CO_2 geological sequestration on the nucleation of earthquakes, *Geophys. Res. Lett.*, *38*(17), 2–7, doi:10.1029/2011GL048487.

Carroll, H. B., and G. Guo (1999), A new methodology for oil and gas exploration using remote sensing data and surface fracture analysis (DE-AC22-94PC91008), *U.S. Dept. of Energy.* Tulsa, OK.

Chadwick, R. ., P. Zweigel, U. Gregersen, G. . Kirby, S. Holloway, and P. Johannessen (2004), Geological reservoir characterization of a CO_2 storage site: The Utsira Sand, Sleipner, northern North Sea, *Energy*, *29*(9–10), 1371–1381, doi:10.1016/j.energy.2004.03.071.

Chen, Z. R. (2011), Poroelastic model for induced stresses and deformations in hydrocarbon and geothermal reservoirs, *J. Pet. Sci. Eng.*, *80*(1), 41–52, doi:10.1016/j.petrol.2011.10.004.

Chiaramonte, L., M. D. Zoback, J. Friedmann, and V. Stamp (2008), Seal integrity and feasibility of CO_2 sequestration in the Teapot Dome EOR pilot: Geomechanical site characterization, *Environ. Geol.*, *54*(8), 1667–1675, doi:10.1007/s00254-007-0948-7.

Crow, W., J. W. Carey, S. Gasda, D. Brian Williams, and M. Celia (2010), Wellbore integrity analysis of a natural CO_2 producer, *Int. J. Greenh. Gas Control*, *4*(2), 186–197, doi:10.1016/j.ijggc.2009.10.010.

D. R. Kerr, L. A. J. (1990), Fluvial architecture and reservoir compartmentalization in the Oligocene Middle Frio Formation of South Texas, *Am. Assoc. Pet. Geol. Bull.*, *74*, 373–380, doi:10.1306/20B2311F-170D-11D7-8645000102C1865D.

Dauben, D. (2013), Simulation of performance in the Wolco area, Avant Field, Osage County, Oklahoma, *Dauben International Energy Consult.* Tulsa, OK.

Davies, J. H. (2003), Elastic Field in a Semi-Infinite Solid due to Thermal Expansion or a Coherently Misfitting Inclusion, *J. Appl. Mech.*, *70*(5), 655, doi:10.1115/1.1602481.

Davis, E. J. (2011), Interpretation of CO_2 sequestration-induced surface deformation over KB-502 at Krechba, Algeria, in *SPE Annual Technical Conference and Exhibition*, Society of Petroleum Engineers, Denver, CO.

Davis, S. N., F. L. Peterson, and A. D. Halderman (1969), Measurement of small surface displacements induced by fluid flow, *Water Resour. Res.*, *5*(1), 129–138, doi:10.1029/WR005i001p00129.

Detournay, E., and A. Cheng (1993), Fundamentals of poroelasticity, in *Comprehensive Rock Engineering: Principles, Practice and Projects*, vol. II, pp. 113–171.

DeWolf, S., L. C. Murdoch, S. Moysey, L. N. Germanovich, A. Hanna, and J. E. Smith (2015), Removable tensor strainmeter and vector tiltmeter system for use with forward and inverse methods for characterizing deformation during CO_2 injection, in *2015 AGU Fall Meeting*, San Fransisco, CA.

Tiab, D. and E. C. Donaldson (1996) Petrophysics. Theory and practice of measuring reservoir rock and fluid transport properties. Gulf Publishing, Houston.

Dusseault, M., M. Bruno, and J. Barrera (1998), Casing shear: causes, cases, cures, in *Proceedings of SPE International Oil and Gas Conference and Exhibition in China*, Society of Petroleum Engineers.

Fabian, M., and H. J. Kümpel (2003), Poroelasticity: Observations of anomalous near surface tilt induced by ground water pumping, *J. Hydrol.*, *281*, 187–205, doi:10.1016/S0022-1694(03)00234-8.

Förster, A. et al. (2006), Baseline characterization of the CO_2SINK geological storage site at Ketzin, Germany, *Environ. Geosci.*, *13*(3), 145–161, doi:10.1306/eg.02080605016.

Franks, K. A. (1989), *The Osage Oil Boom*, Oklahoma Heritage Association; Western Heritage books.

Gale, J. E. (1975), A numerical, field and laboratory study of flow in rocks with deformable fractures (Doctoral dissertation), University of California, Berkeley.

Garagash, D. I., and L. N. Germanovich (2012), Nucleation and arrest of dynamic slip on a pressurized fault, *J. Geophys. Res. Solid Earth*, *117*(B10), 1–27, doi:10.1029/2012JB009209.

Geertsma, J. (1966), Problems of rock mechanics In petroleum production engineering, in *1st ISRM Congress*, pp. 585–594, Lisbon, Portugal.

Germanovich, L. N., and R. A. Chanpura (2002), Modeling thin inclusions in poroelastic medium by line discontinuities, in *IUTAM Symposium on Analytical and Computational Fracture Mechanics of Non-Homogeneous Materials*, edited by B. L. Karihaloo, pp. 133–142, Springer-Science+Business Media, B.V., Cardiff, U.K.

Germanovich, L. N., G. Genc, R. P. Lowell, and P. A. Rona (2012), Deformation and surface uplift associated with serpentinization at mid-ocean ridges and subduction zones, *J. Geophys. Res. Solid Earth*, *117*(7), 1–23, doi:10.1029/2012JB009372.

Germanovich, L. N. (May 2017), Private communication.

Germanovich, L.N. and M. Robinowitz (April 2017), Private communication.

Gladwin, M. T. (1984), High-precision multicomponent borehole deformation monitoring, *Rev. Sci. Instrum.*, *55*(12), 2011–2016, doi:10.1063/1.1137704.

Gladwin, M. T., and R. Hart (1985), Design parameters for borehole strain instrumentation, *Pure Appl. Geophys. PAGEOPH*, *123*(1), 59–80, doi:10.1007/BF00877049.

Guido, F. L., M. Antonellini, and V. Picotti (2015), Modeling ground displacement above reservoirs undergoing fluid withdrawal/injection based on an ellipsoidal inhomogeneity model, *Int. J. Rock Mech. Min. Sci.*, *79*, 63–69, doi:10.1016/j.ijrmms.2015.08.010.

Hesse, M. A., and G. Stadler (2014), Joint inversion in coupled quasi-static poroelasticity, *J. Geophys. Res. Solid Earth*, *119*(2), 1425–1445, doi:10.1002/2013JB010272.

Hisz, D. B., L. C. Murdoch, and L. N. Germanovich (2013), A portable borehole extensometer and tiltmeter for characterizing aquifers, *Water Resour. Res.*, *49*(12), 7900–7910, doi:10.1002/wrcr.20500.

Holzbecher, E., and G. U. Göttingen (2013), Poroelasticity benchmarking for FEM on analytical solutions, *COMSOL Conf.*, (1), 1–7.

Hudson, M. R., D. V. Smith, M. P. Pantea, and C. J. Becker (2016), *Geologic and geophysical models for Osage County , Oklahoma , with implications for groundwater resources: Scientific investigations report 2016 – 5067*, Reston, VA.

Iglesias, M. A., and D. McLaughlin (2012), Data inversion in coupled subsurface flow and geomechanics models, *Inverse Probl.*, *28*(11), 115009, doi:10.1088/0266-5611/28/11/115009.

IPCC (2005), *IPCC Special Report on Carbon Dioxide Capture and Storage*, edited by B. Metz, O. Davidson, H. C. de Coninck, M. Loos, and L. A. Meyer, Cambridge University Press, New York, USA.

Itasca (1997), *FLAC 3D, Fast Lagrangian Analysis of Continua in 3 Dimensions. Version 2.0.*, Minneapolis, Minnesota.

Jordan, L. (1957), *Subsurface stratigraphic names of Oklahoma*, Norman, OK.

Kennedy, L. E., J. D. McClure, H. D. Jenkins, and N. W. Bass (1942), *Part 4. Townships 24 and 25 North Ranges 10 and 11 East: Bulletin 900-D*, Washington, D.C.

Kerr, D. R. (2007), *Facies architexture of the Bartlesville interval in North Avant field, Osage County, Oklahoma*, Tulsa, OK.

Lin, P., and T. G. Ray (1994), A New Method for Direct Measurement of In-Situ Stress Directions and Formation Rock Properties, *J. Pet. Technol.*, *46*(3), 249–254, doi:10.2118/26600-PA.

Liu, G. (2012), Carbon dioxide geological storage: Monitoring technologies review, in *Greenhouse Gases - Capturing, Utilization and Reduction*, pp. 299–338, InTech.

Martin, C. D., C. C. Davison, and E. T. Kozak (1991), Characterizing normal stiffness and hydraulic conductivity of a major shear zone in granite, in *International Journal of Rock Mechanics and Mining Sciences & Geomechanics Abstracts*, vol. 28, pp. 549–556.

Moeck, I., G. Kwiatek, and G. Zimmermann (2009), Slip tendency analysis, fault reactivation potential and induced seismicity in a deep geothermal reservoir, *J. Struct. Geol.*, *31*(10), 1174–1182, doi:10.1016/j.jsg.2009.06.012.

Mura, T. (1982), *Micromechanics of defects in solids*, Springer Netherlands, Dordrecht.

Murdoch, L. C. (2014), Characterizing and interpreting the in situ strain tensor during CO_2 injection (DE-FOA-0001037), *U.S. Dept. of Energy*. Clemson, SC.

Murdoch, L. C., and L. N. Germanovich (2012), Storage change in a flat-lying fracture during well tests, *Water Resour. Res.*, *48*(12), n/a-n/a, doi:10.1029/2011WR011571.

Murdoch, L. C., S. Moysey, and L. N. Germanovich (2016), Proof-of-feasibility of using well bore deformation as a diagnostic tool to improve CO_2 sequestration (DE FE0004542), *U.S. Dept. of Energy*. Clemson, SC.

Muskhelishvili, N. I. (1977), *Some Basic Problems of the Mathematical Theory of Elasticity*, Springer Netherlands, Dordrecht.

Northcutt, R. A. (1997), Fluvial-dominated deltaic (FDD) oil reservoirs in Oklahoma: The Bartlesville play (Special Publication 97-6, ISSN: 0275-0929), *OK Geol. Survey,* Norman, OK.

Obianyor, E. T. (2008), Permeability anisotropy related to meandering fluvial facies architextural elements in the Bartlesville sandstone of North Avant field Osage County, Oklahoma (Masters Thesis), University of Tulsa.

Palciauskas, V. V., and P. A. Domenico (1989), Fluid pressures in deforming porous rocks, *Water Resour. Res.*, *25*(2), 203–213, doi:10.1029/WR025i002p00203.

Peng, S., and J. Zhang (1985), Rock strength experiments and failure criteria, in *Engineering Geology for Underground Rocks*, pp. 75–100, Springer Berlin Heidelberg, Berlin, Heidelberg.

PTC (2007), Mathcad 14.0 user's guide, Parametric Technology Corporation, Needham, MA.

Rees, F. B. (1972), Methods of mapping and illustrating stratigraphic traps: Geologic exploration methods, in *M 16: Stratigraphic Oil and Gas Fields--Classification, Exploration Methods, and Case Histories*, pp. 168–221.

Rice, J. R., and M. P. Cleary (1976), Some basic stress diffusion solutions for fluid-saturated elastic porous media with compressible constituents, *Rev. Geophys.*, *14*(2), 227, doi:10.1029/RG014i002p00227.

Riddiford, F., A. Tourqui, C. Bishop, B. Taylor, and M. Smith (2003), A cleaner development in the Salah Gas Project, Algeria, in *Greenhouse Gas Control Technologies - 6th International Conference*, pp. 595–600, Elsevier.

Robinowitz, S., D. Dauben, and J. Schmeling (2006), Enhanced oil recovery by horizontal waterflooding (DE-FG26-02NT15452), *Dept. of Energy.* Tulsa, OK.

Rutqvist, J., J. T. Birkholzer, and C.-F. Tsang (2008), Coupled reservoir–geomechanical analysis of the potential for tensile and shear failure associated with CO_2 injection in multilayered reservoir–caprock systems, *Int. J. Rock Mech. Min. Sci.*, *45*(2), 132–143, doi:10.1016/j.ijrmms.2007.04.006.

Schmeling, J. (2016), Private communication.

Schweisinger, T., E. J. Svenson, and L. C. Murdoch (2011), Hydromechanical behavior during constant-rate pumping tests in fractured gneiss, *Hydrogeol. J.*, *19*(5), 963–980, doi:10.1007/s10040-011-0728-z.

Segall, P., and S. D. Fitzgerald (1998), A note on induced stress changes in hydrocarbon and geothermal reservoirs, *Tectonophysics*, *289*(1–3), 117–128, doi:10.1016/S0040-1951(97)00311-9.

Segall, P., J.-R. Grasso, and A. Mossop (1994), Poroelastic stressing and induced seismicity near the Lacq gas field, southwestern France, *J. Geophys. Res.*, *99*(B8), 15423, doi:10.1029/94JB00989.

Shafeen, A., E. Croiset, P. L. Douglas, and I. Chatzis (2004), CO_2 sequestration in Ontario, Canada. Part I: Storage evaluation of potential reservoirs, *Energy Convers. Manag.*, *45*(17), 2645–2659, doi:10.1016/j.enconman.2003.12.003.

SIMULIA (2015), *Reservoir geomechnics: How reservoir geomechanics is being addressed by SIMULIA*, Dassault Systemes Simulia Corporation. Johnston, RI.

Slatt, R. M. (2006), Fluvial deposits and reservoirs, in *Handbook of Petroleum Exploration and Production*, pp. 203–248.

Suckale, J. (2009), Induced seismicity in hydrocarbon fields, in *Advances in Geophysics*, vol. 51, pp. 55–106.

Svenson, E., T. Schweisinger, and L. C. Murdoch (2007), Analysis of the hydromechanical behavior of a flat-lying fracture during a slug test, *J. Hydrol.*, *347*(1–2), 35–47, doi:10.1016/j.jhydrol.2007.08.020.

Tamimi, N., and T. L. Davis (2012), Imaging the Morrow A Sandstone using shear wave VSP data, Postle Field, Oklahoma, *Int. J. Geophys.*, *2012*, 1–14, doi:10.1155/2012/231256.

Temizel, C., D. Thanon, T. Inceisci, K. Balaji, A. Suhag, R. Ranjith, Z. Wijaya, and E. Abdelfatah (2017), An analysis of scale buildup in seawater injection of waterflooding operations, in *SPE Latin America and Caribbean Mature Fields Symposium*, Society of Petroleum Engineers.

Thompson, P. M., and E. T. Kozak (1991), In situ measurement of coupled hydraulic pressure/fracture dilation in stiff crystalline rock, in *3rd International Symposium on Field Measurements in Geomechanics*, vol. 30, p. A157, Oslo.

UNAVCO (2017), UNACVO, Available from: http://pbo.unavco.org/data/bsm/plots/AVN2

Urlaub, M., and M. Fabian (2011), Poroelasticity: Finite element modelling of anomalous tilt and pore pressure caused by pumping in a sedimentary half space with fault, *J. Geodyn.*, *51*(4), 219–232, doi:10.1016/j.jog.2010.09.001.

Vasco, D. W., K. Karasaki, and K. Kishida (2001), A coupled inversion of pressure and surface displacement, *Water Resour. Res.*, *37*(12), 3071–3089, doi:10.1029/2001WR000391.

Vasco, D. W., A. Rucci, A. Ferretti, F. Novali, R. C. Bissell, P. S. Ringrose, A. S. Mathieson, and I. W. Wright (2010), Satellite-based measurements of surface deformation reveal fluid flow associated with the geological storage of carbon dioxide, *Geophys. Res. Lett.*, *37*(3), 1–5, doi:10.1029/2009GL041544.

Vaughn, E. C., J. M. Fulford, and H. R. Myers (2006), Bucket wheel assembly for fluid flow meters (US 7,017,425 B1), *United States Patent*.

Verdon, J. P., J.-M. Kendall, A. L. Stork, R. A. Chadwick, D. J. White, and R. C. Bissell (2013), Comparison of geomechanical deformation induced by megatonne-scale CO_2 storage at Sleipner, Weyburn, and In Salah., *Proc. Natl. Acad. Sci. U. S. A.*, *110*(30), E2762-71, doi:10.1073/pnas.1302156110.

Wang, H. F. (2000), *Theory of Linear Poroelasticity with Applications to Geomechanics and Hydrogeology*, 1st ed., Princeton University Press.

Ye, L. (Scott), and D. Kerr (2000), Sequence stratigraphy of the middle Pennsylvanian Bartlesville sandstone, Northeastern Oklahoma: A case of an underfilled incised valley, *Am. Assoc. Pet. Geol. Bull.*, *84*(8), 1185–1204, doi:10.1306/A9673C7A-1738-11D7-8645000102C1865D.

Ye, L. S., and K. Yang (1997), Facies architecture of the Bluejacket sandstone in the Eufaula Lake area, Oklahoma: Implications for the reservoir characterization of the Bartlesville sandstone, in *International Reservoir Characterization Technical Conference*, Houston.

APPENDIX

A.1. 2-D analytical solution of pressurized inclusions

In section 2.4.1, we described the 2-D analytical solution of *Germanovich et al.*, [2012] to calculate induced strains from a pressurized region. In this appendix, we use the analytical solution of strain induced by a pressurized inclusion verify boundary conditions in numerical models. The 2-D model consists of an elastic half-space under plain strain conditions. The analytical model is consistent with various known solutions. For example, increasing the reservoir depth, we approach the limit of an inclusion in an infinite space, which constitutes the classic Eshelby problem.

Representing a circle in a half-space as an ellipse with equal semi axes, we compared a 2-D numerical model of a pressurized ellipse to the known solution for a circular, elastic inclusion with transformation strain in an elastic half-space. An ellipse with dimensions $a = 200, b = 20$ m is centered at a depth 600 m (Figure A.1). Elastic properties of the ellipse and enveloping medium were identical: $\mathrm{E} = 10$ GPa, $\nu = 0.25$, and $\alpha = 0.7$. In the numerical model, the inclusion is a highly permeable ($\phi = 0.1$ and $k = 1000$ mD) poroelastic material encased within a non-permeable solid-elastic material. Finite boundaries occur at x = 12 km, y = 6 km. The upper surface is a traction free boundary, and lateral and lower boundaries are assigned roller-type boundary conditions. Displacements across the border of the ellipse are continuous. The ellipse is pressurized to a uniform $P = 1$ MPa.

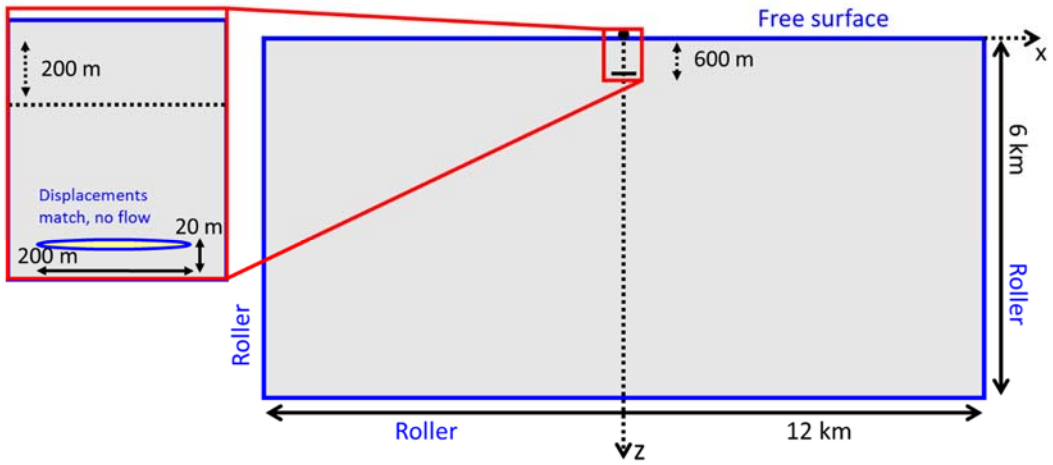

Figure A.1. Geometry of the pressurized elliptical inclusion within a 2-D domain used for the numerical model.

Over sufficient time scales, transient models approach the steady state solution. Pressurizing the inclusion pushes the surface upwards and outwards from the pressurized region. Maximum uplift occurs directly above the inclusion $(4.4\ \mathrm{mm})$ and decreases gradually at greater *x*, such that it is 1.5 mm at distances greater than 500 m away from the origin. Calculated surface uplift error is within 10% of the analytical solution above the inclusion and decreases to 5% at lateral distances of $x = 200$ m, but decreases with increasing mesh density. In general, the horizontal surface displacement error is within 2%.

At a depth of 200 m, the horizontal normal strain $\approx 4\ \mu\varepsilon$, which is double the vertical strain. Both are with 1% of the analytical solution. Maximum tilt and shear strain occurs at lateral distances $\approx 1.5a\ (300\ \mathrm{m})$, where the numerical simulation is nearly an exact match ($< 2\%$ error) to analytical solution.

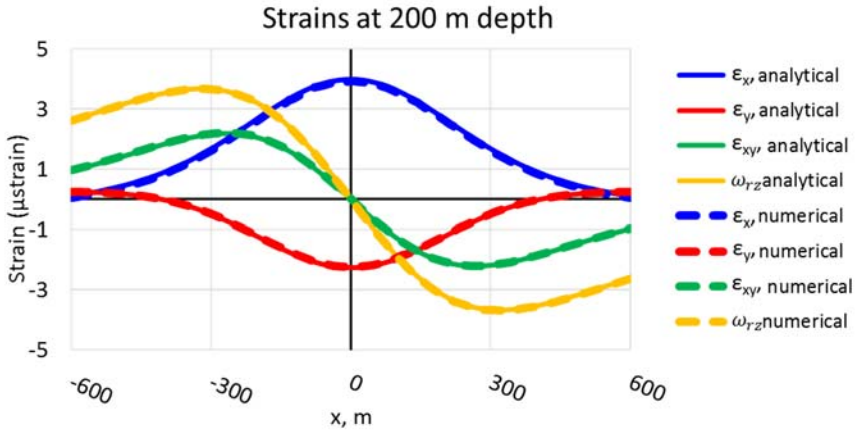

Figure A.2. Plots of strain and tilt $\omega_{xy} = \partial u/\partial y$ are nearly coincident over the entire span. At a depth of 150 ft, the domain is vertical compressed, laterally stretched, and tilts are away from the origin. The results indicate the highest strains occur above the pressurized zone and tilts are at a maximum near the lateral range of the pressurized inclusion.

A.2. Subsurface response to fluid injection at typical carbon storage site

We recreate the model from [*Murdoch et al.*, 2016] to portray the general tendency of the poroelastic response to fluid injection. [*Murdoch et al.*, 2016] investigated typical geologic scenarios of CO_2 storage [e.g., *Riddiford et al.*, 2003; *Chadwick et al.*, 2004; *Chiaramonte et al.*, 2008; *Schweisinger et al.*, 2011] and used intermediate values (Table A.1) to simulate a reservoir 100 m thick imbedded at a $1\ \mathrm{km}$ depth within a $30\ \mathrm{km}$ radial layer (Figure A.3). The well is a cylindrical open hole ($r = 0.1\ \mathrm{m}$) with a casing and screen $8\ \mathrm{mm}$ thick. Axial symmetry is assumed to facilitate more rapid calculations. The reservoir is overlain by a confining layer 1000 m thick and underlain by a $100\ \mathrm{m}$ thick basal unit. Boundary conditions listed in Table 2.4. The wellbore face has a total stress equal to the fluid pressure. Injection at the wellbore is fixed at $p = 1\ \mathrm{MPa}$ for 100 days. Pressures and displacements are determined relative to the initial static equilibrium.

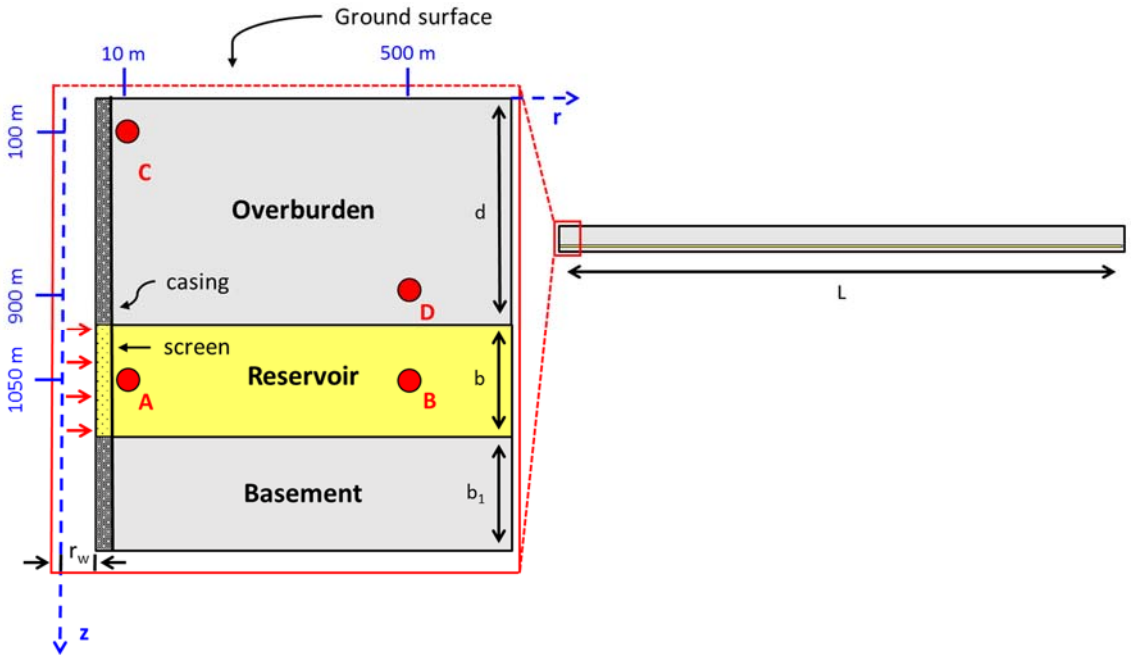

Figure A.3. Cross section of the axisymmetric model with monitoring points marked by red circles. The casing is nearly impermeable steel and injection occurs through a steel screen 8 mm thick. Model dimensions are: r_w = 0.1 m, L = 30 km, d = 1 km, and $b = b_1$ =100 m.

The pattern of deformation evolves as the pressurized region spreads away from the injection line (Figure A.4). The reservoir pressure at a distance $r = 10\ \mathrm{m}$ rapidly increases, reaching nearly 50% of the injection pressure after 1 day (Figure A.6). The rate of increase then slows and the pressure only increases another 10% of the injection pressure over the next 99

days. Reservoir pressure at $r = 500$ m increases steadily to 7% of the injection pressure over 7 days. After this time, the rate of increase drops considerably and reaches a constant pressure 15% of injection pressure at 100 days. This moves the reservoir radially outward in the direction of flow and expands it vertically. Pressure change is much less pronounce in the overburden. Near the wellhead, there is a small pressure drop that decreases steadily to greater than -0.5% of the injection pressure after 100 days. Away from the well and 100 m above the reservoir, the pressure is negative after 1 day. It is -0.05% of the injection pressure, inflects after 10 days and reaches -5% after 100 days. Changes in the pressure manifests as a complex pattern of compressive and tensile strain in the subsurface that expands outward and evolves with time.

Table A.1. Representative formation properties for a depleted reservoir proposed for CO_2 storage [Murdoch et al., 2016].

	$E\ (GPa)$	ν	ϕ	$k\ (mD)$	α	$\rho\ (\mathrm{kg/m^3})$
Reservoir (sandstone)	15	0.25	0.20	100	1	2500
Confining (shale)	15	0.25	0.20	0.1	1	2500
well casing	200	0.3	0.01	0.01	1	2500
well screen	200	0.3	0.2	100	1	2500

During injection, the reservoir expands such that vertical and circumferential strains are always positive (Figure A.4). Vertical strain within the reservoir is up to several times greater than lateral strains and values exceeding 1 με spread radially at approximately the same rate as the pressure front (1% of injection pressure). Circumferential strain is always positive and increases radially at a rate that is between the other normal strains. The radial strain compresses in advance of the pressure front, however, the strain reaches a turning point behind the front such that ε_r becomes increasingly tensile near the well screen. Large values of vertical tilt are concentrated at the upper and lower boundaries of the reservoir. Vertical tilt is negative (towards the wellbore) in the upper reservoir and negative at the near the lower boundary, as the reservoir is dragged outwards. The tilt remains concentrated at the lower boundary, however, the tilt spreads radially along the upper boundary at the pressure front propagates forward.

The volumetric strain rate $(\partial\varepsilon_{vol}/\partial t)$ is always positive, due to the greater values of vertical strain (Figure A.5). Values are greatest in the reservoir decrease towards the surface, and locally increases towards the wellhead. The volumetric strain rate exceeds $1 \times 10^{13} s^{-1}$ about 1 km ahead the pressure front after 1 day. Rates exceeding $1 \times 10^{13} s^{-1}$ gradually expand radially

outward in time such that rates exceed $1 \times 10^{13} s^{-1}$ occur at at the pressure front after 100 days. The vertical strain rate is always positive in the reservoir and greatest near the injection site. Values of vertical strain rate follow directly from the pressure change and the rate decreases locally at the well screen when the pressure change becomes very gradual (after about 100 days). The areal strain rate pattern is similar, however, at early times, it is negative (less than $-1 \times 10^{13}\ 1/\mathrm{s}$) in the reservoir ahead of the pressure front. This reflects the influence of compressive radial strains. Initially, the circumferential strain rate exceeds $1 \times 10^{13}\ 1/s$ ahead of the pressure front. After 100 days, however, the rate decreases and only exceeds $1 \times 10^{13}\ 1/s$ locally in the overburden above the injection line.

Reservoir dilation lifts the overlying confining unit upward, doming the ground surface with a maximum uplift of approximately $1.3\ \mathrm{mm}$ after 100 days of injection. In the subsurface, the zone of induced strains spreads away from the injection site as pressure redistribution occurs in the reservoir. A region of compressive radial strain approximately corresponds to the bulb-like region of tensile vertical strain that extends beyond and above the pressure front. Behind the pressure front, the radial strain expands in the overburden in a bulb-like pattern with its maximum adjacent to the injection site. Strains are greatest in the subsurface adjacent to the pressurized region, yet there is a local maximums of signals near the surface. The vertical strain is compressive throughout the overburden, but increases with depth and becomes tensile near the reservoir as the pressure spreads into the overburden. Circumferential strain is always positive and increases with depth.

In general, tilts are an order of magnitude less than normal strains. The bulging affect due to the upper free surface causes a tilt reversal at shallow depths, roughly twice that of reservoir thickness at the wellbore (Figure A.4). The vertical tilt is negative at depth, but becomes positive near the free surface. Positive tilts (away from the wellbore) emulate as a bulb from the wellhead that increases in time.

In general, strains are characterized by an abrupt change at the start of injection (initial strain is zero), followed by gradual changes after that. Two distinct patterns in strain rates can be distinguished in the cross sections of Figure A.5. There is a bulb-like pattern of positive vertical strain and negative radial strain that expends out ahead of the pressure front in the overburden. The strain rates are greatest at earlier times and decreases to negligible values at radial distances much greater than the radius of the pressure front. Strains above the pressurized region are nearly uniform with a front that increases gradually towards the free surface. Horizontal normal strains

are negative and the vertical strain is positive. The rates exceed $\pm 1 \times 10^{13}\ 1/s$ near the well, but generally decrease as time increases.

A time series of deformation at a point is analogous to in situ measurements. We evaluated strain evolution at two locations in the reservoir depth: point A is near the injection well and point B is away from the injection well, and two in the confining unit: point C is near the wellhead and point D is away from the well at a depth close to the reservoir (Figure A.3). In general, strains correspond to pressures at measurement locations. Vertical strains are compressive or tensile when the pressure is negative or positive, respectively. In all locations, strain rates are greatest within the first day decrease such that 10 days after the injection, the magnitudes of the strain rates decrease to less than $5 \times 10^{13}\ 1/s$ in all monitoring locations. At point A, radial and circumferential strains quickly reach values of 6 and 10 $\mu\varepsilon$ and then gradually increase to 9 and 12 $\mu\varepsilon$, respectively (Figure A.6a). In contrast, the vertical strain nearly triples over the first 30 days from 5 to 13 $\mu\varepsilon$, after which the strain increase nearly ceases. At point B, strains do not exceed $1\ \mu\varepsilon$ until 10 days and circumferential strain never exceeds $2\ \mu\varepsilon$ over the first 100 days. The vertical strain increases as a fractional power function of time to a maximum value of $7\ \mu\varepsilon$ after 100 days. It has a maximum rate after 1 day, when the pressure front reaches point B. Radial strain is initially negative, however, the signal reverses when the pressure front reached point B.

Near the surface (point C), normal strains increase nearly monotonically to approximately $0.7\ \mu\varepsilon$. Vertical strain is always compressive and radial and circumferential strains are expansive. At greater depths in the overburden (point D), the radial strain increases to greater compressive values, reaches a minimum of $-0.2\ \mu\varepsilon$ after 1 day, becomes positive after 10 days to a maximum of $0.2\ \mu\varepsilon$ after 100 days. The vertical strain rate is initially positive, but becomes negative, leading to a minimum of $-0.6\ \mu\varepsilon$ at 20 days. As the pressure front reaches point D, the vertical strain increases, becoming tensile after 40 days.

At all points, the volumetric and areal strains remain positive and mimic the magnitude of the pressure change (Figure A.7). Volumetric strain is always greater than areal strain within the reservoir, due to the relatively high tensile vertical strain. At point D, 100 m above the reservoir, the areal strain is always tensile, reaching $1.8\ \mu\varepsilon$ after 100 days. Volumetric strain is initially less than $0.1\ \mu\varepsilon$, until the pressure front in the reservoir reaches the radius of point D after 15 days causing it to increase monotonically to $3\ \mu\varepsilon$ after 100 days.

Tilts are a function of global deformation. Near the wellbore, tilts are always less than $0.1\ \mu\text{rad}$ as the model is radially symmetric. Tilt is slightly negative ($-0.05\ \mu\text{rad}$) at point A and positive ($0.05\ \mu\varepsilon$)at point C. At a radius of $r = 500\ \text{m}$, tilt is always negative. The signal increases rapidly at first, then the rate decreases after tens of days. The maximum tilt within the reservoir ($-0.07\ \mu\text{rad}$) is roughly half the value 100 m above the revoir ($-0.13\ \mu\text{rad}$).

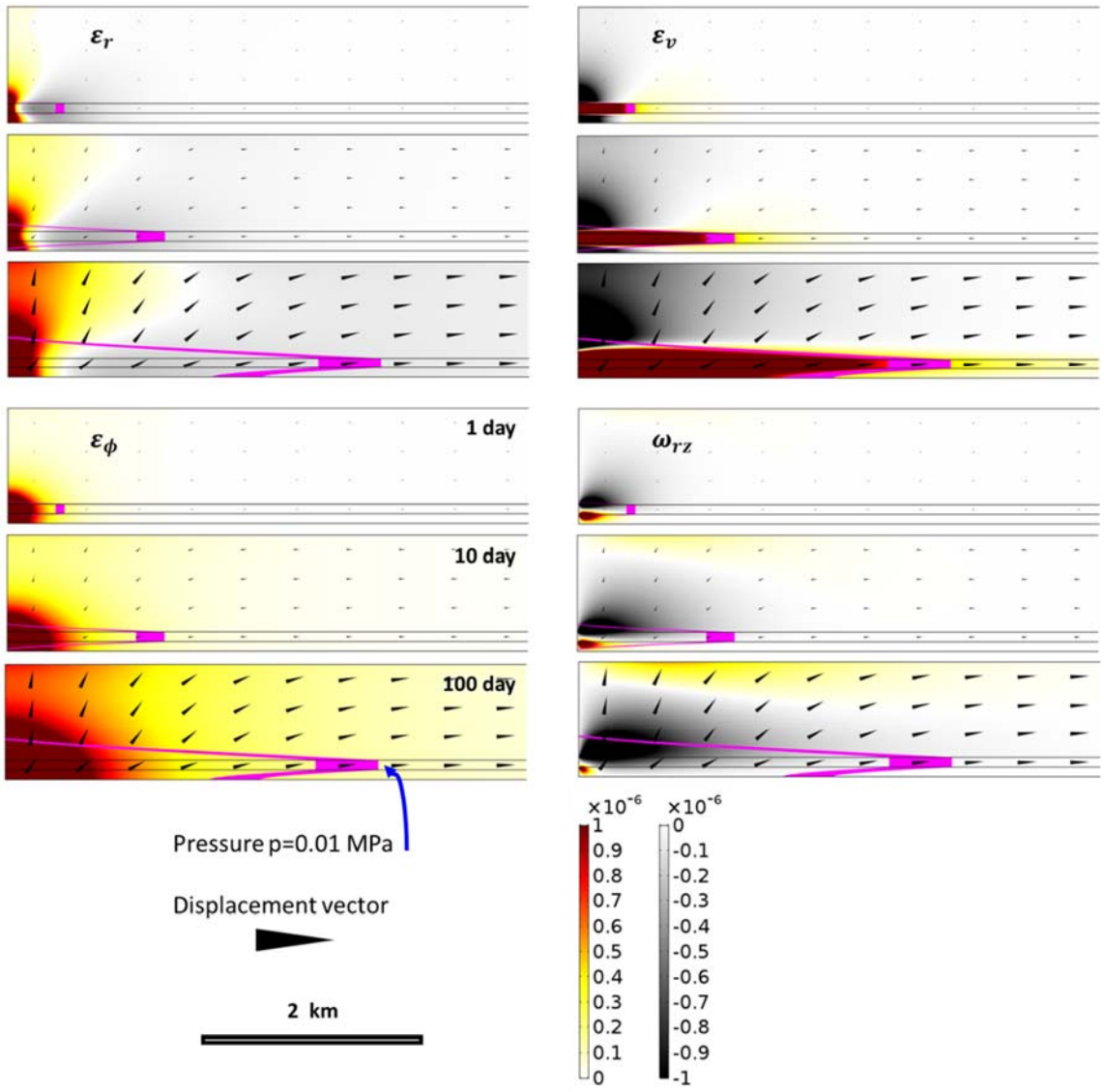

Figure A.4. Strains and tilt at 1, 10, and 100 days after the onset of injection at $p = 1$ MPa. Colored surface plots are positive strains (0 to 1 $\mu\varepsilon$ and grayscale regions are zones of negative strain (-1 to 0 $\mu\varepsilon$). Black vectors are the normalized displacement field. The magenta band is the zone of pressure 0.01 MPa (1% of injection pressure).

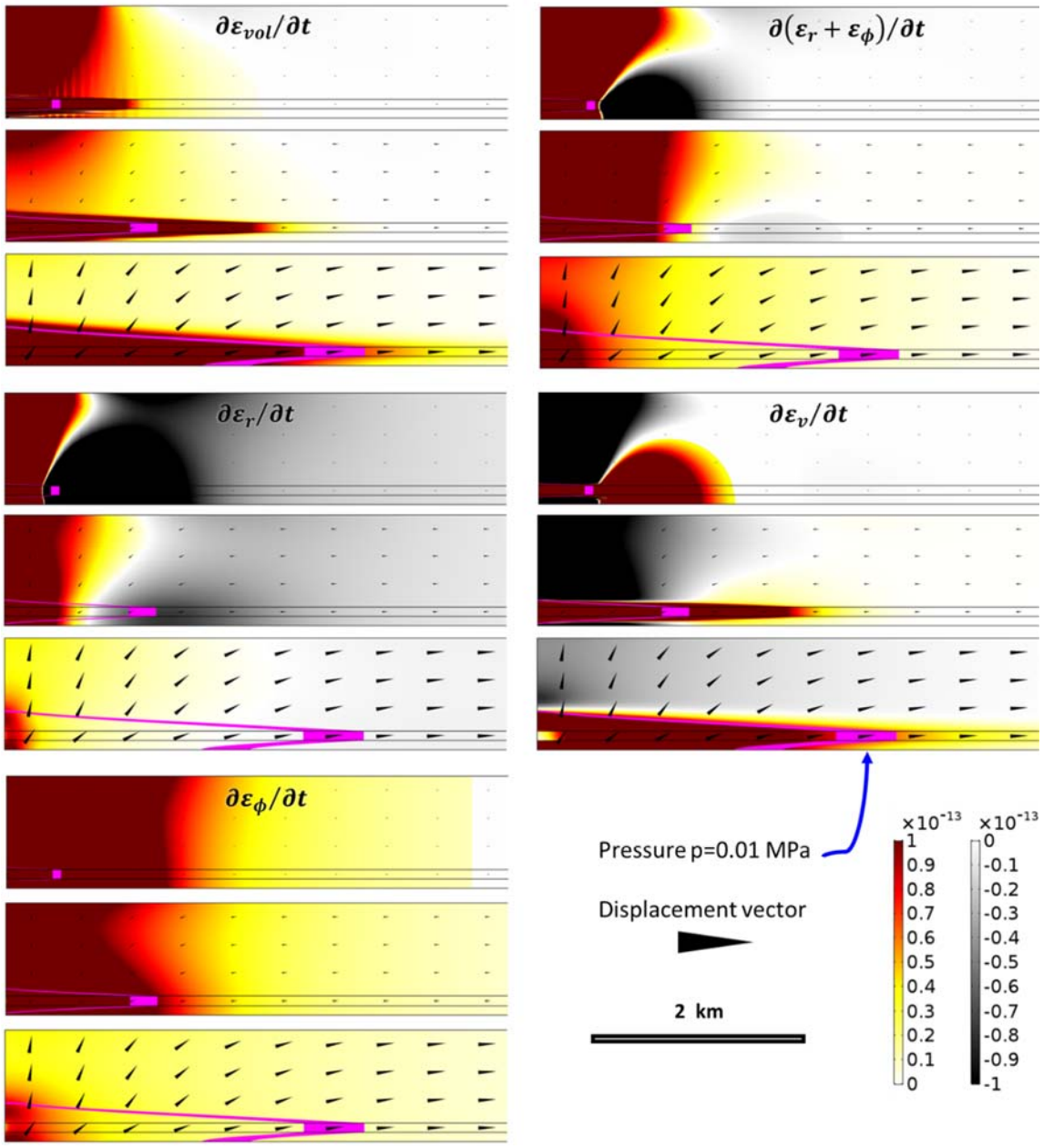

Figure A.5. Strain rates at 1, 10, and 100 days after the onset of injection at $p = 1$ MPa. Colored surface plots are positive strain rates ($0 \leq \varepsilon \leq 1 \cdot 10^{-14}\ s^{-1}$) and grayscale regions are zones of negative strain rate ($-1 \cdot 10^{-14}\ s^{-1} \leq \varepsilon \leq 0$). Black vectors are the normalized displacement field. The magenta band is the zone of pressure 0.01 MPa (1% of injection pressure).

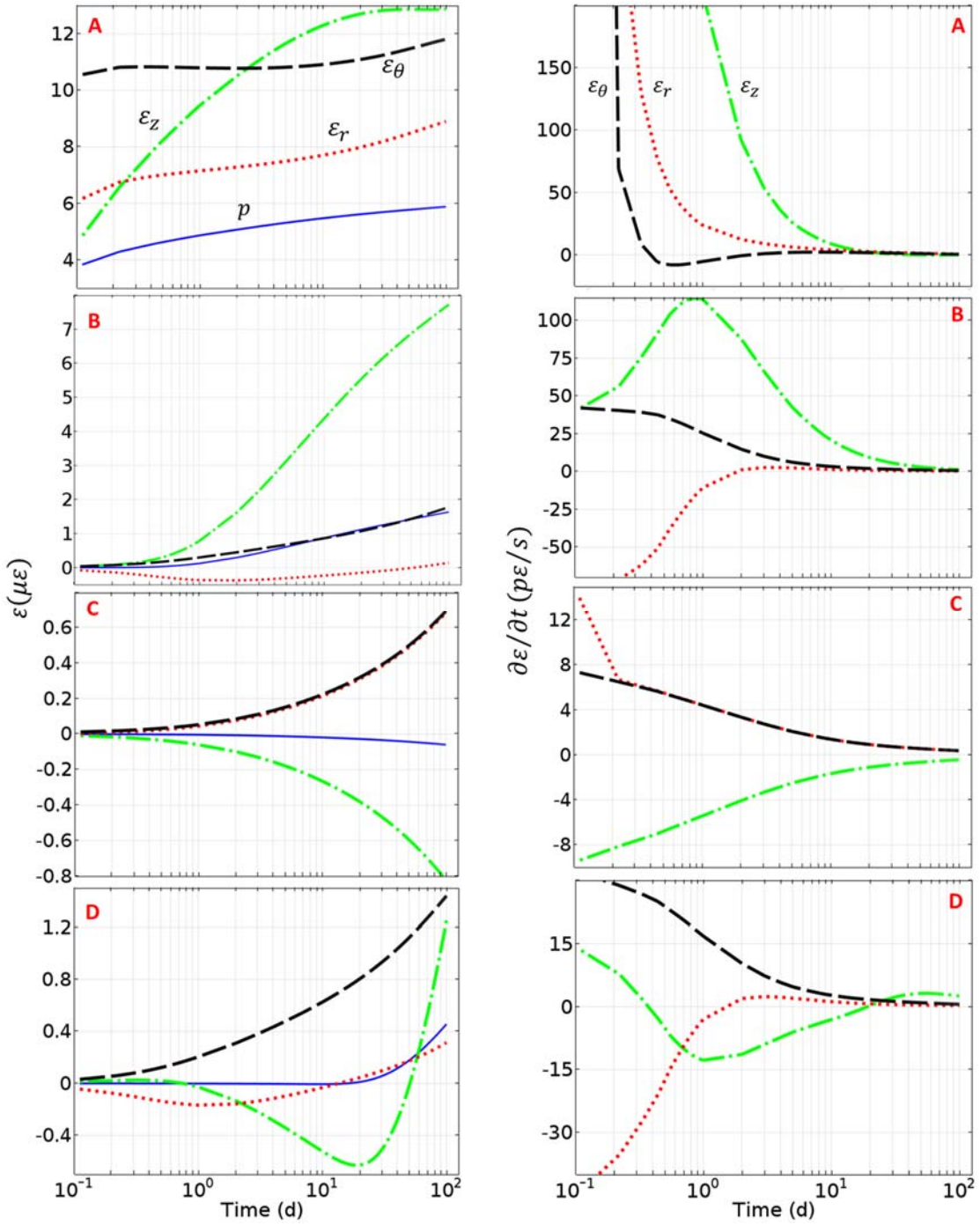

Figure A.6. Pressure (MPa), strain ($\mu\varepsilon$) and strain rates (ps^{-1}) at selected points: (A) near the well screen: $r = 10$ m, $z = 1050$ m; (B) monitoring point in reservoir: $r = 10$ m, $z = 500$ m; (C): near the well casing $r = 10$ m, $z = 100$ m; and (D) monitoring point in confining unit; $r = 500$ m; $z = 900$ m. See Figure A.3 for more information on the position.

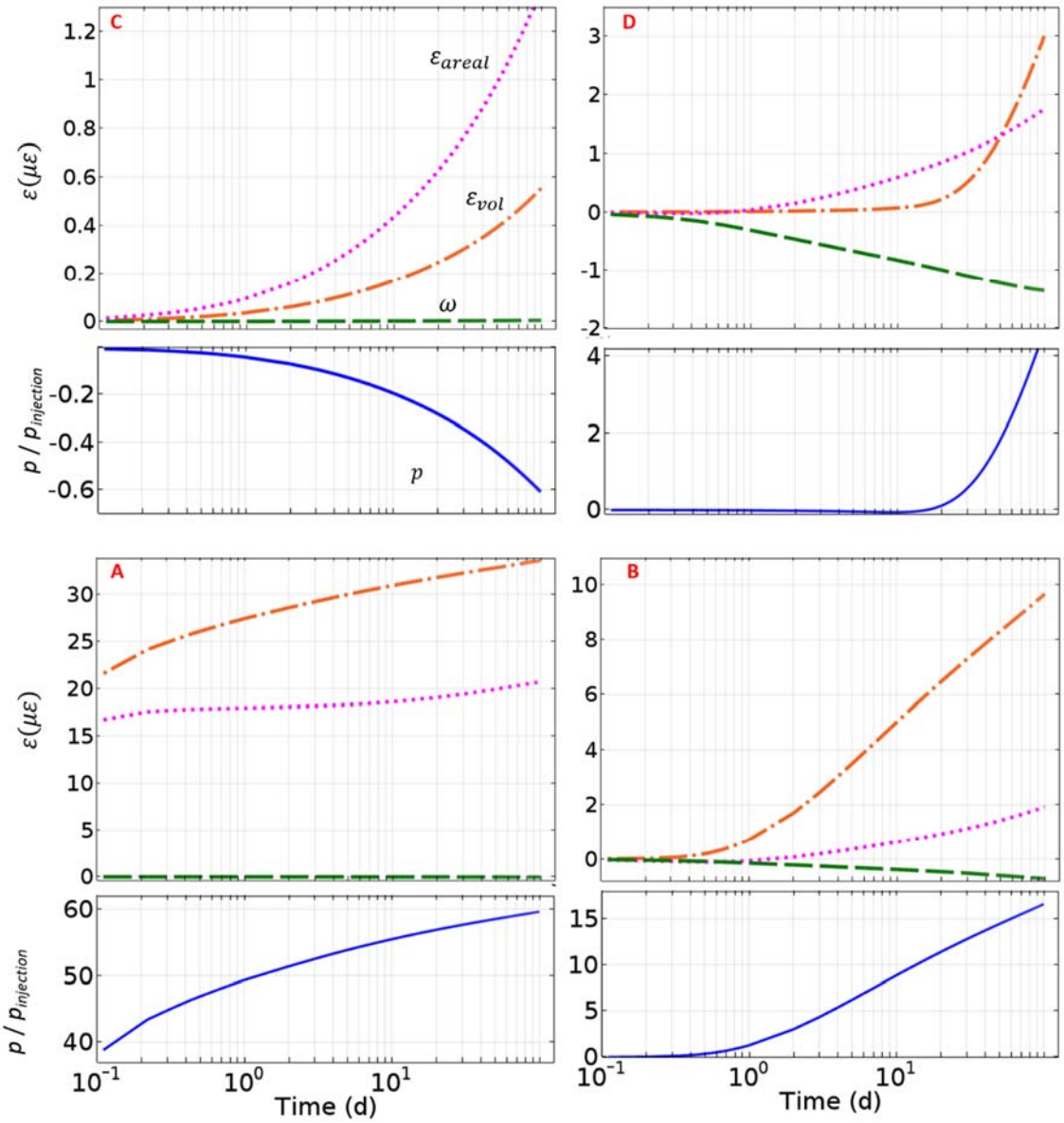

Figure A.7. Volumetric strain (orange dash-dotted line), areal strain ($(\varepsilon_r + \varepsilon_\phi)$, dotted magenta line), and tilt ($(\omega = \partial u_r/\partial z)$, green dashed line) at selected points (A) near the well screen: $r = 10$ m, $z = 1050$ m; (B) monitoring point in reservoir: $r = 10$ m, $z = 500$ m; (C) near the well casing $r = 10$ m, $z = 100$ m; and (D) monitoring point in confining unit; $r = 500$ m; $z = 900$ m. See Figure A.6 for more information on the positions.

A.3. Stratigraphy of sedimentary units at the North Avant field

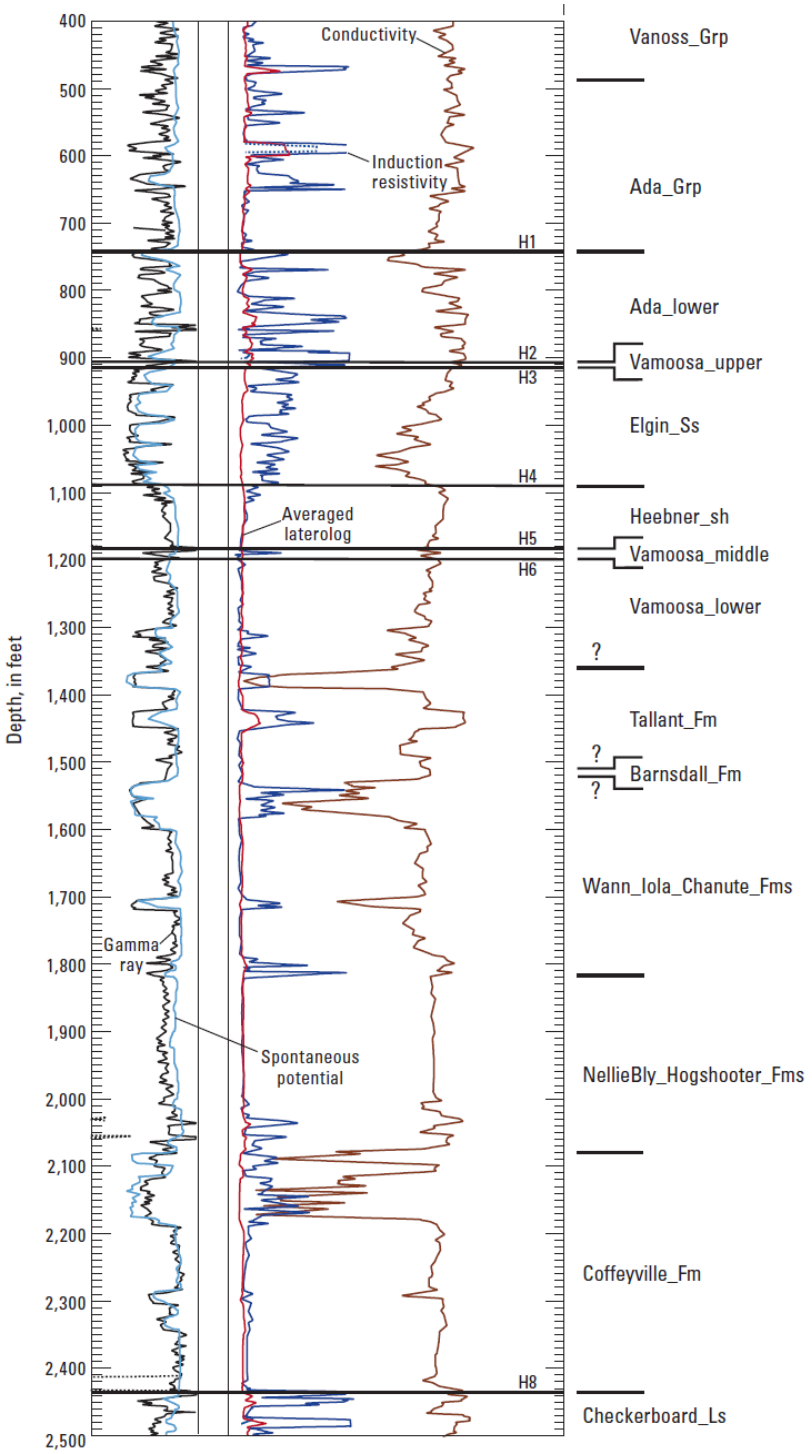

Figure A.8. Wire-line log from northwest Osage County, OK (Figure 4 in *Hudson et al.* [2016]). Sediments are slightly younger (Missourian series) than those at the North Avant field.

A.4. Isopach maps of Bartlesville reservoir

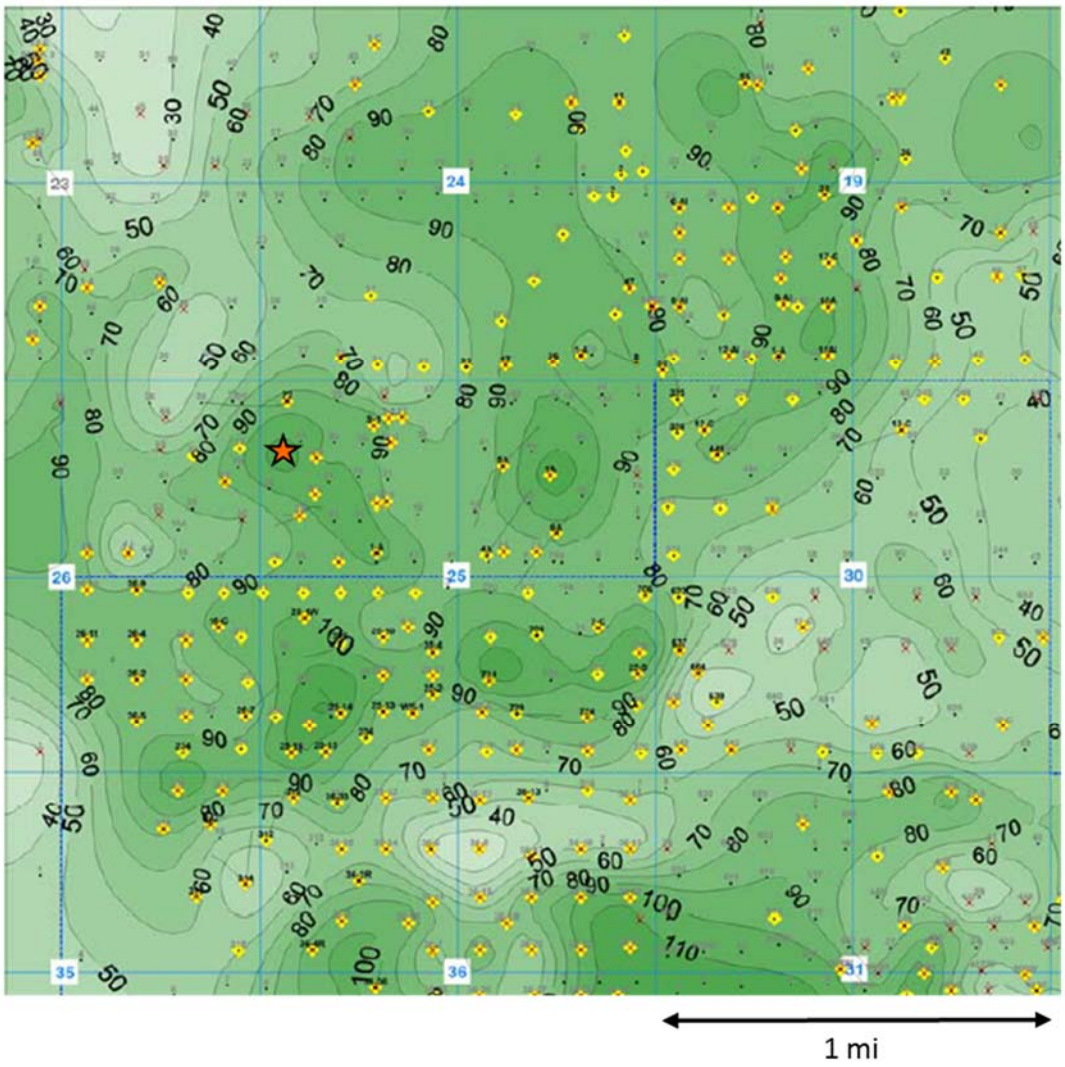

Figure A.9. Isopach map of the C zone (including the high energy channel). Contours are in feet, orange star is the location of well 9A, and yellow diamonds are existing wells. Provided by *Schmeling* [2016].

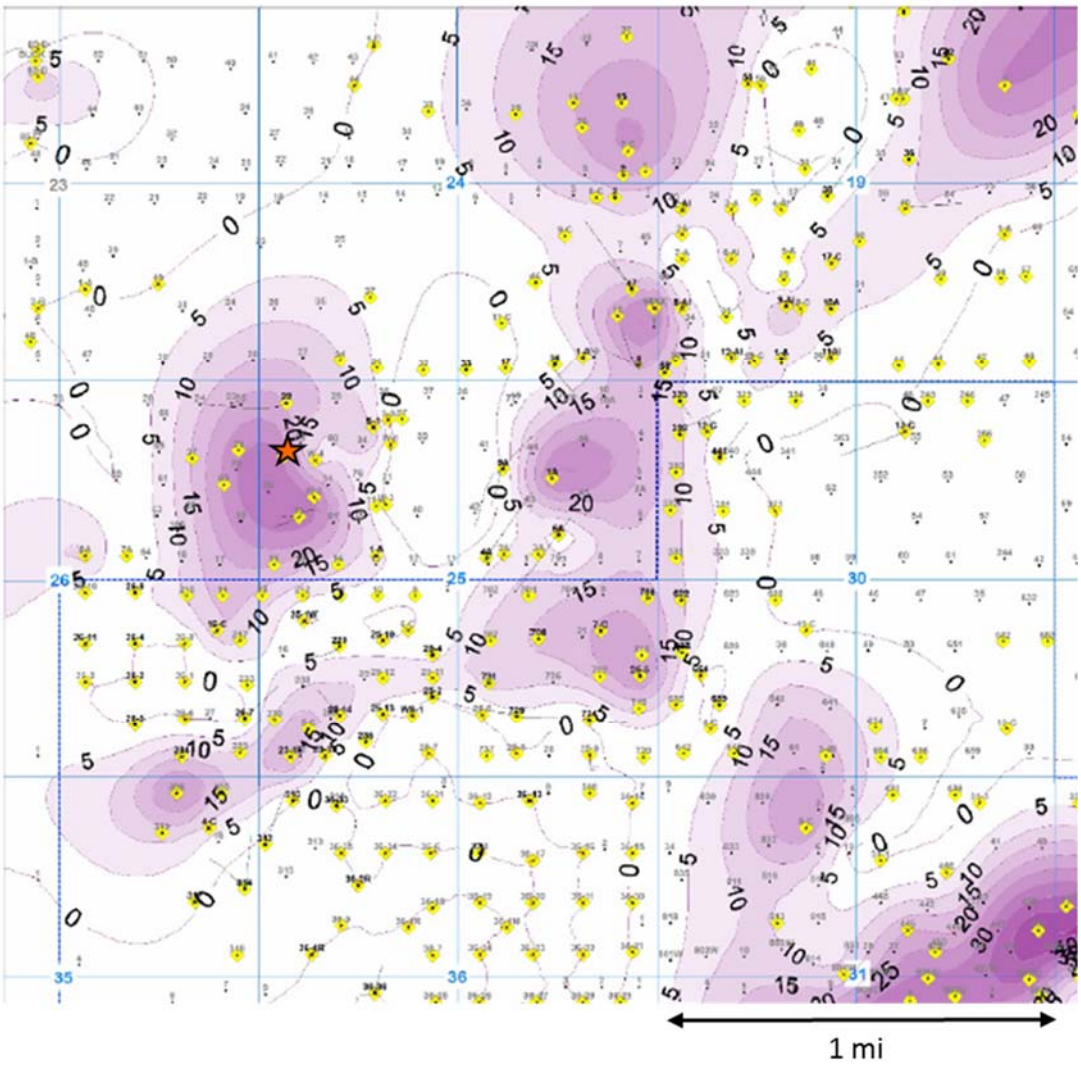

Figure A.10. Isopach map of high energy channels. Contours are in feet, orange star denotes well 9A, and yellow diamonds are existing wells. Provided by *Schmeling* [2016].

A.5. Effect of well casing and screen

In appendix A.2, the screen and casing is included in the model geometry. This representation of the wellbore is physically accurate; however, it is more computation expensive and challenging to incorporate into the geometry of 3-D models. Therefore, the well casing and screen is removed from the model geometry to facilitate calculations in sections 2.5 and 2.6. Here, we test the effect of this assumption on the pressure and deformation pattern (Figure A.11). All other boundary conditions and meshing is identical to the model in appendix A.2, yet the radius of the well remains constant and pressure diffuses directly into the reservoir (no screen). The stress change on the casing is equivalent to wellbore pressure, but the casing is assumed to be sufficiently rigid such that displacement along the wellbore casing is zero perpendicular to the boundary. Injection at a constant pressure $p = 1$ MPa is simulated for 100 days and compared to the subsurface deformation is appendix A.2.

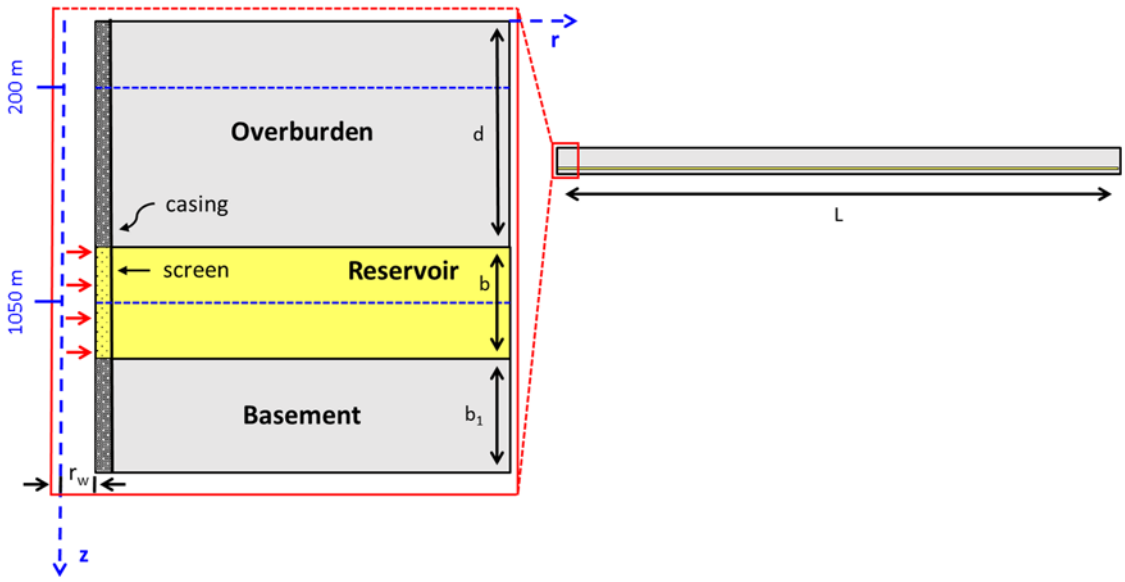

Figure A.11. Axisymmetric model to investigate the effect of the well casing and screen on the deformation pattern. All other conditions are identical model to Appendix A.2, although the figure is no longer to scale. Well casing and screen are included in one scenario. The well is then simplified to a linesource and rigid casing with no displacement. Blue lines denote the radial profiles plotted in Figure A.12.

Two radial profiles of pressure and normal strains are presented in Figure A.12. If displacement is not allowed perpendicular to the well, the profiles of pressure and horizontal strains are somewhat erratic near the wellbore ($r < 10$ m), as the software handles the large pressure gradient at the injection site. The solutions converge for radial distances greater than

approximately 30 m, which is much less than the radial distance proposed for monitoring well locations. Vertical strains match at all locations and times. Additionally, the solutions match more closely in the overburden such that at a depth of 200 m. Over the first several days, solutions also approach one another, yet a limit is then reached and the difference in solutions is nearly constant as time increases. This difference is limited to small radii. Further, the solutions generally converge at smaller radii after one day.

As this analysis shows, the difference in the strain pattern is limited to locations adjacent to the wellbore. We concluded that the well can be simplified to a linesource in our injection models.

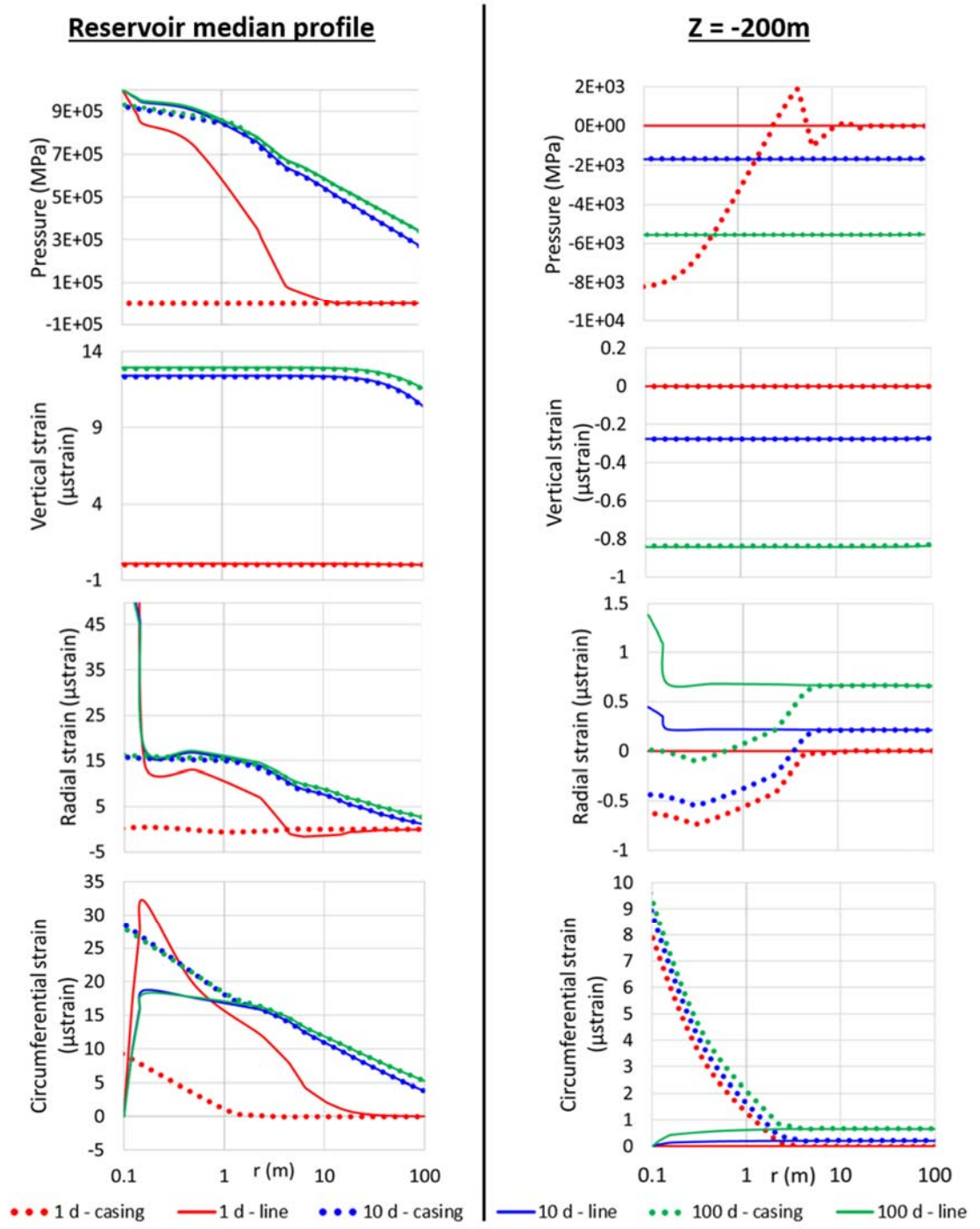

Figure A.12. Profiles of pressure and deformation within the reservoir ($z = -1050$ m) and $z = -200$ m at times $t = 1$ (red), 10 (blue), and 100 (green) days. Solid lines are signals for models that include the casing in the geometry and dotted lines are values from the model simplifying the well to a line source.

A.6. Injection rate and injection pressure

During waterflooding operations, Grand Resources controlled the injection rate and recorded the corresponding wellhead pressure. Injection rate and wellhead pressure were relatively constant ($Q = 500$ barrels per day, $p = 100$ psi) over the last several months prior to shut-in (Figure 2.6). Assuming the water level remains steady at a depth of 450 ft, there will be an additional 200 psi of bottomhole pressure.

During modeling, a constant injection rate or pressure must be assigned. We test the effect of the injection condition on deformation in the axisymmetric model. Model geometry and boundary conditions are the same as section 2.5.2, however the reservoir permeability and porosity were adjusted such that the pressure redistribution within the formation is similar in both cases. The results suggest the average permeability is 12 mD and the model results are described below.

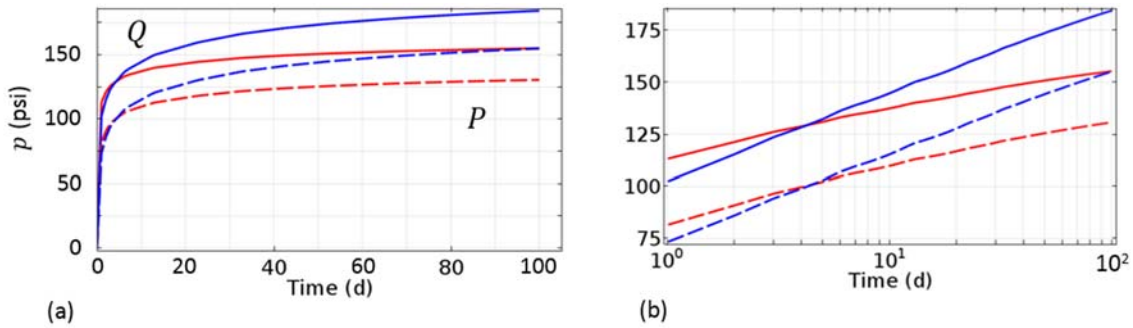

Figure A.13. Median reservoir pressures at 10 m (solid lines) and 20 m away (dotted lines) for injection under a constant pressure boundary condition (red line) and constant rate boundary condition (blue line).

Assigning a constant injection pressure means the bottomhole pressure is always 300 psi. If the average permeability is $k = 12$ mD and injection is at a constant rate, the corresponding bottomhole pressure is approximately 300 psi after 1 day, increases to 320 psi after 10 days, and exceeds 350 psi after 100 days. The formation always undergoes logarithmic pressure growth for both cases.

The evolution of formation pressure is compared at the radial distances of 10 and 20 m. After 1 day, the formation pressure is 10% greater due to a constant pressure boundary condition. After four days, the formation pressure is equal in the two cases, and at 10 days, formation pressure is 5% greater due to constant injection rate. Over tens of days, the injection at a constant rate results

in the formation pressure increasing at approximately double the rate $(\mathrm{psi}/\log t)$, Figure A.13b) than constant injection pressure.

The increase in formation pressure from a constant injection rate results in greater displacements, differences to the pressure and strain are greatest in the formation near the well screen, and changes to the deformation field in the overburden decrease towards the surface. Differences in deformation increase in time, corresponding to the increasing pressure during a constant rate boundary condition. For all times less than 50 days and depths less than 450 m, differences in deformation signals are an order of magnitude below the strength of the signals. The difference in strains within the reservoir exceeded 1 με near the injection line and drop to less than 0.1 με within the overburden. The difference in tilt is also greatest adjacent to the well at great overburden depth. For all depths less than 200 m, tilts vary by less than 0.05 μrad.

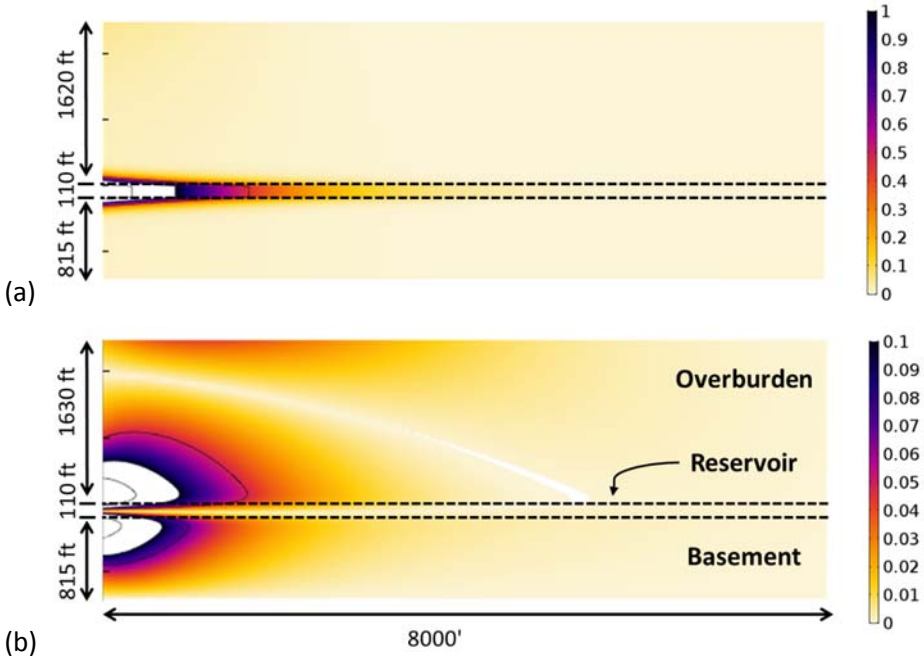

Figure A.14. Difference in the deformation pattern due to injection conditions at a time t = 50 days. (a) Volumetric strain does not vary by over 1 $\mu\varepsilon$ except within the formation and a boundary layer adjacent to the well. (b) The difference in tilt is much less, with ω_{rz} only exceeding 0.1 μrad at locations less than 150 m above and below the reservoir within a lateral distance of 300 m.

A.7. Topography

Our models focused on simplified geometries, where the ground surface is initially a smooth, flat boundary. Well 9A was chosen as the injection site for the field demonstration at North Avant field in part due to the surrounding smooth topography. This is unlikely to be the case in the majority of field settings. This model inspects what effect a topographic feature may have on the deformation pattern. A hill with vertical relief 1:10 is centered directly above the injection well (Figure A.15). The hill has identical properties as the medium and the strain field after 10 days is compared to the homogeneous axisymmetric model in section 2.5.2.

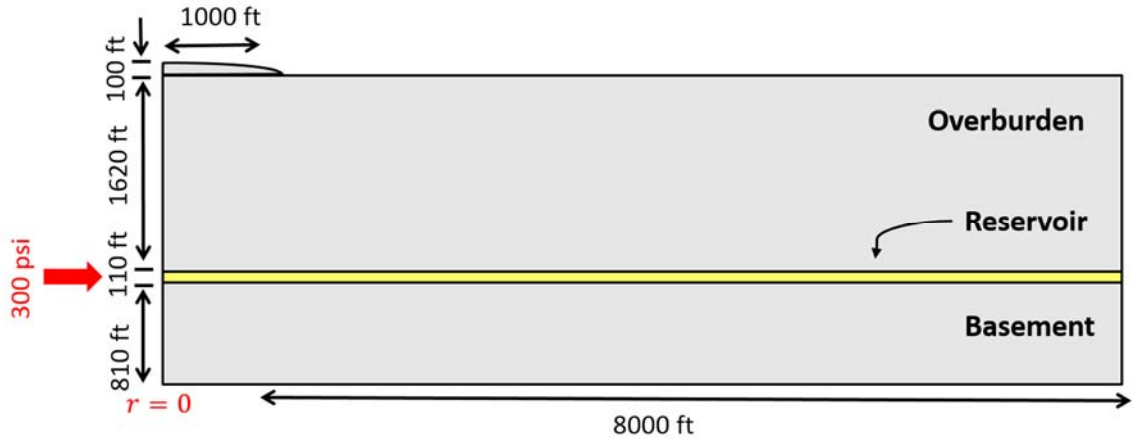

Figure A.15. Geometry of the axisymmetric model with a hill centered above the injection well.

If injection takes place at the summit of a 100 ft high hill with relief 1:10, then alterations to the deformation pattern are greatest near the mound and decrease with increasing distance from the added overburden. Differences in the signals increase in time as the mound reduced the magnitudes of strain and tilt. Strains below the hill vary on the scale of $\mu\varepsilon$, however, differences are limited to near the surface feature. At greater depths $(> 1000 \text{ ft})$, the signal for the case of a hill approaches the homogenous solution (Figure A.16a). Tilt is affected at all depths (Figure A.16b) on a scale equal to the tilt strength. Determining the zone of greatest signal strength also becomes more problematic. The function δ is dampened by the surface feature and no longer has a clear minimum (Figure A.16c).

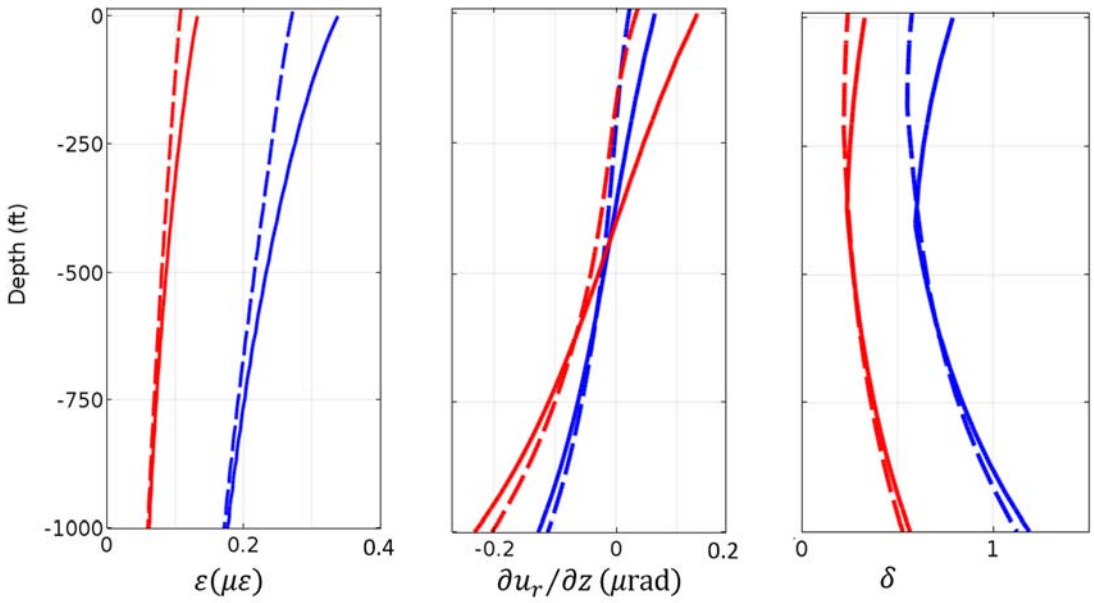

Figure A.16. Vertical profiles of the deformation signals after 10 days (red) and 100 days (blue) at $r = 500$ ft (halfway down the slope).

CHAPTER 3

CONCLUSION AND RECOMENDATIONS

This dissertation addresses two topics of geophysical flow: (1) hydrothermal venting in submarine environments and (2) characterizing the subsurface poroelastic response of CO_2 injection into reservoirs.

The results of studying seafloor hydrothermal venting are as follows:

1. A description of current techniques for measuring hydrothermal flow. In particular, we discuss methods used for direct measurements of diffuse and focused flow reported in this work. Specifically, we discuss the performance of a cup anemometer and two turbine flow meters used to collect measurements on 33 dives to the Juan de Fuca ridge (North Pacific), East Pacific Rise (South Pacific), and Lau Basin (Equatorial Pacific).

2. A database of 104 individual measurements of velocity, temperature, and source area of hydrothermal venting. Measurements are at depths up to 2511 m and at temperatures up to 363°C. In sea trials, the turbine flowmeters provided measurements of hydrothermal flow ranging between 2 and 198.6 cm/s. The cup anemometer device has operated successfully between 7.6 and 88.1 cm/s. Currently, this is the largest collection of direct measurements of seafloor hydrothermal venting.

3. The first direct heat output measurements at the High Rise hydrothermal field, Endeavour segment, and the Dead Dog vent area, Middle Valley, on the Juan de Fuca ridge. This includes the first direct flow rates at most of the structures on the northern part of the Main Endeavour Field (Dante, Hulk, Grotto, and S&M). This dissertation expands on the report by *Ramondenc et al.* [2006] to present the first direct flow and heat measurements at the 9°39.5'N hydrothermal area on the East Pacific Rise, at the Tow Cam and ABE vent fields in the Lau Basin, and at the Puppy Dog mound in the Middle Valley. We obtained the lowest ever measurement velocity, 2 cm/s at the Juan de Fuca ridge.

The characterization of the poroelastic response due to fluid injection into the subsurface is summarized as follows:

1. Created a geologic model of the North Avant field, Osage County, OK. We incorporated existing well logs of the Bartlesville sandstone to separate the reservoir into a homogeneous upper layer with high permeability channels at its base. Channels are not continuous across the field as they consist of deposits in paleovalleys.

2. Described the 2-D and 3-D analytical solutions of the strain induced by pressurizing an inclusion embedded in a homogenous half-space. This is representative of long-term fluid injection into confined reservoirs. These solutions are fast and are consistent with more physically accurate transient numerical models of fluid injection.

3. Characterization of the poroelastic response to fluid injection into a homogeneous anisotropic reservoir. Injection causes the reservoir and overburden to deform in a pattern that varies in time and space. Strains and tilts occur at rates measureable by existing instrumentation.

4. Introduced a new parameter δ to determine zones of greatest signal strength. It is a function of two normal strains and the tilt. The signal strength has a clear minimum at a depth of a couple hundreds of feet.

5. Determine the locations of instrument installation for the field demonstration of waterflooding at the North Avant field, Osage County, OK. Deployment must be at radial locations near to the injection wellhead, where strains are greatest. This distance cannot be too near, however, as there is no tilt adjacent to the wellbore. Instruments should be installed at depths less than 200 ft to avoid the minimum signal of δ.

6. Investigated how the high permeability channels at the base of the reservoir affect the deformation pattern. The strain and tilt signals show distinct signals when channel borders are encountered. In particular, strains increase over the high permeability channel and tilts increase adjacent to the borders of the high energy channel

Our recommendations for future work on characterizing hydrothermal venting include:

1. Additional measurements to increase the database. More than 500 vent fields have been identified [*Beaulieu et al.*, 2013], yet heat output measurements exist for only approximately 10% of these [*Baker*, 2007]. In this work, the velocity of vents varied by a factor or ten or more and the heat outputs can vary by several orders of magnitude on individual structures. To obtain a characteristic average of venting, a distribution of measurements are needed.

2. Improve the design of the flow meters. Our flow meters successfully operated on 33 dives, however, the current instrument design does not incorporate any electronic recording mechanisms, or temperature and chemical sensors. Rather, measurements rely on optical recordings of rotation rates that are analyzed post-dive and converted to velocity using calibration curves. This is considerably labor intensive. Modification to the devices or construction on additional devices can expand the measurement capabilities and accuracy. In some cases, velocities were extrapolated outside the calibration range. In plumes with a large diameter, measurements are limited to the radial outer fringes of the plume to insure optical recording of the cup or turbine rotations. If an electrical or magnetic component were added to the device, measurements can capture discharge occurring at the center of plumes. Instead of optically counting the rotations, a sensor would pick up the signal located on the observation wheel. This would also require an additional data recording and storage component that could be housed along the handle of the device.

3. Little is currently known about the transient nature of hydrothermal discharge. Discharge along structures is highly variable, as fluid pathways are continuously altered by precipitation (clogging). Further, long-term venting relies on a continuous heat source. The current instrument design does not permit long-term deployment. Challenges remain to observe the transient nature of discharge at individual orifices. Time-series of measurements are required to understand the timescale of fluctuations in discharge and understand the evolution of vent fields. Figure 1.10 suggests velocity varies by at least 15% on the scale of seconds, however additional measurements are lacking. Further, it is not clear what effect temporal variations will have on the entrainment of ambient seawater and the microorganisms that rely on the nutrient output from hydrothermal vents. Extended measurement times would allow insight into the rapid fluctuations of discharge, while repeated measurements at the same orifice on the scale of months could quantify the change in permeability structure. Multiple repeated measurements across a vent field would further constrain estimates of the change in vent field heat output.

4. If vertical temperature or velocity measurements are made along a water column, the entrainment coefficient α can be calculated. This needs to be investigated for the high temperature and pressure conditions of hydrothermal venting. Questions that should be addressed include: What is the effect of heat output, i.e., is the entrainment coefficient the same for black and gray smokers? Is the entrainment coefficient constant near the source of hydrothermal vents, or how rapidly does it vary above the orifice?

5. Hydrothermal vents host diverse and thriving biological communities. As venting ceases at one location and initiates at another, these communities must colonize new areas that may be hundreds of kilometers apart. The travel mechanisms is not current known for these organisms, yet likely rely on larval entrainment within plumes to travel great distances. More investigation on the entrainment of plumes in needed to understand how these populations migrate at a sufficient timescale for colonization. Although it is difficult to measure the entrainment directly, incorporating measurements of larvae and microorganism concentrations or vent sources nutrients may more accurately constrain models of entrainment.

Our recommendations for future work on characterization of the poroelastic response due to fluid injection into the subsurface include:

1. The geologic model and simulations of injection are developed from limited field data. In particular, little is known about the elastic parameters of the reservoir and no testing has been performed on the confining units. Sample collection and lab testing, such as triaxial compression, would more accurately constrain the models. Well tests conducted at the North Avant field would provide insight into properties on the reservoir scale. In particular, there is currently no measurements for the Biot-Willis coefficient near the North Avant field. A drained test could be performed, where the confining pressure is increased incrementally while pore pressure is maintained at constant values. The volume change of the sample and fluid volume expelled are then measured, however, for low permeability rocks, laboratory tests on even small samples could take many days.

2. Models were created in preparation of field testing. Instrument siting was determined using these models, however, waterflooding has not initiated yet. The field demonstration can be compared to forward models to see what improvements are needed in the numerical simulations. The injection rate and pressure will vary with time. Unexpected signals are expected to be the result of heterogeneities within the subsurface. These signals should be matched with the deformation in the forward modeling to predict what the subsurface feature may be and constrain the dimensions of the feature. Strainmeter recordings should be input into the model to optimize

parameters. The injection rate and pressure will vary during field testing and can be applied to the forward models to match changes in the deformation pattern.

3. Industrial scale CO_2 sequestration is expected to last on the scale of years. Currently our models do not exceed 100 days. Over time, the strain rates decrease, while the strain continues to increase. Longer time scales should be investigated to insure deformation remains within instrument capabilities. Long-term goals of the project are to apply the injection test at the North Avant field to other sites. In particular, the methods discussed in this work need to be validated during CO_2 sequestration field testing. This can be done by applying the geologic analysis and forwarding modeling to other proposed scenarios such as fully confined reservoirs.

4. Our idealized models highlight the effect of injection on the deformation pattern. Heterogeneities will be encountered during field testing and are expected to be identifiable from the signal. Additional models of unique scenarios (i.e., discontinuities, like faults) should be included in the investigation. These features are expected to alter the permeability structure of the reservoir, which can be further investigated using our numerical modeling to investigate the ability to identify when the injected fluid interacts with these features. This could demonstrate the ability to detect hazards such as leakage.

5. The pressure transient analysis is a primary method of assessing reservoir performance. This test involves measuring flow rates and reservoir pressures under a range of flowing condition and matching the data to reservoir models. If the models match field data, then the parameters are inferred to be the same as corresponding reservoir properties. The solution is not always unique, and it is possible that we may be able to better constrain the analysis by using multiple components of the strain tensor. This should be tested by first modeling different injection (or production) scenarios and observing the reservoir pressure. Then, correlations can be made to the strain signals at shallow depths. The strain may then used as inputs for parameter optimization of unknown reservoir properties.